Fakultät für Geowissenschaften, Ludwig-Maximilians-Universität München

On the Characteristics and Growth of Biominerals

Dissertation der Fakultät für Geowissenschaften der
Ludwig-Maximilians-Universität München zur Erlangung des Grades
DOKTOR RERUM NATURALIS

vorgelegt am
5. Mai 2011
von
Andreas J. Götz

Betreuer:	Prof. Dr. Wolfgang W. Schmahl
1. Gutachter:	Prof. Dr. Wolfgang W. Schmahl
2. Gutachter:	PD Dr. Rossitza Pentcheva
Promotionskommission:	Prof. Dr. Wolfgang. W. Schmahl
	PD Dr. Rossitza Pentcheva
	Prof. Dr. Alexander V. Altenbach
	Prof. Dr. Cristina Pinheiro de Campos (Vorsitzende)
	Prof. Dr. Claudia Trepman
	Prof. Dr. Gordon Winder
Tag der Disputation:	28. Juli 2011

I do not know what I may appear to the world, but to myself I seem to have been only like a boy playing on the sea-shore, and diverting myself in now and then finding a smoother pebble or a prettier shell than ordinary, whilst the great ocean of truth lay all undiscovered before me.

Sir Isaac Newton

Kurzfassung

Die unter dem Einfluss von Organismen entstehenden Minerale können entweder lediglich ein Nebenprodukt des Metabolismus sein oder aber eine Funktion aufweisen, wofür ihre Eigenschaften und Morphologie gezielt vom Organismus gesteuert werden. Der erstere Fall der bioinduzierten Mineralisation wurde in dieser Arbeit bei der Fällung des Minerals Schwertmannit ($Fe_8O_8(OH)_6SO_4$) durch den Bakterienstamm *Leptospirillum ferrooxidans* angetroffen. Die ursprünglich als bio-spezifisch eingeschätzte Morphologie des Minerals konnte in abiotischen Experimenten unter geeigneten Bedingungen erhalten werden. Die in dieser Arbeit am Beispiel der calcitischen Brachiopodenschalen, Seeigelstacheln und Seeigelzähne untersuchten Produkte der gesteuerten Biomineralisation sind Kompositwerkstoffe, deren Eigenschaften aus der Kombination von weichen organischen und harten mineralischen Komponenten entstehen. Sie sind funktionsangepasste Strukturen, für die ein anorganischer Bildungsmechanismus nicht in Frage kommen kann.

Die Bildung der Minerale und deren Eigenschaften wurden mit Hilfe von Rasterelektronenmikroskopie, Rückstreuelektronenbeugung, Transmissionselektronenmikroskopie, Röntgenbeugung, Mikrohärtenmessungen nach Vickers und Nanoindentation untersucht. Durch Messungen mit niedriger Beschleunigungsspannung konnte die laterale Auflösung der Rückstreuelektronenbeugung verbessert werden. Eine Verbesserung der Winkelgenauigkeit der Rückstreuelektronenbeugung wurde durch einen statistischen Ansatz erreicht.

Durch vergleichende biotische und abiotische Syntheseexperimente wurde die Bildung von Schwertmannit durch *Leptospirillum ferroooxidans* als Prozess einer bioinduzierten Mineralisation identifiziert. Die abiotischen Synthesewege beinhalten sowohl zweiwertige als auch dreiwertige Eisenlösungen als Ausgangsmaterial und nutzen verschiedene Wege der Oxidation und/oder Präzipitation von Schwertmannit. Die so gefällten Proben zeigten unterschiedliche Morphologien des Minerals, worunter aber auch die "Igelmorphologie" zu finden war, die in der Literatur als mit Schwertmannit-Nadeln überwachsene Zellen angesehen worden war.

Rietveld-Anpassungen des Röntgenbeugungsprofils des amorphen bis nanokristallinen Minerals zeigen, dass die Kristallitgröße anisotrop ist. Sie ist je nach Bildungsbedingungen 2-2.5 nm senkrecht und als 5-11 nm parallel zu Kanälen, die durch das Netzwerk von $[FeO_6]^{3-}$-Oktaedern in der Struktur gebildet werden.

Die Untersuchungen des Aufbaus calcitischer Brachiopodenschalen zeigen, dass Brachiopodenschalen, je nach Spezies, aus bis zu drei distinkten Mikrostrukturen bestehen können: Kolumnare Schicht, faserige Schicht und Primärschicht. Die Mikrostruktur und Textur der kolumnaren Schicht kann durch einen kompetitiven

Wachstumsprozess erklärt werden, der auch bei anorganischen Prozessen angetroffen werden kann. Eine Erklärung der Mikrostruktur der fasrigen Schicht und der Primärschicht ist hingegen nicht durch Prozesse, die aus anorganischen Systemen bekannt sind, möglich. Die Mikrostruktur der Primärschicht, die in dieser Arbeit erstmalig mit Hilfe von räumlich hochauflösender Rückstreuelektronenbeugung aufgeklärt wurde, ähnelt dendritischen Strukturen. Eine derartig stark verzahnte und hochwiderstandsfähige Mikrostruktur ist bisher bei keinem anderen einphasigen Material bekannt und wird durch einen Entstehungsprozess aus einem amorphen $CaCO_3$ (ACC) Precursor erklärt, der seinerseits eine Agglomeration von ACC-gefüllten Vesikeln entstand. Die Vickerhärten der einzelnen Schichten in Brachiopodenschalen schwanken zwischen 200 und 520 HV (0.005/10) und sind damit deutlich härter als bei anorganisch geformtem Calcit (150-170 HV 0.005/10). Mikrostruktur, Textur und Anordnung der Schichten innerhalb von Brachiopodenschalen maximieren deren Bruchfestigkeit.

Seeigel bilden Calcit mit einem starken Grad an kristallographischer Vorzugsorientierung. Diese Vorzugsorientierung ist bei Seeigelstacheln so hoch, dass diese hochporösen Konstrukte als Einkristalle bezeichnet werden. Eine genaue, räumlich aufgelöste Messung der Orientierung der Kristallite mit Hilfe von Rückstreuelektronenbeugungsmessungen mit hoher Winkelauflösung zeigten, dass es interne Verkippungen bis zu 0.5° gibt. Diese Verkippungen in Seeigelstacheln erlauben Rückschlüsse auf deren Bildung. Die räumlich aufgelöste chemische Analyse in Kombination mit räumlich aufgelöster mechanischer Charakterisierung zeigt, dass der Mg Gehalt (molares Mg/Ca Verhältnnis 1-6 %) in Seeigelstacheln nicht mit Nanohärte (4-4,5 GPa) und E-Modulus (50-80 GPa) korrelierbar ist. Die Nanohohärte von Seeigelstacheln liegt deutlich höher als bei anorganisch gebildetem Calcit (3.0 ±0.2 GPa), während deren E-Moduli ähnlich sind (70 ±5 GPa).

Diese Arbeit untersucht erstmals die Mikrostruktur von Seeigelzähnen mit Rückstreuelektronenbeugung. Die Untersuchungen zeigen, dass die großen strukturellen Einheiten, Steinteil, lamellarer Nadel Komplex, Prismen, Primär-, Sekundär- und Karinarplatten, 3-5° gegeneinander verkippt sind. Diese Bereiche selbst sind wieder in Untereinheiten strukturiert, beispielsweise einzelne Platten, die 1-2° gegeneinander verkippt sind. Diese Untersuchungen zeigen jedoch auch, dass die Bereiche ineinandergreifen können und eine strikte Unterscheidung nicht immer möglich ist. Für dieses Material wird der Begriff des Kompositkristalls vorgeschlagen. Das molare Mg/Ca Verhältnis der untersuchten Seeigelzähne liegt bei 10-25 % und ist positiv mit der Nanohärte (4-8 GPa) korreliert. Die Kombination der Messung der präzisen kristallographischen Orientierung, mikrostrukturellen, chemischen und mechanischen Eigenschaften trägt zu einem tiefergehenden Verständnis des Selbstschärfungsmechanismuses der Seeigelzähne bei. So konnte beispielsweise der häufig diskutierte Einfluss der prominenten 104-Spaltfläche von Calcit ausgeschlossen werden.

Abstract

Minerals formed by organisms may either be simply a side-product of the metabolism or they carry a function, for which their properties and morphologies are controlled by the organism. The first case, bioinduced mineralisation, was encountered in this work in the case of the precipitation of the mineral schwertmannite ($Fe_8O_8(OH)_6SO_4$) by the bacterial strain *Leptospirillum ferrooxidans*. In the literature the characteristic morphology of the mineral had been viewed as bio-specific. However, in this work, in could be produced in abiotic syntheses with appropriate conditions. Products of biocontrolled mineralisation investigated in this work were brachiopod shells, sea urchin spines and sea urchin teeth. These products are hybrid composite materials consisting of soft organic and hard mineral components. For their complex, highly characteristic, and purpose-oriented microstructures an inorganic mechanism can not be envisaged.

The formation of the minerals and their properties has been investigated with scanning electron microscopy, electron backscatter diffraction, transmission electron microscopy, x-ray diffraction, Vickers microhardness indentation and nano-indentation. The use of a low accelerating voltage allowed the increase of the lateral resolution of electron backscatter diffraction. The angular resolution of electron backscatter diffraction could be increased by a statistical approach.

Comparative biotic and abiotic synthesis experiments identified schwertmannite precipitation in cultures of *Leptospirillum ferrooxidans* as a process of bioinduced mineralisation. Different abiotic synthesis started from ferric or ferrous-solutions and used various methods of oxidation and/or precipitation to produce schwertmannite. The samples prepared by these methods led to a variety of morphologies of the mineral, including the "hedgehog" morphology which had been adressed as cell overgrown with schwertmannite needles in the literature.

Rietveld refinements of the diffraction profile of the amorphous-to-nanocrystalline schwertmannite show that the crystallite size is anisotropic. It varies depending on the growth conditions and is between 2-2.5 nm perpendicular and 5-11 nm parallel to channels created by the network of $[FeO_6]^{3-}$-octahedra in the structure.

The analyses of calcitic brachiopod shells show that, depending on the species, a distinction of up to three microstructures are present: columnar layer, fibrous layer and primary layer. The microstructure and texture of the columnar layer of the brachiopod shell can be explained by a process of competitive growth, which can also be found in inorganic systems. However, the formation of the fibrous and the primary layer can not be described by processes known from inorganic systems. The microstructure of the primary layer, which was correctly resolved in this thesis for

the first time by high spatial resolution electron backscatter diffraction, resembles dendritic structures. Such a high interdigitated and highly resistive microstructure is not known from any other single phase material. Its formation is explained in terms of a precursor of amorphous $CaCO_3$ (ACC) which has formed as an agglomeration of ACC-filled vesicles. Vickers hardnesses of the bachiopod shell layers vary between 200-520 HV (0.005/10) and are thus much harder as inorganic formed calcite (150-170 HV 0.005/10). Microstructure, texture and arrangement of the shell layers maximises the fracture toughness of brachiopod shells.

Sea urchins form calcite with a high degree of crystallographic preferred orientation. The preferred orientation in sea urchin spines is so high that these highly porous structures are referred to as single crystals. A precise, spatially resolved measurement of the crystallographic orientation of sea urchin spines gives information on their formation. The spatially resolved chemical analyses of sea urchin spines in combination with spatially resolved mechanical characterisation shows that Mg content (molar Mg/Ca ratio: 1-6 %) is not correlated with the nanohardness(4-4.5 GPa) and Young's modulus (50-80 GPa). The nanohardness of sea urchin spines is higher than that of inorganically formed calcite (3.0 ±0.2 GPa), while the Young's moduli of sea urchin spines and inorganically formed calcite (70 ±5 GPa) are similar.

The present thesis analyses the microstructure of sea urchin teeth for the first time with electron backscatter diffraction. The data shows that the major structural units (i.e. stone, lamellar needle complex, prisms, primary plates, secondary plates and carinar process plates) are misoriented 3-5°. These units are assembled of sub-units, e.g. plates, that are misoriented 1-2°. The data furthermore shows that the units can interdigitate and that a distinction is not always possible. The term "composite crystal" is suggested for these materials. The molar Mg/Ca ratio of the investigated sea urchin teeth is 10-25 % and it is positively correlated with nanohardness(4-8 GPa). The combination of precise measurement of the crystallographic orientation, microstructural, chemical and mechanical analyses lead to a deeper understanding of the self-sharpening mechanism of sea urchin teeth. It could be shown that the 104-clevage of calcite does not influence the self-sharpening.

Contents

List of Abbrevations

Abbrevation	Designation
ACC	amorphous calcium carbonate
ACP	amorphous calcium phosphate
AMD	acid mine drainage
BSE	backscattered electrons
BIF	banded iron formations
CRISP	corrected illumination scanning probe (transmission electron microscope)
CSM	continous stiffness meassurement
EBSD	electron backscatter diffraction
EDX	energy-dispersive X-ray spectroscopy
EPMA	electron microporbe analysis
EPS	extracellular polymeric substances
FIB	focused ion beam
HV	Vicker's hardness (conditions defined in the corresponding section)
LA-ICP-MS	Laser Ablation Inductively Coupled Plasma Mass Spectrometry
MTS	Mechanical Testing System
nh / NH	nanohardness (conditions defined in the corresponding section)
ODF	orientation distribution function
PF	pole figure
PQ	pattern quality
rpm	rounds per minute
SEM	scanning electron microscope
shm / SHM	Schwertmannite
SE	secondray electrons
SURFTRAP	SURFaces for water TReAtment Purposes
TEM	transmission electron microscope
VMHI	vickers microhardness indentation
XAS	x-ray absorption spectroscopy
XRD	x-ray diffraction
XPEEM	x-ray photoemission electron microscopy

Preface

The present dissertation is structured in an introductory part (*Chapter 1*) that familiarizes the reader with the topic of biomineralisation in general and with the investigated biominerals and biomineralisation processes in particular.

Chapter 2 focuses on electron backscatter analyses, the method most intensively used during the preparation of this thesis. It describes in detail the advances achieved on that method as part of this dissertation.

Chapter 3 is a collection of published articles (Sections 3.2, 3.3 & 3.4), submitted manuscripts (Sections 3.1 & 3.6) and manuscripts in preparation (Section 3.5). Every of those sections contains a short introduction on the background of the study and a detailed *methods and samples*-section. Subsequently the results are presented and discussed. Every section of *Chapter 3* contains its own reference list.

Chapter 4 is a more general discussion compared to the discussion present in Chapter 3. It focuses on the fundamental relevance of the observations from Chapter 3 and also compares the observed structures to other well-studied examples from the fields of geology, material science and biomineralisation.

Chapter 5 compares the influence of the investigated organisms on the precipitation of the investigated biominerals.

The *Bibliography* mentions all studies cited within the *Chapters 1, 2 & 4*. Subsequent to the Bibliography an overview on studies that are part of the dissertation, published works, memberships and prizes and my curriculum vitae is given.

1 Biomineralisation

1.1 Processes of Biomineralisation

The term *biomineralisation* refers to the processes by which organisms form minerals (Lowenstam & Weiner 1989). The processes of mineral formation mediated by organisms are different from those occurring in an abiotic system. Organisms strongly influence local phase equilibria and kinetics of reactions and thus actively form environments and geologic settings. Marine sedimentary rocks such as radiolarites or chalk cliffs (consisting of coccoliths) illustrate the high efficiency and the extent of biomineralisation processes.

Processes of biomineralisation occur widely and are conducted by organisms within all biologic kingdoms. This leads to a wide variety of minerals that are formed by organisms (Table 1.1). Two main categories of biomineralisation are commonly distinguished that qualify the significance of the mineralising organism for the product. After the nomenclature proposed by Mann (1983) they are referred to as *biologically induced mineralisation* (*bioinduced mineralisation*) and *biologically controlled mineralisation* (*biocontrolled mineralisation*).

In bioinduced mineralisation the metabolic activity of living matter leads to the formation of minerals. However, the process of mineral formation is not actively controlled by the organism.

In contrast, during biocontrolled mineralisation the process of mineralisation is regulated by the organism. Biocontrolled mineralisation often results in highly optimized bio-composite materials. To produce such bio-composite materials the organism controls a variety of properties of the resulting biomineral[1]. Examples for those properties are the phase/polymorph, the crystallographic orientation, mechanical properties, chemical composition and others.

The aim of this dissertation is the investigation of exemplary biomineralisation products that (a) are formed as a by-product of metabolism and (b) biominerals where the formation was actively controlled by the organism. As exemplary materials for (a) minerals precipitated by iron oxidising bacteria were investigated and as an example for (b) skeleton minerals of brachiopods and sea urchins were investigated.

---

[1]Note that the term *biomineral* refers to a composite of mineralized inorganic products and organic components (Weiner & Dove 2003).

Table 1.1: Examples for minerals produced by organisms. The information is compiled mainly from Lowenstam & Weiner (1989). Entries that are based on other literature sources are labelled accordingly.

Mineral	Composition	Exemplary Organisms / Comments
Carbonates		
Calcite	$CaCO_3$	- Spicula of Porifera, skeletons / spicules of Cnidaria, brachiopod shells, cuticula and eye-lenses of Crustacea, skeletons and teeth of Echinodermata, tests and shells of Foraminifera, resting cysts of Dinoflagelata, coccoliths of Coccolithophoridae.
Aragonite	$CaCO_3$	- Mollusc shells, tests and shells of Foraminifera, coccoliths of Coccolithophoridae.
Vaterite	$CaCO_3$	- Shells of immature gastropods, gastropod eggs and pearls formed by molluscs (Soldati et al. 2008).
Protodolomite	$CaMg(CO_3)_2$	- Teeth of sea urchins.
Amorphous Calcium Carbonate (ACC)	non-stoichiometric phase	- Precursor for calcite in Echinodermata (Politi 2004) and Brachiopoda (Schmahl et al. 2009), cuticle and blood of Crustacea. At least five distinct varieties of ACC are known up to now (Weiner et al. 2005).
Phosphates		
Dahlite	$Ca_5(PO_4,CO_3)_3(OH)$	- Mammal bone and teeth.
Francolite	$Ca_5(PO_4)_3F$	- Mammal teeth (enamel), Tympanic bulla of whales / dolphins (sound reception), brachiopod shells.
Amorphous Calcium Phosphate (ACP)	non-stoichiometric phase	- Mitochondria of Mammalia for ion storage, cow milk for ion storage, precursor phase in molluscs and zebrafish (Mahamid et al. 2008). Several distinct varieties of ACP exist.
Silica		
Opal	$SiO_2 \cdot nH_2O$	- Spicula of Porifera, radula of gastropods, tests and shells of Foraminifera, skeletons of Radiolaria.
Iron Oxides		
Magnetite	Fe_3O_4	- Chiton teeth, magnetosensors in pigeons and magnetotactic bacteria (e.g. Winklhofer & Petersen 2006).
Goethite	$FeOOH$	- Radula of snails, iron-oxidising bacteria (Larese-Casanova et al. 2010).
Lepidocrocite	$FeOOH$	- Chiton teeth, iron-oxidising bacteria (Larese-Casanova et al. 2010).
Schwertmannite	non-stoichiometric phase	- Iron-oxidising bacteria (Section 3.1).
Oxalates		
Whewellite	$CaC_2O_4 \cdot H_2O$	- Product of excretion from mammalia (e.g. kidney stones).
Weddellite	$CaC_2O_4 \cdot (2+X)H_2O$ with ($X \leq 0.5$)	- Product of excretion from mammalia (e.g. kidney stones), Skeleton of Chlorophyta.

1.2 Metabolic By-Products - Schwertmannite

1.2.1 Microbial Iron Oxidation

An excellent example for microbial mineralisation is the precipitation of iron-oxide minerals[2]. Iron is the fourth most abundant element in the earth crust. It is occurs naturally in three stable oxidation states, Fe^{3+} (ferric iron, Fe-(III)) and Fe^{2+} (ferrous iron, Fe-(II)) and seldom as Fe^0 (metallic iron). Both, the reduction and oxidation of iron are common reactions to gain energy for microorganisms: Some microbia gain energy from oxidation of Fe-(II) to Fe-(III) whereas others reduce Fe-(III) to Fe-(II) (Weber et al. 2006). As the solubility of Fe-(III) is lower compared to that of Fe-(II) (cf. Figure 1.1), the oxidation of Fe-(II) to Fe-(III) leads to a precipitation of iron oxide minerals. The difference in redox-potentials between the Fe-(II)/Fe-(III) and the O_2/H_2O redox couples is low, thus a large amount of Fe-(II) is necessary to produce relatively little cell mass (e.g. Rawlings 2007). This results in the precipitation of large amounts of iron oxides by relatively few organisms. It is argued that the *banded iron formations* (BIF)[3] result, completely or at least in part, from biogenic iron oxidation (Koehler et al. 2010). In systems with non-acid pH values the reaction speed for the transformation of Fe-(II) to Fe-(III) is too fast to allow microorganisms to catalyse the reaction and thus the bacterial iron oxidation of Fe-(II) to Fe-(III) is limited to acid regimes (e.g. Holmes & Bonnefoy 2007, Rawlings 2007).

The oxidation of Fe-(II) in mining environments often results in a dissolution of pyrite (FeS_2). In this process the liberation and oxidation of sulphur to sulphate leads to an acidification of mining areas known as *acid mine drainage* (AMD) but also to a release of toxic metals present in the sulphides. The great efficiency of microbial pyrite dissolution gives this process a major relevance for environmental problems. However, the efficiency of this process also renders it interesting for *biomining* activities. In biomining microbial dissolution of pyrite and other metal sulphides is exploited to dissolve valuable metals like copper (Domic 2007), cobalt (Morin & d'Hugues 2007), gold (Logan et al. 2007) and others.

It is furthermore worth to mention that the dissolution of pyrite was proposed to be the key reaction for the formation of life (e.g. Wächtershäuser 1988, Wächtershäuser 1990, Wächtershäuser 2000, Cody 2004, Hazen & Sverjensky 2010) in a model known as the *iron-sulphur-world*.

The dominating organisms in these iron rich AMD regimes are *Acidithiobacillus ferrooxidans* and *Leptospirillum ferrooxidans* (cf. Rawlings 2007, Norris 2007). However a wide variety of additional microorganisms is usually present in those environments. Rawlings (2007) compiled common characteristics of all microbia with a metabolism that is based on the oxidation of Fe-(II) to Fe-(III): (1) They are autotrophically growing organisms that fix CO_2 from the atmosphere, (2) they obtain their energy by using Fe-(III) as an electron donor, some species can use additionally

---

[2]The term *iron-oxide* is usually referred to a wide variety of iron-oxy-hydroxy minerals and also includes minerals like akaganeite and schwertmannite that contain Cl or S, respectively (Cornell & Schwertmann 2003).

[3]BIF are the largest source of iron ores on our planet (Koehler et al. 2010).
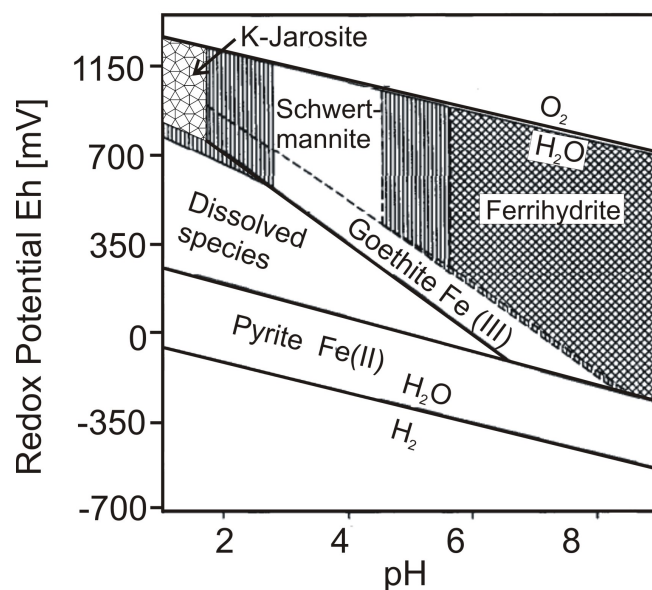
Figure 1.1: Pourbaix-diagram for the system Fe-S-K-O-H. Fields of metastability are shown by dashed lines. Single hatched areas indicate that the stability of jarosite and ferrihydrite expand for lower sulphate concentrations. Graph modified after Bigham et al. (1996).

reduced inorganic sulphur compounds. The electron acceptor is generally assumed to be oxygen. (3) They are acidophiles and grow in low-pH environments. (4) They are remarkably tolerant to a wide range of metal ions.

1.2.2 Production and Application of Schwertmannite

This work deals with the precipitation of the mineral *schwertmannite* by iron oxidising bacteria. Schwertmannite is a quasi-amorphous and non-stoichiometric iron-oxy-hydroxy sulphate with an idealized composition of $Fe_8O_8(OH)_6SO_4$ (e. g. Bigham et al. 1990, Bigham et al. 2994). It is widely abundant in areas of AMD (e. g. Ferris et al. 2004). However, it is also the product of a pilot bio-reactor plant located at the open pit lignite mine "Schwarze Pumpe", Upper Lusatia (Germany). In this mine ground water needs to be removed from the ore body prior to the extraction of the coal by a drainage system (Peiffer et al. 2010). The drainage water contains high amounts of iron and sulphur from the dissolution of sulphide minerals present in the coal, e. g. pyrite (Acharya et al. 2003). The dissolution of sulphide minerals results from bacterial activity that leads to an oxidation of sulphide to sulphate, a process that includes the reduction of Fe-(III) to Fe-(II) (Acharya et al. 2003, Rohweder et al. 2003). From the acidic drainage water (pH ranging from 3 - 5) schwertmannite is precipitated in the pilot bio-reactor. The precipitation of schwertmannite cleans the drainage water from sulphur and iron.

It is known that the precipitation of schwertmannite in the bio-reactor results from the oxidation of the solved Fe-(II) to Fe-(III). The lower solubility of Fe-(III) compared to that of Fe-(II) leads to a precipitation of schwertmannite (cf. Figure

1.1). It is also known that the oxidation of Fe-(II) is performed by microorganisms present in the bio-reactor. In order to enhance the precipitation process it is necessary to better understand the direct influence of the microorganisms present in the reactor. Ferris et al. (2004) mention that schwertmannite precipitating bacteria can influence the mineralisation process in various ways. They observed mineralisation in vesicles, mineralisation within *extracellular polymeric substances* (EPS) but also mineralisation on the external face of the cell wall and precipitation inside the surface of the cell membranes. The last two processes mean that the precipitation of schwertmannite can kill the bacterial cell. An overgrowth of bacteria with schwertmannite might lead to a mass mortality of microorganisms in the reactor. This undesirable event would slow down the industrial process of schwertmannite precipitation as less Fe-oxidation would occur. The influence of bacteria on the precipitation of schwertmannite is discussed in Section 3.1.

The excellent sorption capacities of schwertmannite regarding toxic metals (Waychunas et al. 1995, Webster et al. 1998, Carlson et al. 2002, Regenspurg & Peiffer 2005, Burton et al. 2010) allow its further use as a filter material. First trials in an industrial scale to use schwertmannite to remove toxic metals from water are run at a second pilot plant. It is located in a water treatment facility of the Wismuth AG in Schlema / Alberoda (Peiffer et al. 2010). These tests aimed to remove As and confirmed the excellent sorption properties of schwertmannite not only for As but also for U (Peiffer et al. 2010).

It is essential to understand the crystallographic structure of schwertmannite in order to obtain a deeper understanding of its sorption capacities and the stability of adsorbed toxic metal anions. However, the quasi-amorphous structure of schwertmannite impedes structural analyses. Until recently, it was commonly assumed that the structure of schwertmannite consists of a β-FeOOH-cage (Figure 1.2a) that is filled with sulphate groups (Bigham et al. 1990, Bigham et al 1994). Recent work proposed a similar structure model in which those channels are broken (Fernandez-Martinez et al. 2010, Figure 1.2b). This model was tested in Rietveld refinements in the present thesis and turned out to fit the observed data significantly better than the β-FeOOH-model (Section 3.1). The Rietveld refinements furthermore allowed to extract an assumption on the anisotropic crystallite size of schwertmannite.

1.2.3 *Leptospirillum ferrooxidans*

The organisms chosen to investigate the process of iron-oxide precipitation in the bio-reactor belong to the gram-negative, obligate aerobic bacterial strain *Leptospirillum ferrooxidans* EHS-2 (Hedrich et al. 2009). The investigated strain was isolated at the bio-reactor at the lignite mine where it is especially abundant at the inflow area (Heinzel et al. 2009). In pure culture this bacterial strain produces either schwertmannite, jarosite or a mixture of goethite and lepidocrocite depending on the pH of the medium (cf. Figure 1.1). *Leptospirillum ferrooxidans* is an organism widely occurring in AMD environments (e. g. Bond et al. 2000, Hallberg et al. 2006).
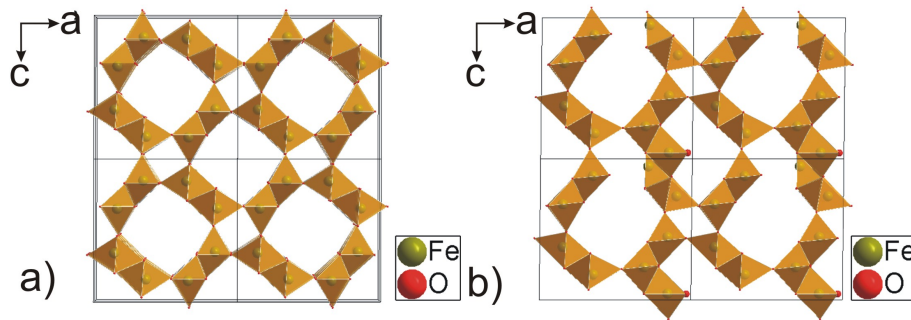
Figure 1.2: a) $\beta-FeOOH$-cage derived from a model obtained by Stahl et al. (2003) for akaganeite, Cl and H are not shown. It was commonly assumed that schwertmannite has a similar structure (e.g. Bigham et al. 1994). b) Schwertmannite structure proposed by Fernandez-Martinez et al. (2010). In difference to the $\beta-FeOOH$-cage the channels are broken and form a more open network.

It is noteworthy that, in opposition to their name, the organisms of the investigated strain are not spirilla but rod-shaped.

Leptospirillum ferrooxidans was chosen for this work as its preferred redox-potential activity range (600-1000 mV, Tributsch & Rojas-Chapana 2007) matches better the stability range of schwertmannite (Figure 1.1) than the redox-potential activity range of *Acidithiobacillus ferrooxidans* (0-700 mV, Tributsch & Rojas-Chapana 2007).

Leptospirillum ferrooxidans is known to use exclusively Fe-(II) as an electron donor and it was not reported that it uses electron acceptors other than O (Rawlings 2007). It possesses the genes necessary for nitrogen fixation (Norris et al. 1995, Parro & Moreno-Paz 2003) and for the fixation of carbon by means of the Calvin cycle (Tyson et al. 2004).

Little is known of the process of iron oxidation performed by the cell. It was recently proposed by Tyson et al. (2004) that the iron oxidation in *Leptospirillum ferriphilum*, a close relative of the here investigated *Leptospirillum ferrooxidans*, is located in the periplasmic space between the inner cytoplasmic membrane and external outer membrane. The electrons are then transferred to the cytoplasm where the reduction of oxygen is believed to take place.

Leptospirillum ferrooxidans is commonly found in pyrite oxidising communities (e.g. Schrenk et al. 1998, Rojas-Chapana & Tributsch 2004, Rawlings 2007). It is reported that in these environments the cells of *Leptospirillum ferrooxidans* are surrounded by a capsule of EPS containing nanoparticles of pyrite that were removed from the substrate in a process of "electrochemical machining" (Rojas-Chapana & Tributsch 2004). The EPS capsules containing nanoparticles can be interpreted as an energy storage for individual microorganisms (Rojas-Chapana & Tributsch 2004, Tributsch & Rojas-Chapana 2007).

1.3 Skeleton Minerals - Calcite

1.3.1 Mineralisation of Calcite Skeletons

Among the biominerals produced by higher organisms some of the most abundant structures are probably endo- and exoskeletons. These skeletons are in many cases produced from $CaCO_3$ (cf. Table 1.1). In biominerals crystalline $CaCO_3$ appears mainly in the phases of calcite and aragonite but vaterite can also be present. In addition to crystalline phases also amorphous calcium-carbonate (ACC) is present in carbonatic biominerals. In the recent time more and more evidence appears that crystalline calcium-carbonate phases in biominerals are often formed from ACC as a precursor (Section 3.3, Beniash et al. 1997, Addadi et al. 2003, Politi et al. 2004, Politi et al. 2008, Griesshaber et al. 2009, Schmahl et al. 2010).

In classical crystallisation from hydrous solution hydrated ions are present in solution and are subsequently attaching to a crystal leading to its growth. In bio-controlled mineralisation of $CaCO_3$ there exist structures that are believed to precipitate in such a manner from aqueous solution, e.g. corals (Cohen & Gaetani 2010), Foraminifera (Bentov et al. 2009) and the shell of avian eggs (Hérnandez-Hérnandez et al. 2008). However, it is discussed that a variety of biominerals are formed by *non-classical crystallisation* processes (e.g. Coelfen & Antonietti 2005, Coelfen & Antonietti 2008). The concept of this non-classical crystallisation is based on the assembly of nanoparticulate intermediates such as ACC to bigger crystal aggregates. The product of this process is referred to as a *mesocrystal*[4]. The concepts of non-classical crystallisation are of special interest for biomineralisation studies as they are independent of solubility products and allow high crystallisation rates. Furthermore, they do not include changes in pH or osmotic pressure that are problematic to explain in organisms (Coelfen & Antonietti 2005). Up to now several mechanisms of non-classical crystallisation have been identified (Figure 1.3, Coelfen & Antonietti 2008) that include the aggregation of nanoparticles to macroscopic crystals (Xu et al. 2006, Zhou et al. 2009), clusters in liquid precursors (Gower & Odom 2000, Jee et al. 2010) as well as the transformation of an amorphous precursor phase (Addadi et al. 2003, Weiner et al. 2005).

As mentioned before the amorphous precursor in calcitic biominerals is ACC, a metastable phase under environmental conditions. It can be stabilized e.g. with Mg^{2+}- and PO_4^{3-}- ions or organic compounds such as oligosaccharides and amino acids (Merten & Bachman 1980). At east two forms of ACC exist (i): an essentially anhydrous *transient ACC* that rapidly transforms within minutes to crystalline calcium carbonate phases and (ii) indefinitely stabilized *stable ACC* ($CaCO_3 \cdot H_2O$) (Addadi et al. 2003). From the stable ACC phases different modifications can be distinguished by EXAFS that differ in their short-range order (Addadi et al. 2003).

---

[4]Mesocrystal is the abbreviation of *mesoscopically structured crystal* refers to colloidal crystals that are built up from individual nanocrystals and are aligned in a common crystallographic register and scatters x-rays like a single crystal (Coelfen & Antonietti 2008).
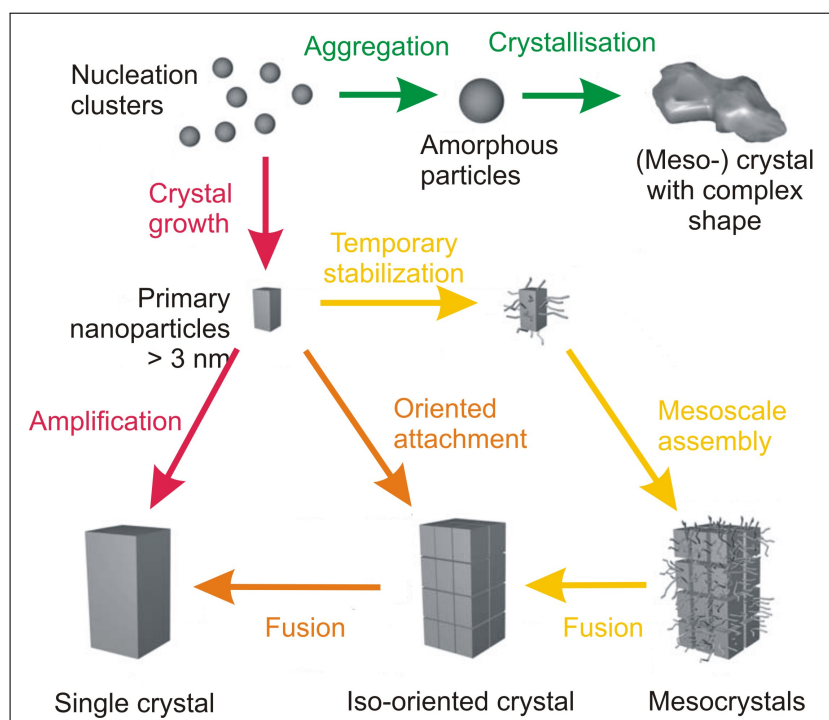
Figure 1.3: Pathways of crystal growth. The classical way is marked by red arrows: nucleation clusters grow to primary nanoparticles that grow further to single crystals. The orange path shows a process called oriented attachment in which primary nanoparticles aggregate to an iso-oriented crystal that can then fuse to a classical single crystal. The yellow pathway stabilizes the nanoparticles with organic molecules and the molecules fuse by mesoscale assembly to a mesocrystal that can fuse to an iso-oriented crystal and a classical single crystal. The green path shows that nucleation clusters can aggregate to amorphous particles that then crystallize in a solid state reaction to a crystal or mesocrystal. Figure modified after Coelfen & Antonietti 2008.

In the present work calcitic skeletons from sea urchins and brachiopods were investigated as examples for biocontrolled mineralisation. Beside the fundamental interest to understand the mechanisms by which an organism creates the, often very beautiful, microstructures of calcitic skeletons one main focus of this work is to reveal mechanical optimizations of those microstructures. Furthermore the results of this work contribute to studies from the field of paleoclimatology.

1.3.2 Background Information on the Investigated Organisms

Brachiopoda - Lamp Shells

The phylum Brachiopoda (also referred to as *lamp shells* or *brachiopods*) consists of marine, solitary sessile organisms. They form a dorsal and a ventral valve that surrounds the soft tissue of the animal (Figure 1.4). In contrast to bivalve mollusc shells that have two equal shell halves the dorsal and ventral valve are unequal in brachiopod shells (Williams et al. 1997). There is no taxonomic relation between molluscs and brachiopods.

The brachiopod valves are connected to the substrate with a fleshy stalk referred to as *pedicle*. The sessile brachiopods feed by filtering micro-organisms from the ocean water with an apparatus of tentacles, the *lophophor*. Brachiopods are animals living with a low energy life style that allows them to survive a long time without food allowing them to compete against other animals in habitats with limited and/or temporarily restricted resources even surviving temporarily anaerobic conditions (Peck 2001).

In this work the shells of brachiopods where investigated. A schematic overview of the brachiopod shell growth is given in Figure 1.4. The investigated brachiopod shells belonged to individuals of the order of terebratulate brachiopods that mineralise calcitic shells. The investigated samples included species from special habitats like the deep sea (*Kakanuiella chathamensis*) and the Antarctic ocean (*Liothyrella uva*) as well as animals from more moderate conditions (*Liothyrella neozelanica* and *Gryphus vitreus*).

The main morphofunctional relevance of the shell is probably protection of the organism (Rudwick 1970). Alexander (2001) however assumes five possible functions of the shell: (1) Protection of the soft tissue against predators, (2) stabilisation of the organism on the substrate and in the current, (3) facilitation of filtration in combination with the exclusion of sediment from the soft tissue, (4) augmentation of respiration and (5) dispersion of gametes and, if applicable, the brood of larvae.

Only 350 of of the 13000 known species are living today (Moore 2006, p. 214 et seq.). Their high abundance during the Paleozoic Era in combination with a fast evolution of their shells make them important index fossils. This high abundance together with their calcitic shells, which survive diagenesis better than aragonitic shells, make them furthermore ideal candidates for δ^{18}O measurements (Carpenter & Lohmann 1995, Yamamoto et al. 2010).
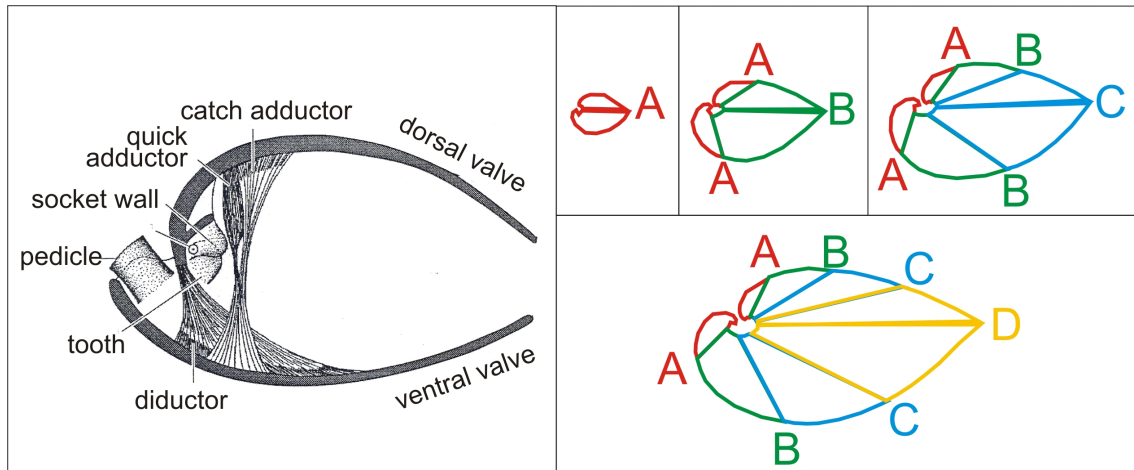
Figure 1.4: LEFT: Schematic sketch of the anatomy of a brachiopod. Modified after Peck (2001). RIGHT: Schematic overview of the growth of a simple, generalized brachiopod shell. Modified after Rudwick (1970).

Echinoidea - Sea Urchins

Echinoidea or sea urchins are marine animals living predominantly in benthal regions of the shelf sea. Regular sea urchins, as they were investigated in the present work, have a pentameric symmetry. A schematic sketch of their anatomy can be found in Figure 1.5a. Their inner organs are surrounded by a round corona consisting of single crystalline calcite plates. Onto the corona different kinds of spines are attached. This work investigates the calcitic, single crystalline primary spines. The morphofunctional role of these spines is interpreted as protection of the animal from structural damage (Strathmann 1981), but they are also used for locomotion. The spines, as well as the corona plates, are well studied objects that fascinate many scientists since long due to their single crystalline nature (Schmidt 1930, Donnay & Pawson 1969, Currey & Nichols 1967, Paquette & Reeder 1990, Su et al. 2000, Magdans & Gies 2004). The calcitic spines and coronal plates are highly porous on the micrometre scale. This porous calcite is referred to as *stereom.*

Regular sea urchins commonly feed by grazing algae and other organisms from the substrate with their calcitic teeth. The teeth are part of the masticatory apparatus known as the *Aristotle's lantern* (Figure 1.5b)[5]. The teeth are the second sea urchin biomineral that is investigated in this work. The grinding of the teeth that occurs during feeding is exploited in a self-sharpening mechanism. The constant wear down of the teeth requires a constant regrowth. A complete regeneration of the teeth of *Strongylocentrotus purpuratus* carried out under laboratory conditions lasted for two to three months (Holland 1965). Since Aristotle (350 B.C.) a number of studies has been published on the function and morphology of sea urchin teeth (e. g. Salter 1861, Giesbrecht 1880, Märkel 1969, Märkel & Gorny 1973, Stock et al. 2003, Robach et al. 2006, Robach et al. 2009). Section 3.6 contributes to a deeper understanding of the sea urchin teeth microstructure and texture.

---

[5]This name dates back to Aristotle who described the masticatory apparatus of sea urchins as horn-lantern like objects (Aristotle 350 B. C.).
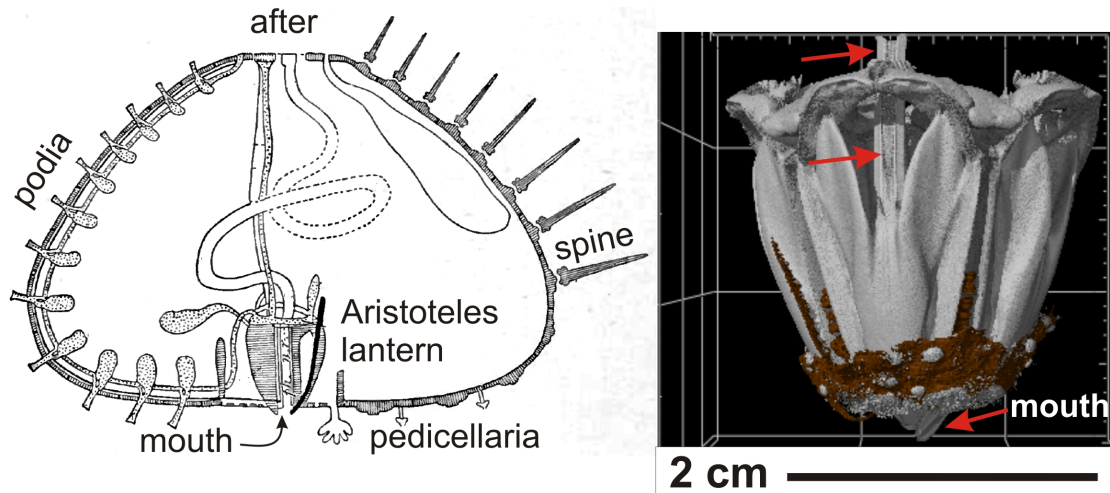
Figure 1.5: LEFT: Schematic sketch of a regular sea urchin. The mouth can be found in the lower part of the animal. Exemplary spines, podia and pedecellaria are shown. Figure modified after Gregory (1900). RIGHT: Computed tomography of the Aristotle's lantern, the masticatory apparatus of sea urchins. The 5 sea urchin teeth are surrounded by skeleton plates. the position of one tooth is marked by red arrows. The brown colours indicate presence of organic tissue on the investigated sample.

1.3.3 Material Science

Engineering materials often outclass biologic materials in their specific material properties. However, biomaterials such as biominerals have very impressive material properties even though they are built from a few abundant light chemical elements such as C, N, O, H, Ca, P, S, Si, Mg and others (Fratzl & Weinkammer 2007). Man made materials like modern highly optimized steels in contrast achieve their special material properties often from a complex chemistry and processing to control microstructures. They contain beside Fe and C a variety of rare elements such as Nb, V, Cr, Co, Ni, W, Mo, V, Ta, and others.

Engineering structures are designed for a special function. The material and geometry of an engineered object are chosen depending on its function before its production. They can not (or only very limited way) be adjusted after its production. An excellent example for how different biominerals are in this respect is the biomaterial bone: Bone can adapt its geometry according to its need, e.g. if the organism grows. Also the material properties are adjustable depending on the needs by tailoring the ratio of the structural elements, a hard mineral phase and a soft organic phase, form which bone is formed (Layne & Nelson 1999). The probably most intriguing fact is that bone can even reassemble after a complete fracture.

As all biominerals are produced at body temperature also the energy consumption in the process of mineralisation is low compared to man-made materials like steel, aluminium, concrete or glass. A good example for the low energy production of biominerals are glass sponges that mineralize their skeleton from silica glass at body temperature using a collagen template (Ehrlich et al. 2010).

Calcite ($CaCO_3$) is a material that has a very unfavourable combination of material properties: it is very *soft* having a Moh's hardness of 3 and still highly *fragile* due to its pronounced cleavage. However, the animals investigated in this study, brachiopods and sea-urchins, use this material as a protective shell or as teeth and they are not the only ones (Table 1.1). The calcite we find in biomaterials is harder than geologic calcite (Sections 3.2 & 3.6) and the cleavage of inorganically precipitated calcite is not present in the calcite formed by biocontrolled mineralisation.

The reason why biomineral-skeletons are strong and resistive materials compared to the inorganically formed equivalents is that they are highly optimized composite materials (e. g. Fratzl & Weinkammer 2007, Schmahl et al. 2008). Biomineral skeletons usually combine stiff mineral components with tough organic components. The mineral components are typically not very tough but vulnerable to fracture. The organic components in contrast are tough and can thus dissipate cracks. The composite is constructed on different hierarchical levels leading to complex materials with excellent properties (e. g. Wegst & Ashby 2004, Fratzl & Weinkammer 2007, Meyers et al. 2008, Schmahl et al. 2008, Dunlop & Fratzl 2010).

The $CaCO_3$-biomaterial that gained the most attention in respect to its microstructure is *nacre*. Nacre occurs in in mollusc shells. It is usually found in the inner layer of the shell and the outside layer consists of a more brittle calcitic columnar layer (e. g. Pérez-Huerta et al. 2011). The microstructure of nacre consists of aragonite platelets that have dimensions of about $8\,\mu m * 0.4\,\mu m$ in the shell of *Haliotis rufescens*[6] (Barthelat & Espinosa 2007). The platelets build a brick wall structure and are embedded in proteins/chitin (Smith et al. 1999, Weiss et al. 2002) and can be regarded as the cement in the brick-wall analogon (Figure 1.6). The composite material nacre consists roughly of 95% aragonite and 5% organic constituents (Barthelat & Espinosa 2007).

Microstructural optimizations present in nacre result in an extraordinary mechanical strength. The strengthening effect of this organic/inorganic composite structure compared to the pure brittle mineral has been subject of many studies (e. g. Currey 1977, Wang et al. 2001, Barthelat et al. 2007, Barthelat & Espinosa 2007). The organic matrices in combination with the microstructure lead to extraordinary mechanical properties like a 30 times higher toughness than pure inorganic aragonite[7] (Barthelat & Espinosa 2007). The extraordinary mechanical properties of nacre are attributed to several optimizations. It is worth to take a closer look at these optimizations as the principles also apply for the calcitic biominerals investigated in this work:

Due to the *composite structure* of biominerals a large number of interfaces of organic and inorganic compartments occur which leads to crack deflection, to crack bridging and, in the case of nacre, to a plate pull-out. All these processes dissipate energy and thus impede the catastrophic failure of the shell (e. g. Wang et al. 1995, Menig et al. 2000, Dunlop & Fratzl 2010). In nacre this is achieved by the brick-wall microstructure.

---

[6] These values apply for the shell of *Haliotis rufescens*, the red abalone. The platelets of nacre in other species can vary but all are in the same order of magnitude.

[7] Older work mentions 1000-3000 times higher toughness of nacre compared to inorganic aragonite. However, there are no reliable data published that supports these extraordinarily high values.

The soft organic matrix generally reduces the brittleness of the composite biomaterials (e.g. Schmahl et al. 2008, Dunlop & Fratzl 2010) compared to the pure inorganic counterparts. The importance of the organic matrix in nacre can be seen by the fact that dry nacre has a similar toughness as inorganic aragonite whereas wet nacre shows an increase in toughness (Barthelat & Espinosa 2007) by the factor of 30. This strong increase arises from *macromolecular optimizations* in the soft organic matrix that enhance the mechanic properties of the material. Some of the biomolecules present in the organic membrane have the capability to stretch (Smith et al. 1999). During the process of stretching the tertiary protein structure is changed and sacrificial interchain-bonds need to be broken and thus more energy is necessary to break the composite (Smith et al. 1999). The efficiency of this process is enhanced as the sacrificial interchain-bonds reconstitute after unload.

The *mesocrystalline structure* of biominerals also enhances the mechanical properties of these materials. In nacre every platelet consists of polygonal nanograins. This structuring makes the platelet better deformable than monolithic aragonite (Li et al. 2004).

Topological optimizations could be identified in nacre on different scales: Computer simulation studies showed that the size and aspect ratio of the brittle mineral platelets maximize the inelastic strain capacity (Evans et al. 2001). The aragonite platelets are not perfectly flat but are slightly waved (indicated in Figure 1.6) leading to a strain hardening when force is applied perpendicular to the short axis of the platelets. This strain hardening arises as the platelets can not slide past each other but get stuck (Barthelat & Espinosa 2007). Furthermore nanoasperities were found on the surface of the tablets that also resist a sliding of tablets and thus enhance the shear resistance (Wang et al. 2001, Evans et al. 2001). Computer simulation studies showed that also the size and abundance of these asperities is optimized to provide maximum strain hardening (Song & Bai 2003, Song et al. 2003). The number of nanoasperities ensures the formation of multiple dilatation bands. However, the number of asperities is below the level that leads to a internal plate fracture due to dilatation bands. In addition to the topologies mentioned above there are mineral bridges between the platelets that enhance the strength of the organic interface (Song & Bai 2003, Song et al. 2003).

Occasionally certain material optimizations of biomaterials can be copied by engineers. Examples for this are the work of Tang et al. (2003), who were able to construct a highly resistive nacre-like microstructure from a clay mineral composite, and the work of Presser et al. (2009), who enhanced the material properties of corundum ceramics by copying the microporosity of sea urchin spines. However, biominerals are *hierarchically structured* materials (e.g. Fratzl & Weinkammer 2007, Meyers et al. 2008, Schmahl et al. 2008, Dunlop & Fratzl 2010) and most of the biomimetic approaches could only copy the optimizations of one hierarchical level. One exception is the recent fabrication of a bone-like hierarchical microstructure (Nassif et al. 2010). However, beside the disappointing fact that this material produced by Nassif et al. (2010) has essentially the material properties of collagen, it seems problematic to manufacture hierarchical composites on industrial scales.
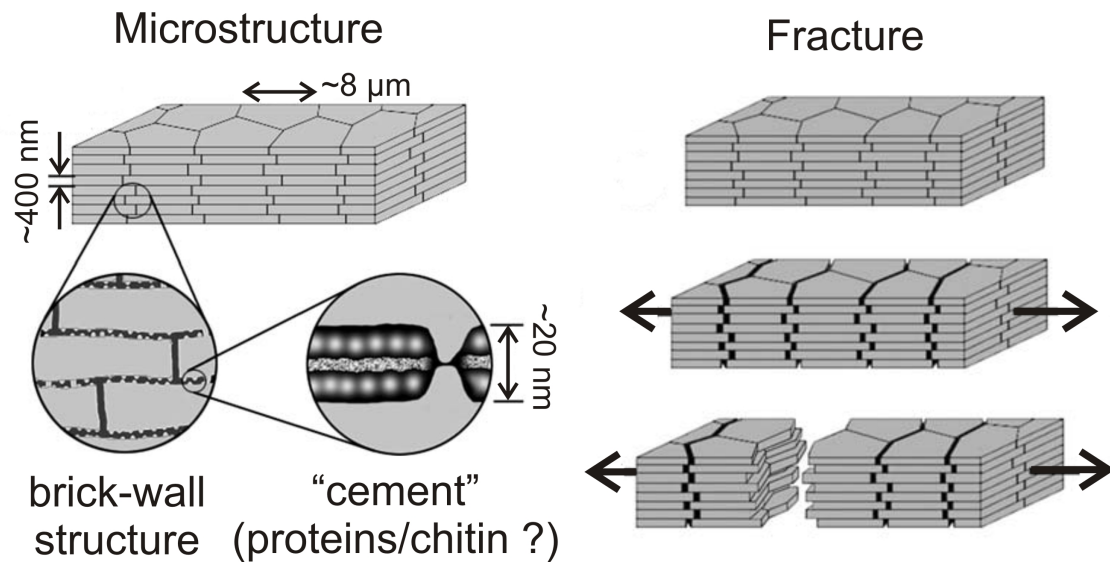
Figure 1.6: LEFT: Microstructure of nacre. Aragonitic platelets are arranged in a brick-wall structure. As cement serve proteins or chitin. Single optimizations as the waviness of platelets and nanoasperities are shown in the downer left image. RIGHT: Behaviour of the microstructure under load showing first the initial microstructure, then deformation and finally the fracture. Figure modified after: Barthelat & Espinosa 2007

1.3.4 Paleoclimatology

In order to reconstruct seawater chemistry and temperature from stable isotopes, minor and/or trace element concentrations are investigated (e.g. Denison et al. 1997, Veizer et al. 1999, Buggisch et al. 2003, Borremans et al. 2009, Hermans et al. 2010, Yamamoto et al 2010, Brand et al. 2011). A variety of studies uses therefore fine grained micritic sea-floor sediments (e.g. Denison et al. 1997, Buggisch et al. 2003) as they are easily accessible (Brand et al. 2011). However, sea floor sediment is always altered during diagenesis, e.g. it is not clear how changes from aragonitic to calcitic oceans change the sediment (Sandberg 1983, Brand et al. 2011). The study of brachiopod shells instead has the advantage that they consist of low-Mg calcite, a phase the is usually the end product of diagenesis. Most other animals mineralise aragonite that is transformed to calcite during diagenesis and the high abundance of brachiopods throughout the Palaeozoic makes them ideal candidates as proxies for the paleotemperature of oceans by analysing their $\delta^{18}O$ isotope ratios (e.g. Veizer et al. 1999, Brand et al. 2011) . The utilisation of brachiopod shells is based on the assumption that oxygen isotopes are incorporated into the shell in equilibrium with the ocean water. It is generally believed that this is the case in the *secondary* and *tertiary shell layer* (Carpenter & Lohmann 1995, Yamamoto et al. 2010) whereas the *primary shell layer* is not precipitated in isotopic equilibrium.

However, also brachiopods are not free of diagenetic overprint. Whereas older works tried to overcome this problem with high numbers of investigated individu-

als (e. g. Veizer et al. 1999 investigated 2128 shells), younger work concentrates on samples that have a well preserved microstructure and that lack features of diagenetic alteration (cf. Brand et al. 2011). To identify microstructurally well preserved shells the microstructures need to be well-known. Sections 3.2 & 3.3 deal with recent brachiopod shell microstructures and they can be used to identify unaltered microstructures.

Some authors try to correlate the Mg/Ca ratio of sea urchin calcite to either the Mg/Ca-ratio of the ocean habitat (Dickson 2002, Dickson 2004, Ries 2004) or even use it as a paleothermometer (Borremans et al. 2009, Hermans et al. 2010). These papers are based on the assumption that Mg is incorporated into sea urchin calcite in equilibrium with the ocean water surrounding the animal. The validity of this assumption is challenged in Section 3.5.

2 Samples and Methods

2.1 Investigated Samples and Applied Methods

Major experimental techniques used in this work were *scanning electron microscopy* (SEM), *electron backscatter diffraction* (EBSD), *electron microprobe analyses* (EMPA), *transmission electron microscopy* (TEM), *x-ray diffraction* (XRD), Vickers Microhardness Indentation (VMHI) and *nanoindentation*. This work was conducted in the laboratories of three different universities (LMU Munich, Universität Ulm, Ruhr-Universität Bochum) and five different research facilities (MPI für Metallforschung Stuttgart, KIT Karlsruhe, MPI für Eisenforschung Düsseldorf, DLR Köln, CEASAR Bonn). This resulted in a high variety of different methods and a number of different machines used for similar characterisations, e. g. six different SEM were used during this study. The reader is referred to the *samples and methods*-section within each section in Chapter 3 where the used methods for the corresponding section are described in detail. These sections also provide details about the origin and preparation of the investigated samples.

The current chapter will focus on the discussion on technical advances in the field of EBSD analyses that were made during the work on this dissertation.

2.2 Electron Backscatter Diffraction Analyses

2.2.1 Fundamentals of Electron Backscatter Diffraction Analyses

EBSD, also referred to as *orientation imaging microscopy* (OIM), is an SEM based technique to characterise the crystallographic and microstructural properties of a crystalline material. It is a diffraction technique in which *electron backscatter diffraction patterns* (EBSP, Figure 2.1a) are collected in a SEM. These EBSP can be indexed if one or more phases are given as possible solutions (Figure 2.1b). As a result of the indexation the phase and its crystallographic orientation are obtained (Figure 2.1c). Pattern collection and indexation is highly automatized and is rather fast (about 1 s/point in the LMU-system as used in Sections 3.4 & 3.6).

By scanning uniform (hexagonal or rectangular) grids on the sample surface large EBSD maps are obtained. The information of such a dataset can be represented in three different ways: two dimensional *maps* of phase- and orientational information (Fig 2.2 left), (inverse) *pole figures* (Fig 2.2 right) and *orientation distribution functions* (ODF). As in this work no ODF are directly presented they will not be
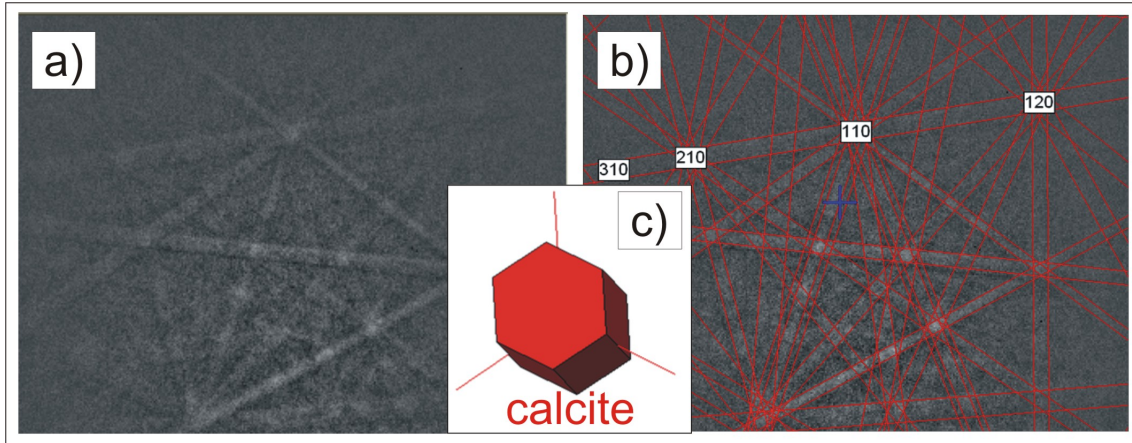
Figure 2.1: a) Typical EBSP of calcite. The diffraction lines correspond to lattice planes. b) Red lines indicate to the result of the indexation of the EBSD pattern. c) Illustration of the crystallographic orientation shown in b).

discussed here. Pole figures and maps are used within all sections of this work that deal with EBSD. They were calculated either with HKL CHANNEL 5, EDAX OIM SUITE or with own code written in WOLFRAM MATHEMATICA that is based on the equations that are shown below.

Under standard conditions (field emission gun SEM and 20 kV accelerating voltage) the lateral resolution of EBSD determined on calcite was described to be around $0.5\,\mu m$ and the angular resolution around 0.5° (Schmahl et al. 2008). During the preparation of the present thesis, the lateral resolution could be improved to around 200 nm (Section 3.3) and the angular resolution to 0.1° (Section 3.4). The increase of the angular resolution (Section 3.4) allows to access small *misorientations*[1] within EBSD datasets. During the work on the angular resolution an algorithm had to be developed to plot highly resolved pole figures. Furthermore new ways of data representation of conventional maps were developed to better demonstrate small orientational variations.

2.2.2 Data Representation

Pole Figures

Crystallographic orientation is reresented in pole figures and inverse pole figures. Pole figures represent the orientation of the crystal with respect to the sample whereas inverse pole figures present the orientation of the sample with respect to the crystallographic orientation. In this work inverse pole figures are used only indirectly for colour coding and thus do not play a major role. Pole figures in contrast are used extensively and their calculation is now discussed in detail.

---

[1]The term *misorientation* refers to the difference between two orientations.
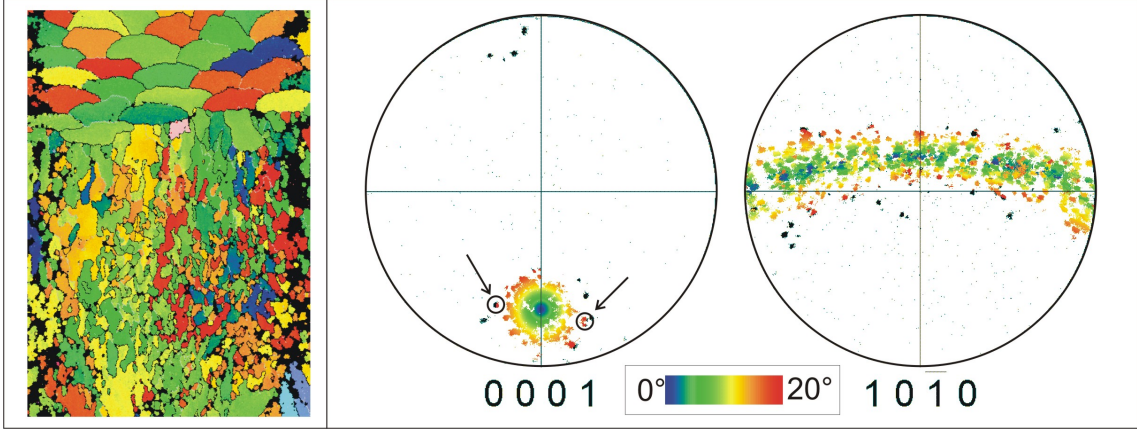
Figure 2.2: LEFT: EBSD map coloured after the tilt of the c-axis relative to the blue orientation. RIGHT: corresponding pole figures. Every point on the pole figure has the colour as it appears in the map on the left. Note that the areas in circles have very different orientations (c-axes are tilted by 40°) but appear in the same colour.

Note that all the following considerations are based on the unit sphere/circle with a radius of $r = 1$.

The orientation of a crystal in space is described by the orientation of the co-ordinate system defined by the crystal lattice. The EBSD data collection software FLAMENCO exports the calculated crystallographic orientation of each measured point as a set of Euler angles. The Euler angles describe the orientation of an object relative to a reference orientation. Every orientation in space of an object can be achieved by a rotation of the object around three independent axes. The rotations need to be applied in a certain sequence (Figure 2.3). The degree of rotation is given in three Euler angles (φ_1, Φ and φ_2) that are used after the convention of Bunge (Bunge & Esling 1986, see also Figure 2.3). To convert from one Cartesian to another Cartesian coordinate system[2] the Eulermatrix E is used:

$$E = \begin{pmatrix} cos\varphi_1 cos\varphi_2 - sin\varphi_1 sin\varphi_2 cos\Phi & sin\varphi_1 cos\varphi_2 + cos\varphi_1 sin\varphi_2 cos\Phi & sin\varphi_2 sin\Phi \\ -cos\varphi_1 sin\varphi_2 - sin\varphi_1 cos\varphi_2 cos\Phi & -sin\varphi_1 sin\varphi_2 + cos\varphi_1 cos\varphi_2 cos\Phi & cos\varphi_2 sin\Phi \\ sin\varphi_1 sin\Phi & -cos\varphi_1 sin\Phi & cos\Phi \end{pmatrix} \qquad (2.1)$$

Pole figures represent orientations of crystallographic directions or planes. This work deals exclusively with EBSD measurements on calcite. Calcite is crystallizing in the trigonal system and the hexagonal setting is used throughout this thesis:

$$\alpha = \beta = 90°, \, \gamma = 120°, a = b \neq c \qquad (2.2)$$

The orientation of a calcite crystal in space can be represented by the orientation of two linearly independent directions, e.g. the a*- and c-axes. From eq. 2.2 it can be found that:

$$a^* \perp c \qquad (2.3)$$

---

[2]The investigated material, calcite, is trigonal. The conversion from a trigonal to a Cartesian coordinate system is discussed in the following passage.

29
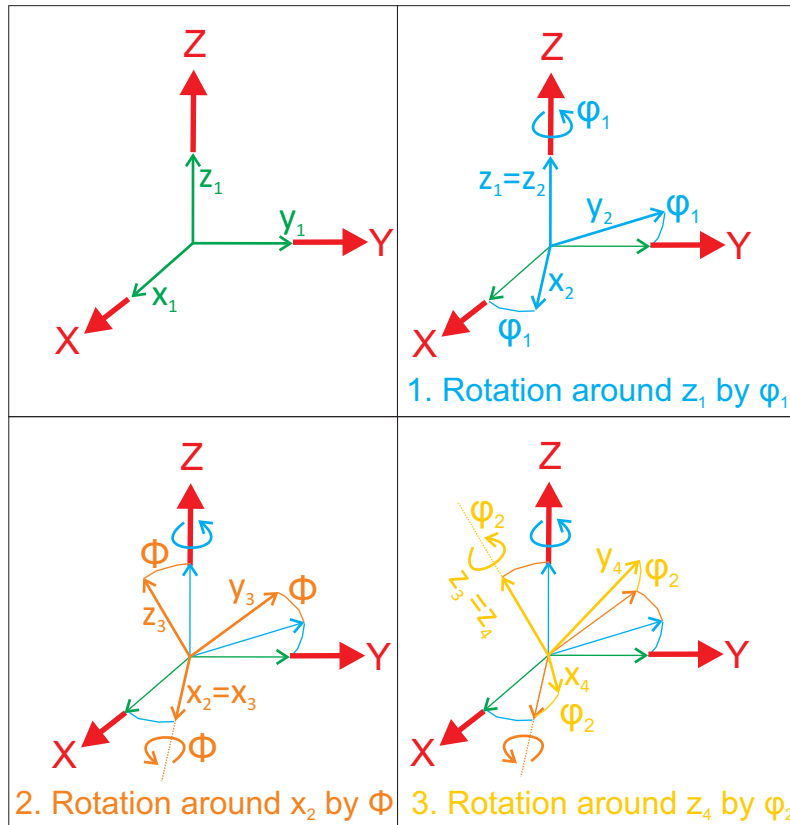
Figure 2.3: Successive rotation of the Cartesian coordinate system x_1, y_1, z_1 (green) to the coordinate system x_4, y_4, z_4 (yellow) via the Euler angle triplet $\varphi_1, \Phi, \varphi_2$. The coordinate system x_4, y_4, z_4 represents the orientation of a crystal within a reference coordinate System X,Y,Z (red). The reference coordinate system can be a sample or a laboratory system. Figure modified after Bunge & Esling (1981).

Therefore the a*-axes can be represented as the cartesian vector $\begin{pmatrix} 1 \\ 0 \\ 0 \end{pmatrix}$ and the

c-axes as the cartesian vector $\begin{pmatrix} 0 \\ 0 \\ 1 \end{pmatrix}$. The multiplication of these vectors with the

inverse Euler matrix will result in the unit vectors $\vec{u}_{100}$ and $\vec{u}_{001}$ that represent the orientation in space of (100) and [001], respectively:

$$\vec{u}_{100} = E^{-1} \cdot \begin{pmatrix} 1 \\ 0 \\ 0 \end{pmatrix} \tag{2.4}$$

$$\vec{u}_{001} = E^{-1} \cdot \begin{pmatrix} 0 \\ 0 \\ 1 \end{pmatrix} \tag{2.5}$$

The pole figures calculated by WOLFRAM MATHEMATICA and presented in Section 3.6 are the result of a stereographic projection of the upper hemisphere onto the equator plane. A graphic illustration and the definition of the symbols for the equator plane $E(x, y, 0)$, the centre point $C(0, 0, 0)$, the south pole $S(0, 0, -1)$, the

direction $\vec{u} = \begin{pmatrix} i \\ j \\ k \end{pmatrix}$, the point $U(i, j, k)$ and finally its projection $P(x_p, y_p, 0)$ is

given in Figure 2.4. The variables i, j, k are the coordinates of the point $U(i, j, k)$. The same variables i, j, k are also used as the vector components of the vector $\vec{u}$. The use of i, j, k in both, U and $\vec{u}$ is valid as we define $\vec{u}$ as a unit vector:

$$|\vec{u}| = \sqrt{i^2 + j^2 + k^2} = 1 \tag{2.6}$$

The stereographic projection of the point U results in point P. P is the intersection of the line SU and the equator plane E:

$$P = E * SU \tag{2.7}$$

Solving this equation leads to the coordinates of the projection point $P(x_p, y_p, 0)$:

$$x_p = \frac{i}{k + 1} \tag{2.8}$$

$$y_p = \frac{j}{k + 1} \tag{2.9}$$

To ensure that a point is projected inside a unit sphere the ranges of i, j, k are defined as:

$$i \in \{-1, 1\}, \, j \in \{-1, 1\} \, \text{and} \, k \in \{0, 1\} \tag{2.10}$$
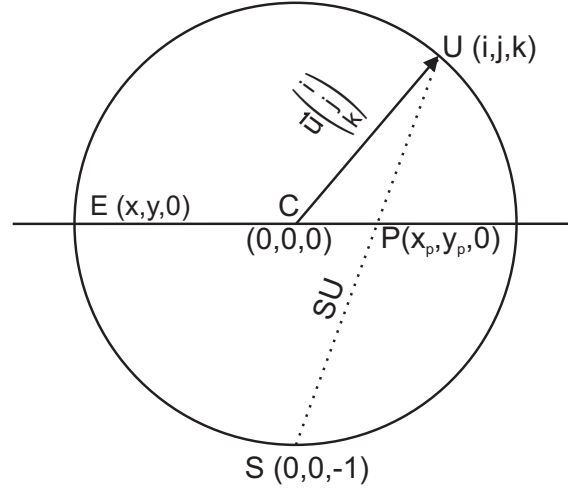
Figure 2.4: Sketch of the stereographic projection showing a section through a unit sphere with equator $E(x, y, 0)$, centre point $C(0, 0, 0)$, the south pole $S(0, 0, -1)$, a direction that is represented by a unit vector $\vec{u}_{i,j,k}$. If the origin of $\vec{u}_{i,j,k}$ is C it will touch the unit sphere in the point $U(i, j, k)$. The stereographic projection of $\vec{u}_{i,j,k}$ is the intersection of the equator with the line SU resulting in the point $P(x_p, y_p, 0)$.

The equations 2.4 and 2.5 can result in values of $k < 0$. However, the symmetry of calcite allows to use the absolute value of k for the calculation of pole figures of (100) and [001]:

$$x_p = \frac{i}{|k| + 1} \tag{2.11}$$

$$y_p = \frac{j}{|k| + 1} \tag{2.12}$$

2.2.3 Accessing Small Misorientations by EBSD

Data Representation - Resolution of Misorientations above 0.5°

The orientational differences in EBSD maps are usually presented in colour coded maps. The colour coding based on Euler angles is based on the *RGB-colour* model. In this additive colour model the three *primary colours* red, green and blue are added to produce a broad array of *secondary colours*. In Euler-angle coloured EBSD maps every Euler angle is represented by one primary colour. The higher the angle, the higher the contribution of the corresponding primary colour to the secondary colour. In commercially available software (e. g. CHANNEL 5) the Euler range that is given to each colour is defined by the symmetry of crystal system: i.e. in calcite each primary colour is represented with an angular range from 0° - 180°. The human eye is limited to distinguish only 200 hues (Eisel 2006) and thus small misorientations can not be distinguished in such a colour coding.

To overcome this problem, CHANNEL 5 allows the user to represent small misorientations by colouring the absolute value of the measured points from a distinct

orientation. An example for such a colouring can be found in Figure 2.2. The corresponding pole figure next to the colour coded map illustrates the problem of such a colouring: two points can have the same colour because they have the same tilt to the reference orientation even though they have very different orientations.

The biominerals investigated in this work showed a strong crystallographic preferred orientation and single grains show due to their mesocrystallinity a strong internal misorientation. This means that we need to consider small orientational deviations in the analysed datasets. To display these structural features a method was developed in WOLFRAM MATHEMATICA to adjust the range of plotted Euler angles. Thus, only angles from a small range of Euler angles are colour coded (illustrated in Figure 2.5). The adjustment of the plotted range of the Euler angles results in maps where small orientational differences can be differentiated accurately (Figure 2.5).

The method of adjusting the colour range of the Euler angles to emphasize small orientational differences is so successful that it was not only used for my own work (Section 3.6) but also in EBSD work that deals with otoliths (Schulz - Mierbach et al. in prep.) and mollusc shells (Hahn et al. in prep).

Adjustment of the measurement routine - resolution of misorientations down to 0.1°

To investigate very subtle (<1°) differences in crystallographic orientation the measurement routine of EBSD needs to be adjusted. It turned out that the averaging of the orientation of many measured points can increase the precision of EBSD (Section 3.4). As calcite is a non-conductive material continuous measurement of one point will lead to charging effects that again lead to a deformation of the diffraction pattern that results in a wrong calculation of the orientation. To avoid these charging effects small maps (10*10 = 100 points) with a step size of $1.5\,\mu m$ where measured.

In order to obtain datasets where an average orientation can be extracted a very careful sample preparation is necessary that results in a smooth and clean surface. Furthermore a number of geometric errors need to be excluded during the high angular resolution EBSD measurement:

1. The movement of the electron beam must be limited to a minimum. It may only move while scanning a map. For scanning the next map only the stage may be moved but not the beam.

2. The stage may only be moved parallel to the tilt-axis[3] of the sample relative to the detector. This is commonly achieved by moving the motor that changes the x-coordinate.

---

[3]during EBSD measurements the sample is tilted 70° away from the horizontal in order to achieve an angle of 20° between sample surface and EBSD detector. This tilt angle maximises the signal to noise ratio of the pattern.
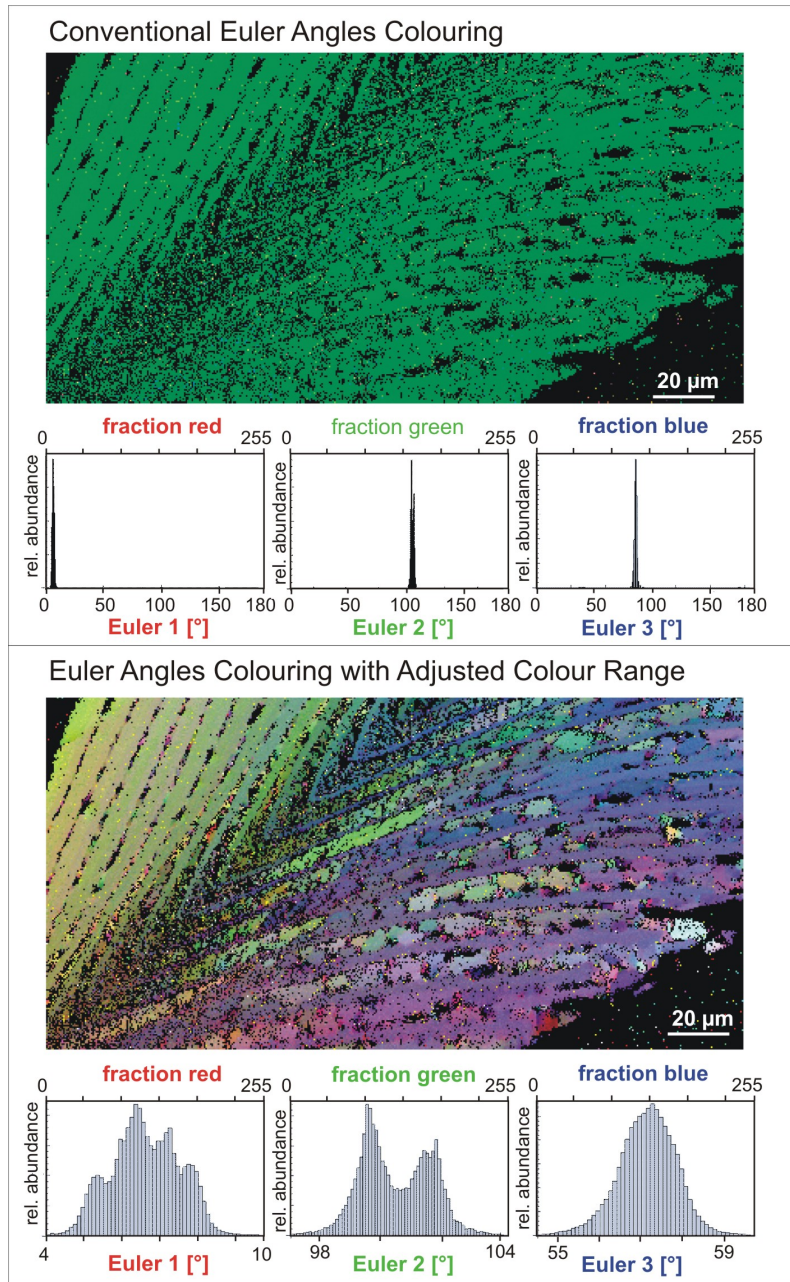
Figure 2.5: EBSD dataset collected on a sea urchin tooth. The upper map has a conventional Euler-angle colouring. The investigated area seems to be as like a single crystal with voids. The histograms below the map indicate that only one orientation and one colour can be distinguished. In the lower map, the colour range is adjusted to only represent the information within the maxima of the upper histograms. In this map single grains can be distinguished and the microstructure can be interpreted more accurately.

3. The focus should not be changed during measurement. Note that hysteresis in the electromagnetic lenses also forbids to change the focus and reset it later to the original values.

4. All measurements must be performed with the same calibration.

The calculation of an average orientation requires a normalisation of the orientation matrix, a mathematically not trivial procedure. To avoid the normalisation the average orientation was approximated as follows:

The normalized (100)- and [001]- orientation ($\vec{u}_{100}$ and $\vec{u}_{001}$, respectively) for every data point was calculated following eqs. 2.4 and 2.5, respectively. From the p=100 data points p (100)- and p [001]-orientations are obtained. They will be referred to as $\vec{u}_{i,100}$ and $\vec{u}_{i,001}$, respectively, with i as an integer between 1 and p. Subsequently the average orientation ($\overline{V}_{100}$ and $\overline{V}_{001}$, respectively) was calculated from all data points:

$$\overline{V}_{100} = \frac{1}{p}\sum_{i=1}^{p}\vec{u}_{i,100} \quad \text{with} \quad \overline{V}_{100} = \begin{pmatrix} \overline{i}_{100} \\ \overline{j}_{100} \\ \overline{k}_{100} \end{pmatrix} \tag{2.13}$$

$$\overline{V}_{001} = \frac{1}{p}\sum_{i=1}^{p}\vec{u}_{i,001} \quad \text{with} \quad \overline{V}_{001} = \begin{pmatrix} \overline{i}_{001} \\ \overline{j}_{001} \\ \overline{k}_{001} \end{pmatrix} \tag{2.14}$$

The average orientations ($\overline{V}_{100}$ and $\overline{V}_{001}$, respectively) were then transformed into the unit vectors $\overline{U}_{100}$ and $\overline{U}_{001}$, respectively:

$$\overline{U}_{100} = \frac{\overline{V}_{100}}{\sqrt{\overline{i}_{100}{}^2 + \overline{j}_{100}{}^2 + \overline{k}_{100}{}^2}} \tag{2.15}$$

$$\overline{U}_{001} = \frac{\overline{V}_{001}}{\sqrt{\overline{i}_{001}{}^2 + \overline{j}_{001}{}^2 + \overline{k}_{001}{}^2}} \tag{2.16}$$

The distance (d_{100} and d_{001}) of every orientation ($\vec{u}_{i,100}$ and $\vec{u}_{i,001}$) from the average orientations ($\overline{U}_{100}$ and $\overline{U}_{001}$) was calculated as:

$$d_{100} = |\overline{U}_{100} - \vec{u}_{i,100}| \tag{2.17}$$

$$d_{001} = |\overline{U}_{001} - \vec{u}_{i,001}| \tag{2.18}$$

Only data points that have a distance smaller than three times the standard deviation of all distances are included in the following refinement. This procedure excludes random wrong indexations (*wild spikes*). Usually more than 95% of the data is within this range. The number of remaining data points is defined as the new value of p. From those remaining data points the average orientations of (100) and <001> and the distances of every observed orientation to the average orientation

are calculated again according to the procedure described before in eq. 2.13 - 2.18.

The average orientation is finally defined as the orientation where the sum of the distances d_{100} and d_{001} is lowest.

This procedure allows to avoid the calculation (and normalisation) of an average orientation. The error implied by this method was for all datasets below 0.01°.

2.2.4 High Lateral Resolution EBSD

The spatial or lateral resolution of EBSD is dertermined by the interaction volume for incoherent, elastic scattering processes induced by the primary electron beam. This interaction volume depends on the incoherent quasi-elastic scattering of the primary beam electrons and is influenced by mainly two factors: material properties of the sample and the energy of the primary electrons.

The material properties that influence the interaction volume are the atomic number and electronic properties of the sample material. A lower atomic number of the investigated material leads to a larger interaction volume. Calcite consists of the light elements Ca, C and O and can thus be only be investigated with low lateral resolutions compared to steels or most other metallic compounds. The lateral resolution on calcite was determined to be around $0.5\,\mu m$ using an accelerating voltage of $20\,$kV (Schmahl et al. 2008).

The energy of primary electrons is controlled by the accelerating voltage of the electron gun. A decrease of accelerating voltage leads to a decrease of the primary electron energy and thus to a reduction of the interaction volume (Ren et al. 1998, Steinmetz & Zaefferer 2010). This reduction results directly in a higher lateral resolution. The validity of these considerations was recently demonstrated (Steinmetz & Zaefferer 2010). The decrease of the accelerating voltage however results in patterns with a low *pattern quality* (defined by Wright & Nowell 2006), a measure of the signal-to-noise ratio.

The improvement of the lateral resolution of EBSD on calcitic samples was performed at the Max-Planck Institute for Iron Research (MPIE) in Düsseldorf. The used EBSD system was a prototype of a new generation of fast EBSD cameras. This camera allowed a fast collection of low signal to noise ratio diffraction patterns. This implies that the dwell time of the electron beam on one measured point was short compared to other devices. However, in the used SEM[4] problems arose on the sample due to beam damage: An amorphous carbon layer formed on the sample surface due to chemical cracking of organic molecules present within the sample. As the EBSD signal is obtained only from the upper $20\,$nm of the sample (e. g. Field 1997) a thin amorphous layer strongly decreases the pattern quality. To minimize these problems the beam aperture was reduced severely ($30\,\mu m$) to decrease the beam current and therewith the beam damage. However, this reduction of the aperture results in a comparably low collection speed: Maps were measured with $200\,$ms per frame with $15\,$kV accelerating voltage and $500\,$ms per frame with $10\,$kV accelerating voltage.

---

[4]a Zeiss 1540 XB dual-beam focused ion beam field-emission SEM, see Section 3.3

The relatively low collection speed resulted again in beam damage due to the high dwell time. Nevertheless EBSD measurements could be performed successfully. A further decrease in beam damage can be achieved by increasing the step-size of the measurement, a factor that naturally again decreased the lateral resolution. High lateral resolution EBSD measurements with 10 kV and 15 kV could be performed successfully on brachiopod shells (Section 3.3). However, the lateral resolution with 15 kV is better as a smaller step size (100 nm) can be chosen.

3 Results and Discussion

3.1 On the Structure and Formation of Biotic and Abiotic Schwertmannite

Abstract

We studied the structural variability of Schwertmannite as synthesized in different biotic and abiotic pathways from acidic solutions in the presence of sulfate. The biotic pathways included the bacterial strains *Leptospirillum ferrooxidans* EHS 2. The abiotic pathways started from ferric or ferrous-solutions and used various methods of oxidation and/or precipitation to produce the iron-oxy-hydroxy-sulfates. The hedgehog-like morphology of schwertmannite, which is common in biotic synthesis environments, was obtained in biotic but also in abiotic syntheses. Further, the hedgehog particles in both synthesis routes are solidly filled with precipitate. As they are not hollow they do not reflect overgrown bacteria. We further found that the contribution of bacteria such as Leptospirillum ferrooxidans EHS-2 to schwertmannite formation is limited to the oxidation of ferrous to ferric iron in acidic conditions. A substrate effect of EPS secreted by the bacteria cannot be ruled out. The schwertmannites obtained from various synthesis pathways gave slightly different x-ray diffraction profiles. In Rietveld refinements these differences could be attributed to a variation in the size and shape of coherently diffracting nanocrystalline domains. These domains are anisotropic with 5-11 nm along the channels and 1.8 - 2.4 nm perpendicular to the channels depending on the synthesis procedure. Mössbauer spectroscopy showed that the schwertmannite precipitates were purely ferric and contain octahedrally coordinated Fe(III) only.

3.1.1 Introduction

The mineral schwertmannite, a non-stoichiometric compound with an idealized composition of $Fe_8O_8(OH)_6SO_4$, occurs widely in environments with acidic iron- and sulfate bearing waters. In spite of its high abundance it has only been known since the 1990s (Bigham et al. 1990, Bigham et al. 1994). The late identification of this compound can be attributed to its lack of long range order and the corresponding absence of a distinctive and easily recognizable diffraction pattern. Moreover, schwertmannite shows x-ray diffraction (XRD) peaks overlapping with those of 6-line ferrihydrite. The physicochemical conditions for the formation of schwertmannite are met in acid mine drainage or acid rock drainage waters (e. g. Bigham et al. 1996, Kawano and Tomita 2001, Giagliano et al. 2004, Regenspurg et al. 2004, Parafiniuk and Siuda 2006, Adams et al. 2007, Kupka et al. 2007). In such regions the dissolution of pyrite liberates typically Fe and S. Bacteria oxidize the sulfur to sulfate and the iron to Fe-(III) whereupon the lower solubility of Fe-(III) compared to Fe-(II) leads to the precipitation of schwertmannite. Natural schwertmannite is known for building aggregates of whiskers which form hedgehog-like particles (Ferris et al 2004). It has been suggested that these hedgehog-like structures result from a - probably lethal - over-growth of the iron oxidizing bacteria by schwertmannite needles (Ferris et al. 2004).

Due to the amorphous to nanocrystalline nature of schwertmannite there is no final agreement on its structure. Bigham et al. (1990), who first described the mineral in detail, put forward the theory that schwertmannite has a β-FeOOH structure resembling that of akaganeite. This structure is similar to that of hollandite: the Fe-OOH octahedra form a structure with open channels that are filled with anions, in the case of schwertmannite with sulfate. In a recently published paper a structural model based on a disrupted β-FeOOH structure is described and evidence for this is given by pair distribution function (PDF) fitting (Fernandez-Martinez et al. 2010). However, the structural position of the sulfate was left open and remains up to now a matter of speculation. Some authors expressed doubts that the β-FeOOH model is correct for schwertmannite at all (Majzlan and Myneni, 2008) and even a goethite like structural element was proposed (Loan et al., 2004, Loan et al., 2005).

The porous channel-structure of schwertmannite created attention due to its sorption capacities for heavy metals or toxic complexes such as chromate and arsenate (e. g. Waychunas et al. 1995, Webster et al. 1998, Carlson et al. 2002, Regenspurg and Peiffer 2005, Burton et al. 2010). The studies that use synthetic schwertmannite use different ways to obtain it and the subsequent phase identification is usually performed by XRD. Due to the close-to-amorphous nature of schwertmannite the majority of diffractograms in literature exhibit a strikingly bad signal to noise ratio.

For an understanding of the bacterial influence on the precipitation of schwertmannite TEM samples of pure cultures of Leptospirillum ferrooxidans EHS 2 were analysed. To answer the question whether schwertmannite is indeed a structurally distinct single-phase material we synthesized schwertmannite materials by different biotic and abiotic pathways. The products were quantitatively analysed using Rietveld-analysis on XRD data showing a high signal/noise ratio. Furthermore temperature dependent Mössbauer spectroscopy from $4.2\,K$ to room temperature was conducted.

3.1.2 Materials and Methods

Samples and Sample Preparation

For this study schwertmannite was synthesized in several abiotic and biotic ways. The first synthesis method follows Bigham et al. (1990): 2 l of MilliQ water were heated to 60 °C and 10.8 g of $FeCl_3 \cdot 6 H_2O$ and 3 g of Na_2SO_4 were added. The solution was placed in an oven at 60 °C for 12 minutes. The orange suspension was then placed into dialysis bags (Carl Roth, Germany, cellulose, 2.5-3.0 nm) and dialyzed against MilliQ water. The water was exchanged daily during a period of 33 days. The precipitate was then filtered and vacuum dried. This sample are referred to as *dialyzed schwertmannite*. Note that this sample was prepared at 60 °C.

The second method for precipitating schwertmannite that was used in this study was first published by Regenspurg et al. (2004): 5 g of $FeSO_4$ were dissolved in 1 l of distilled water at room temperature. Then 5 ml of H_2O_2 (32%) were added. The solution became brown-red and after only few minutes, a rust-colored precipitate could be observed. After 24 h of ripening in solution the obtained material was vacuum-dried. We will refer to this material as *fast-H_2O_2-schwertmannite*.

To obtain an abiotic sample with conditions closer to the biotic schwertmannite syntheses, diluted H_2O_2 (0.03%) was pumped continuously for 24 h at a flow rate of 5 ml/h into 100 mL of sterile culture medium (iFe) containing 25 mM ferrous iron (Johnson and Hallberg, 2007) at 30 °C. After the oxidation of the ferrous iron the resulting precipitate was harvested by centrifugation (6000 g, 15 min) and freeze dried. This sample is refered to as *slow-H2O2-schwertmannite*.

Another abiotic synthesis method was described by Loan et al. (2004). An amount of 2.5 g of $Fe_2(SO_4)_3xH_2O$ was dissolved in 500 ml of MilliQ water in a glass bottle in a water bath at 85 °C, 60 °C, 50 °C, 40 °C, 30 °C respectively. Precipitation took place within 1 h for the 85 °C sample and within 3 days for the 30 °C sample. All precipitates were left in solution for at least 24 h before they were vacuum dried. These samples are called according to their synthesis temperature (e. g. *85 °C-Schwertmannite*).

For biosynthesis of schwertmannite, *Leptospirillum ferrooxidans* EHS 2 (Hedrich et al. 2009) was inoculated with bioactive THERMANOX foils (obtained from PLANO, Germany) in test tubes and incubated at 30 °C with shaking (120 rpm). The bacteria and the schwertmannite were found to be attached to these foils.

Samples for electron microscopy examination were fixed by different physical and chemical methods. These samples were obtained either as pieces of the THERMNAOX foils or from precipitate accumulated on the bottom of the culture vessel. The precipitate was filled into VISKING dialysis tubes (obtained at Carl Roth, Germany). For physical fixation the samples were high pressure cryo-fixed in a in Wohlwend HPF Compact 01. For transmission electron microscope (TEM) analysis the samples were freeze substituted in 1.6% OsO_4, 0.1% UA and 5% H_2O in acetone (Walther and Ziegler 2002). After rinsing three times in pure acetone samples were embedded in EPON. Using an ultramicrotome (Ultracut, Leica) and a 45° diamond knife (Diatome) 70 nm thick sections were cut. For scanning electron microscopy (SEM) analysis the high-pressure-cryo-fixed THERMANOX samples were freeze dried and coated with 3 nm of platinum. The chemical fixation was performed in 0.02 M

cacodylate buffer at pH 4.5 containing 1 wt.-% paraformaldehyde and 2.5 wt.-% glutaraldehyde. After dehydration in an isopropanol series (10%, 30%, 50%, 60%, 70%, 80%, 90%, 100%) the samples were transferred into acetone and subsequently into an acetone-EPON-mixture. After the evaporation of the acetone, the sample and the surrounding EPON was put into molds, hardened at 60 °C and cut to 70 nm thick sections as described above. The ultrathin sections were contrasted with lead citrate. For the chemical fixation of SEM samples that contain cellular material the THERMANOX foils were put into a 0.1 M cacodylate buffer at pH 4.5 containing a 0.125 % glutaraldehyde solution. To investigate the influence of organic matter three batches of bacterial pure cultures were analyzed. Every batch consisted of at least four culture vessels. For XRD and morphology analyses samples were taken from the bottom of the culture vessels and freeze dried. These samples are referred to as *biogenic schwertmannite.*

In blank tests THERMANOX foil was put into sterile iFe medium for 3 weeks. This approach did not lead to precipitation of iron oxides on the foil.

For the morphologic analysis by SEM the precipitates were put onto a conductive tab and coated with carbon. For the XRD analysis precipitates were put between two Mylar foils without the use of glue to prevent all unnecessary background intensity.

Rietveld refinements were performed with the program suite GSAS (Larson and Von Dreele 2004) using the EXPGUI-interface (Toby 2001) embedded in GSAS. A modified pseudo-Voigt function (Larson and Von Dreele 2004) for fitting wide peaks was chosen and the instrumental parameters GU, GV, and GW were calibrated by the refinement of a LaB6 standard. As convergence criterion 0.01 for the square of the sum of all parameter shifts divided by the corresponding parameter value was chosen and only converged refinements are presented in this work. The calculation of the size of coherent structural domains was performed as described by Larson and Von Dreele (2004) based on an Lorentzian broadening model and with a Scherrer constant of 0.9.

Characterization

XRD characterization was performed on an Oxford Diffraction diffractometer equipped with a 2D-Atlas detector, operating at 100 mm sample to detector distance and using Mo-Kα radiation (HOPG-monochromator). The information obtained by recording several frames of Debye-Scherrer rings on the 2D-detector was integrated to one-dimensional intensity vs. 2-Theta data by the diffractometer software (CRYSALIS PRO). The scattering from the Mylar foil and the instrumental background were subtracted during the post-processing. No evidence for any preferred orientation was observed, neither in intensity distributions along Debye-Scherrer rings nor by experiments taken with different sample orientations.

SEM characterization was performed in the field emission gun SEM JEOL JSM 6500 F and a Hitachi S5200 with an accelerating voltage of 4 kV in both cases.

In the TEM analyses the ultrathin sections were investigated with a Zeiss EM 10 transmission electron microscope at an accelerating voltage of 80 kV. Images were recorded on Agfa negative film. After development, the negatives were scanned and the resulting digital images were processed with standard graphics software. No other image processing apart from brightness and contrast correction was performed.

Mössbauer spectra were recorded between 4.2 K up to 293 K with a transmission spectrometer operated with a sinusoidal velocity waveform and using a 25 mCi source of ^{57}Co in rhodium. A liquid He bath cryostat was used for cooling the source and absorber to 4.2 K. Temperatures between 4.2 K and ambient temperature were obtained during the slow (several days) warming of the cryostat, with the source always being at the same temperature as the absorber. Isomer shifts are given with respect to the source, and a metallic iron foil was used for velocity calibration. The spectra were fitted with appropriate Gaussian distributions of Lorentzian-shaped lines for the magnetic sextets and quadrupole doublets (Carlson et al. 2002). Hyperfine fields, B_{hf}, were calculated as average values over the Gaussian distributions.

3.1.3 Results

SEM

The samples precipitated by the various methods applied in this study show different morphologies (Figure 3.1). The typical hedgehog shaped aggregates of whiskers can be observed in our biogenic schwertmannite samples. The aggregates have a typical diameters of around 1 μm. Our abiotic precipitates exhibit a variety of morphologies: fast-H_2O_2-schwertmannite appears as spherical particles with several hundreds of nanometers in diameter, dialyzed schwertmannite exhibits a broccoli-like surface.

To understand the origin of the different morphologies slow synthesis ways of schwertmannite were tested. The first method was to gradually decrease the precipitation temperature in an Fe-(III)-sulfate solution, as described by Loan et al. (2004). The gradual decrease of synthesis temperature down to 30 °C slows down the kinetics and the resulting product is schwertmannite exhibiting a hedgehog-like morphology (Figure 3.1C).

The second approach in which a bacterial culture medium is oxidized slowly at 30 °C with diluted H2O2 (slow-H_2O_2-schwertmannite) results in schwertmannite hedgehogs as well (Figure 3.1E).

The bioactive THERMANOX foils that were present in pure cultures of L. ferrooxidans EHS-2 are tightly covered with a lawn-like structure of schwertmannite whiskers (Figure 3.2). This lawn structure exhibits the same surface morphology as schwertmannite hedgehogs. Fragments of fractured schwertmannite lawn show that the inner part of this schwertmannite layer consists of a compact aggregate that exhibits a conchoidal fracture (Figure 3.2A). Single hedgehogs (Figure 3.2B) and bacteria (Figure 3.2C) appear on the lawn surface. Traces of fibrous structures that we interpret as extracellular polymeric substances (EPS, see discussion), are present. This EPS is connected to the bacteria as well as to the precipitated schwertmannite lawn (Figure 3.2C).

TEM

The analysis of the microtome sections of both, THERMANOX foil and sediment of the culture media show that the hedgehog whiskers surround a compact core aggregate with a diameter varying from hundreds of nanometers up to tens of microns (Figure 3.3a). In sections through the hedgehogs no traces of overgrown cells can
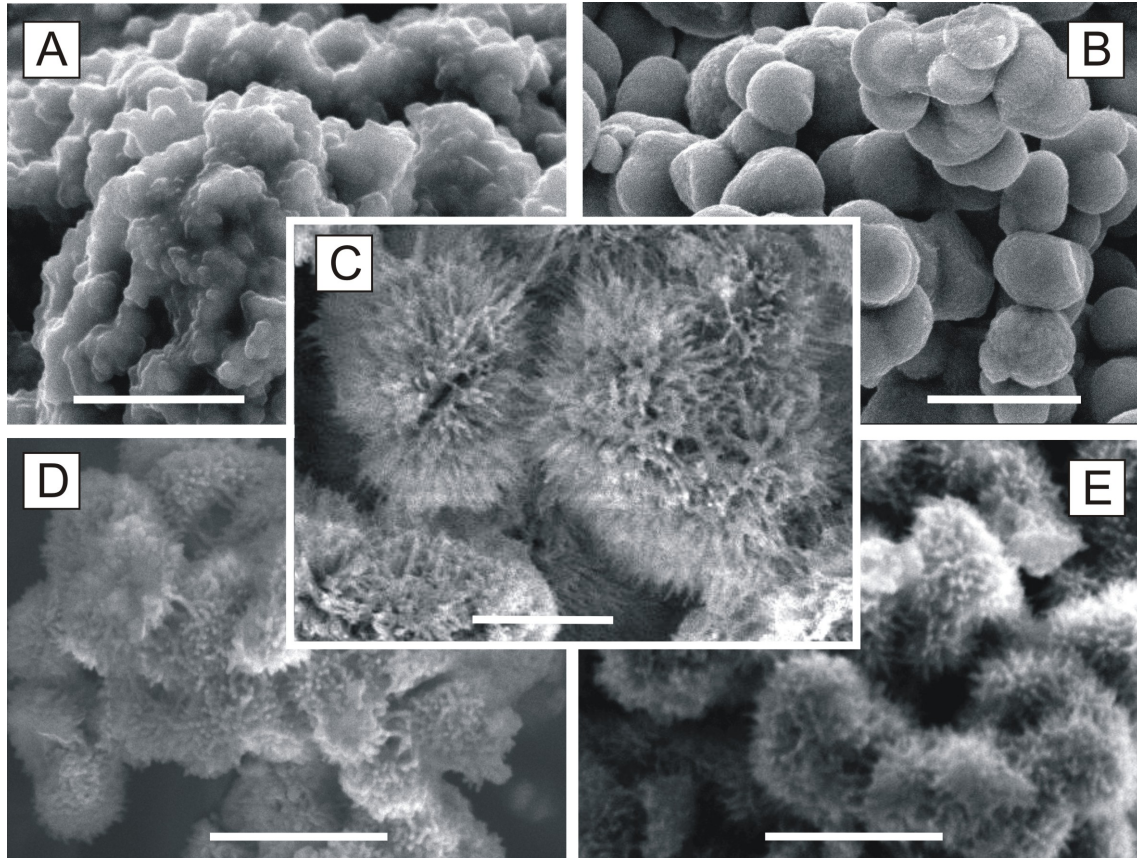
Figure 3.1: Microscale morphology of schwertmannites that were precipitated in different ways. A) schwertmannite precipitated in dialysis bags exhibiting a broccoli-like shape. B) fast-H_2O_2-schwertmannite, it consists of spherical particles of several hundred nanometers in diameter. C) schwertmannite precipitated with the temperature method abiotically at 30 °C. It shows the hedgehog structure and D) schwertmannite precipitated by the presence of bacteria showing the typical hedgehog structure E) ce-**H2O2**-schwertmannite showing the typical hedgehog structure. Scalebar is one micrometer.
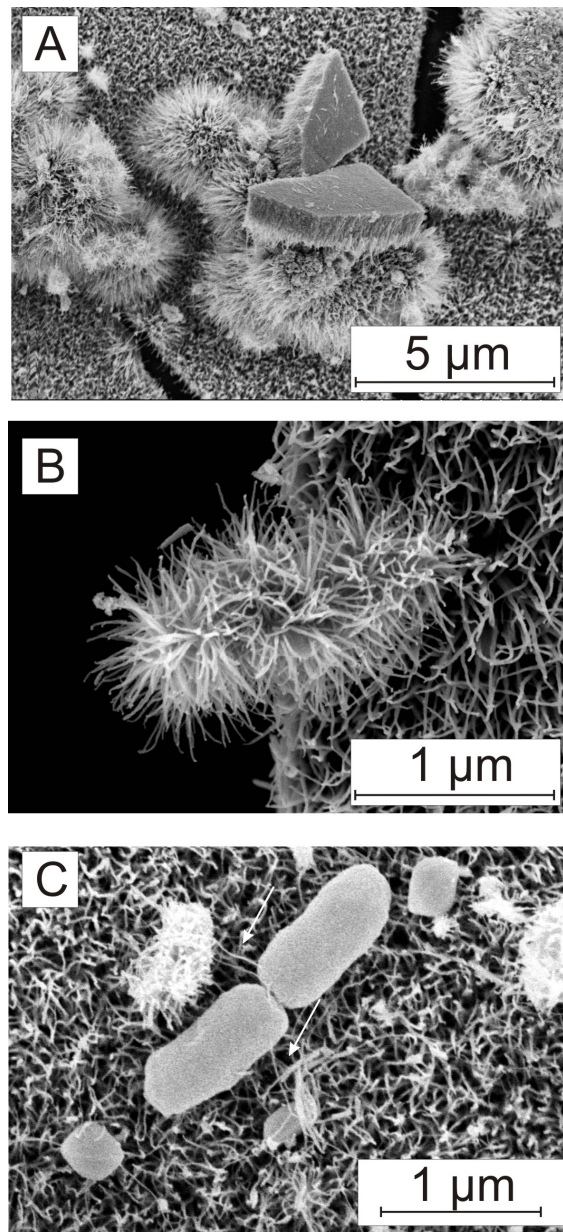
Figure 3.2: SEM images from pure bacteria cultures. A) a schwertmannite lawn that precipitated on the foil and several big hedgehogs. Fragments of the lawn can be seen in the center of the image. The lawn-like structure only appears on the contact to the solution whereas the iron oxide in contact with the foil is compact. B) typical hedgehog particle that can easily be mistaken as an overgrown bacterium. C) *Leptospirillum ferrooxidans* EHS-2 cell sitting on the schwertmannite lawn. The cell and the schwertmannite are connected by EPS filaments (arrows).
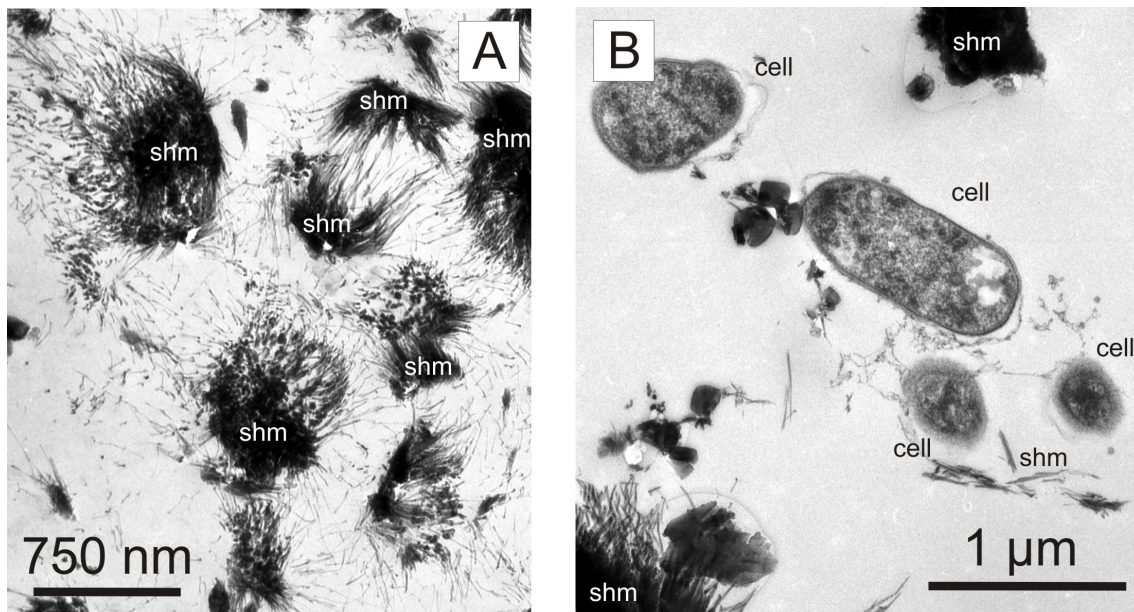
Figure 3.3: TEM images of samples of *Leptospirillum ferrooxidans* EHS-2. A) shows sections through schwertmannite hedgehogs. These hedgehogs are dense in their center and do not show any sign of bacteria in their inside. B) Typical scenery as observed in TEM investigations. It shows several cells that have no contact to schwertmannite (shm). The three cells on the right are connected by extracellular polymeric substances (EPS).

be found. Also we observed no other traces of organic matter within the mineral aggregates. Especially in the larger mineral aggregates ($<5\,\mu m$) an internal fracture resulting from the microtome sectioning is observed.

In both, chemically and physically fixed samples there are fibrous structures (Figure 3.3b) with a thickness between 10 and 30 nm. We interpret them as EPS (see discussion). The EPS forms a network that is connected to both cells and mineral. Within the network-forming EPS fibrils single schwertmannite needles can be found (Figure 3.3). We observed no attachment of schwertmannite whiskers on the bacteria.

XRD

Obtained data
Even though the differently produced schwertmannites show similar diffraction patterns there are distinct variations observable (see Figure 3.4 and Table 3.1).

The common diffraction maxima of the materials correspond to lattice plane distances (d-values) of 3.4, 2.55, 2.3, 1.95, 1.66, 1.5, 1.3, 1.04, and 0.99 Å (Table 3.1). As these maxima result from overlapping reflections we will not address them as single reflections in the following but as diffraction maxima or peaks.

The profile of the wide maximum at 3.4 Å varies from a rounded profile in the fast-H_2O_2, slow-H_2O_2 and the 30 °-schwertmannite to a triangular shape in biogenic-,

85 °C- and dialyzed-schwertmannite. In the cases of the slow H_2O_2-and the 30°-schwertmannite the peak contains a strong contribution at around 3.5 Å.

The maximum at 2.55 Å is the strongest and is similar in all diffractograms. It has a shoulder at 2.3 Å which is strongest in the 85°-schwertmannite and well pronounced in the biogenic and dialyzed schwertmannite. The intensity of this shoulder is one of the most distinctive features in the different diffractograms. The shoulder is weak in the cases of all H_2O_2-schwertmannites and the 30°C-schwertmannite.

A broad maximum at d=1.95 Å shows low intensity for all the different schwertmannite samples obtained in this study.

A relatively sharp maximum at 1.7 Å is observed only in the 85°C- and the dialyzed- (at 60 °C) schwertmannite. All schwertmannites show a XRD peak at 1.66 Å ; for the 85°C and the dialyzed-schwertmannite this is only a shoulder of the maximum at 1.7 Å.

The maximum at 1.51 Å has a sharper profile than all other maxima.

Rietveld refinements

The low crystallinity of schwertmannite allows the refinement of few parameters only. All refinements were performed with a linear background to ensure that no structural features are fitted by the background. Apart from the scale factor an overall Debye-Waller-factor was refined. The β-FeOOH (akaganeite) structure reported by Post and Buchwald (1991) was used as a starting model using only the iron-oxygen cage without the chloride. As a second model the schwertmannite structure proposed by Fernandez-Martinez et al. (2010, therein called "model 2") was refined, it will be referred to as the Fernandez-Martinez-structure or Fernandez-Martinez-model. The crystallographic b-axis of that model is parallel to the channels. Note that Bigham et al. (1994) used another initial setting where the c-axis is parallel to the channels. In the Fernandez-Martinez-model Fe and O show different Debye-Waller-factors. In our calculations, they were constrained and refined as one free parameter. Based on these two models we tried to design several variants containing SO_4 but the influence of this structural unit on the calculated diffractogram is so weak that the position of the sulfate cannot be determined. Accordingly the models that are presented here contain only Fe and O. These models are tested in a first step on a data set recorded for the fast-H_2O_2-schwertmannite.

For the β-FeOOH-structure the refinements (Table 3.2, Figure 3.5) lead to a somewhat similar diffractogram as the observed one. However, neither the strong reflections with d-spacings above 1.3 Å nor the weaker reflections below 1.3 Å can be described very well by this model. Beside background, scale factor and Debye-Waller-factor only a crystallite size model could be refined as free parameters. In nanocrystalline materials the size of the coherent structural domains can be understood as the "crystallite size" in diffraction experiments. The calculated size of coherent structural domains from the fit of an isotropic size model is 1.7 nm. A refinement of further parameters of the akaganeite model like lattice parameters and/or anisotropic line broadening cannot be achieved as efforts to adjust such parameters lead to divergence.

The Fernandez-Martinez-model turns out to be very stable as a starting model for Rietveld refinements and the results fit much better than the akaganeite model (see

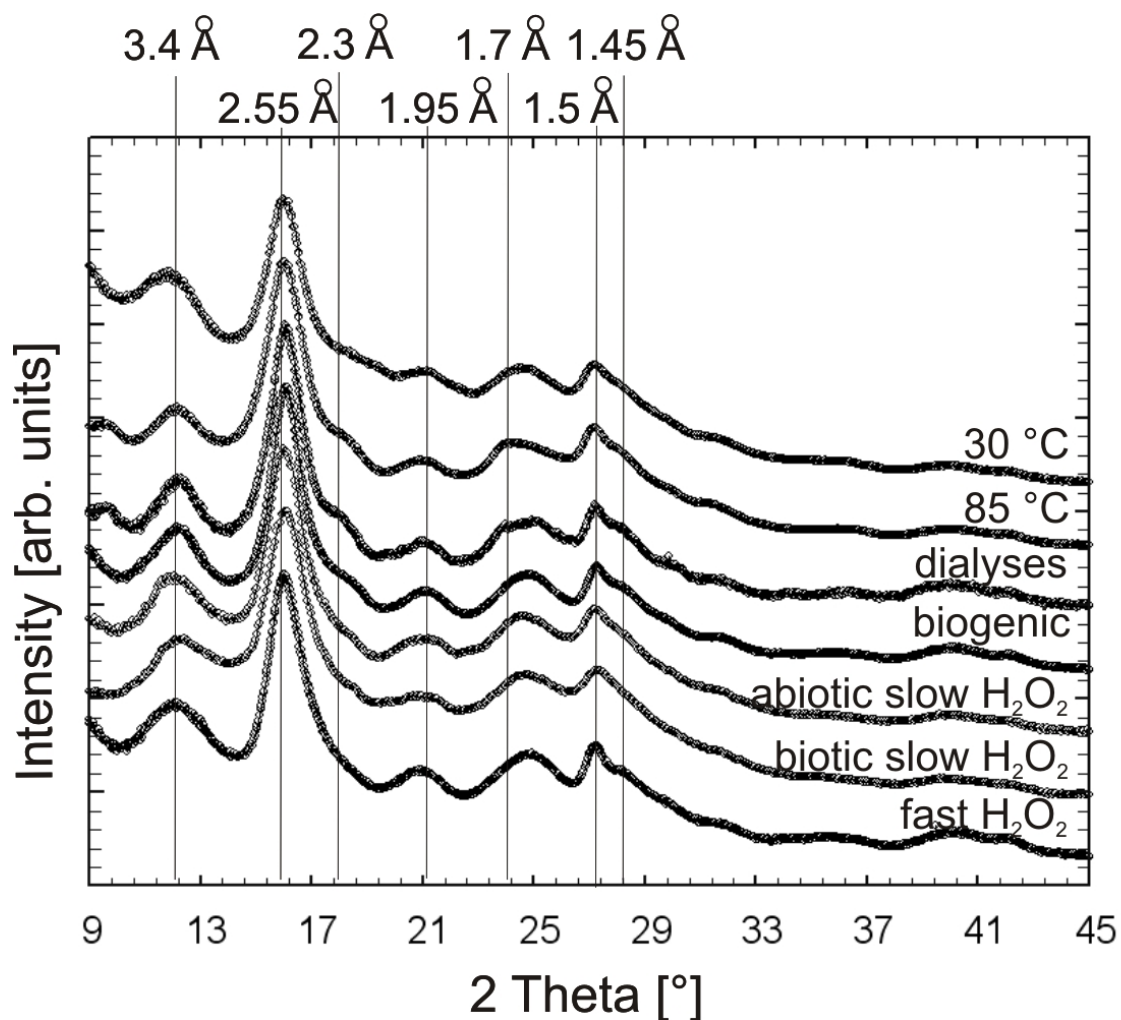Figure 3.4: Diffractograms recorded from schwertmannites precipitated in different ways. The most prominent reflections are marked by a line and the d-value is given above. There are distinct differences between different samples. Most prominent distinguishing features are the shoulder at 1.7 Å, the strong reflection at 1.45 Å, the shoulder at 2.3 Å and the reflection at 3.4 Å. Refer to Table 3.1 for further information

Table 3.1: Comparison of the XRD results of different schwertmannite samples compared to data of Bigham et al. (1994). The reflection at 4.86 Å is not within the investigated range. The hkl indizes are according to the cell after Bigham et al. 1994 (a=b=10.66 Å, c=6.04 Å)

| Data from Bigham et al. 1994			Biogenic schwert-mannite	85 °C schwert-mannite	Fast-H_2O_2 schwert-mannite	Dialysed schwert-mannite	Slow-H_2O_2 schwert-mannite	30 °C schwert-mannite
d [Å]	Relative intensity	hkl	Description of reflection relative to other samples					
4.86	37	200 / 111	n/a	n/a	n/a	n/a	n/a	n/a
3.39	46	310	wide and pointy	wide and pointy	wide and pointy	thin	wide and low	wide and low
2.55	100	212	strong	strong	strong	strong	strong	strong
2.28	23	302	pronounced shoulder	very pronounced shoulder	weak shoulder	pronounced shoulder	weak shoulder	weak shoulder
1.95	12	412	high	low	high	low	low	low
				additional peak at 1.7 Å		additional peak at 1.7 Å		
1.66	21	522	pronounced	shoulder of 1.7 Å reflection	pronounced	shoulder of 1.7 Å reflection	pronounced	pronounced
1.51	24	004	very sharp	very sharp	very sharp	very sharp	pronounced	pronounced
1.46	18	104 / 542	shoulder of 1.51 Å	shoulder of 1.51 Å	pronounced shoulder of 1.51 Å	pronounced shoulder of 1.51 Å	not detectable	not detectable
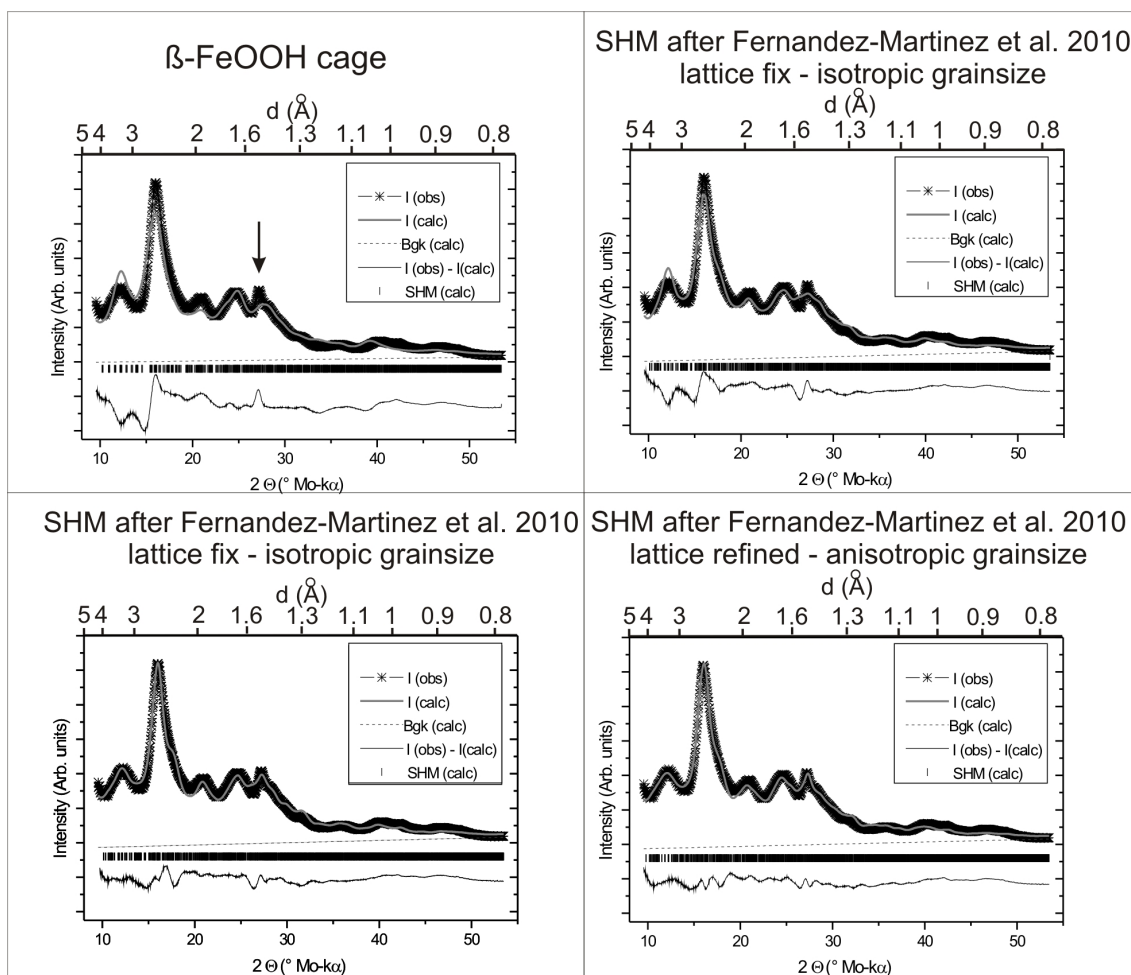
Figure 3.5: Rietveld refinements of fast-H_2O_2-schwertmannite. Top left graph shows the result of the refinement of the iron-oxygen cage of the β-FeOOH (Akaganeite) structure. Lattice and anisotropy of crystallite size could not be refined for this model. The other three graphs show the successive refinements with a model based on the Fernandez-Martinez-structure (see also Table 3.2).

Table 3.2: Parameters refined by Rietveld. "LX" and "ptec" are line broadening parameters refined in the Rietveld software (GSAS). From those parameters the (anisotropic) crystallite size is calculated. A refinement of further parameters of the akaganeite model cannot be converged or leads to divergence.

	Akaganeite lattice fixed - isotropic grain size model	Fernandez-Martinez model lattice fixed - isotropic grain size model	Fernandez-Martinez model lattice fixed - anisotropic grain size model	Fernandez-Martinez model lattice free - anisotropic grain size model
Space group	P1	P1	P1	P1
Lattice parameters	a=10.6 Å, b=6.066 Å, c=10.5 Å, α=90°, β=90.4°, γ=90°	a=10.86 Å, b=6.03 Å, c=10.47 Å, α=90°, β=92.1°, γ=90°	a=10.86 Å, b=6.03 Å, c=10.47 Å, α=90°, β=92.1°, γ=90°	a=11.16 Å, b=6.02 Å, c=10.36 Å, α=91.9°, β=90.7°, γ=87.7°
LX / Crystallite size parallel b-axis	211 / 1.7 nm	140 / 2.6 nm	193 / 4.2 nm	194 / 6.6 nm
ptex / Crystallite size perpendicular b-axis	n/a	n/a	-107 / 1.9 nm	-139 / 1.9 nm
Debye-Waller-factor	0.016	Fe:0.015, O:0.021	Fe:0.016, O:0.022	Fe:0.010, O:0.016
Number of refined parameters	5	5	6	12
χ^2	6.138	3.029	2.357	2.154

Table 3.2 and Figure 3.5 for results). In the first step only Debye-Waller-factor and a line broadening caused by an isotropic crystallite size were refined. The second refinement step assumes an anisotropic crystallite size. This improves the fit of the sharp peak at 1.5 Å and also of the 3.4 Å peak. An additional refinement of the lattice parameters leads to an appropriate description of the sharp 1.5 Å peak. The refinement of the anisotropic line broadening model results in a crystallite size of 6.6 nm along the channels and 1.9 nm perpendicular to the channels.

The Fernandez-Martinez model adapted as described above is then used as initial model for modelling the diffractograms of schwertmannites prepared after different recipes (see Table 3.2 and Supplementary Material 3.8). Convergence was tested repeatedly for different starting parameters to check for the effect of local minima. The lattice constants a, b, c were reproducible to within $\pm$ 0.01 Å, and the angles α, β, γ to +/-1°, but the lattice angles never shifted by more than 3° from 90°. The calculated crystallite size was reproducible within $\pm$ 0.2 nm when starting from different initial values. The refinements of the size of the coherently scattering domain show that the size along the channels (4.9 nm - 11.1 nm) is always higher

Table 3.3: Results of Rietveld refinement schwertmannites (SHM) produced by different recipes. "LX" and "ptec" are parameters calculated by the Rietveld software. From those parameters the (anisotropic) crystallite size is estimated. The aspect ratio is the crystallite size parallel b-axis divided by the crystallite size perpendicular to the b-axis.

	Fast-H_2O_2-SHM	Slow-H_2O_2-SHM	Biogenic-SHM	Dialysed-SHM	85 °C-SHM
Space group	P1	P1	P1	P1	P1
Lattice parameters	a=11.16 Å, b=6.02 Å, c=10.36 Å, α=91.9°, β=90.7°, γ=87.7°	a=11.02 Å, b=6.05 Å, c=10.36 Å, α=91.5°, β=91.1°, γ=87.4°	a=10.73 Å, b=6.01 Å, c=10.38 Å, α=91.5°, β=90.45°, γ=87.4°	a=10.65 Å, b=6.03 Å, c=10.44 Å, α=91.4°, β=90.0°, γ=87.2°	a=10.75 Å, b=6.06 Å, c=10.44 Å, α=91.2°, β=89.9°, γ=86.9°
LX / Crystallite size parallel b-axis	194 / 6.6 nm	152 / 4.9 nm	151 / 11.1 nm	176 / 9.6 nm	203 / 6.8 nm
ptex / Crystallite size perpendicular b-axis	-139 / 1.9 nm	-77.5 / 2.4 nm	-118 / 2.4 nm	-138 / 2.1 nm	-149 / 1.8 nm
Aspect ratio	3.5	2	4.6	4.6	3.8
Debye-Waller-factor	Fe:0.010, O:0.022	Fe:0.016, O:0.022	Fe:0.029, O:0.035	Fe:0.029, O:0.035	Fe:0.020, O:0.026
Number of refined parameters	12	12	12	12	12
χ^2	2.154	2.113	1.846	1.669	1.373

than perpendicular to that direction (1.8 nm − 2.4 nm, see Table 3.3). The highest aspect ratios (Table 3.3) can be observed for the biogenic- and dialyzed schwertmannites (4.6) followed by intermediate aspect ratios of 3.8 and 3.5 of the 85°C- and fast-H_2O_2-schwertmannite, respectively. The lowest aspect ratio is observed for the slow-H_2O_2-schwertmannite. The differences between calculated and observed curves show some common maxima. All refinements show maximum deviations from the observed data between d=0.9 Å and 1 Å. This can probably be attributed to a wrong background model and/or wrong atomic displacement parameters. The 85°C-, biogenic-, dialyses- and slow-H_2O_2-schwertmannite show maxima at 1.51 Å. This is probably due to inaccuracies in the description of the particle size and shape. These differences do not indicate the presence of a second phase.

Mössbauer spectroscopy

Mössbauer spectra of fast-H2O2-schwertmannite were recorded as a function of temperature between 4.2 K and room temperature with an absorber containing

$20\,\mathrm{mg}/cm^2$ of schwertmannite powder pressed into a lucite holder. A few spectra are shown in Figure 3.3. At room temperature, the spectrum is a broadened quadrupole doublet indicating a distribution of electric quadrupole splittings. For the maximum of the distribution the quadrupole splitting is $QS = 0.54(2)\,\mathrm{mm/s}$ and the isomer shift is $0.26(1)$, as is typical for ferric iron. The doublet is slightly asymmetric, with a wider spread of the quadrupole splittings towards larger values. The spectrum could be fitted with an asymmetric Gaussian distribution of quadrupole splittings, much like those of ferrihydrites (Mikutta et al. 2008, Eusterhues et al. 2008). There is no trace of divalent iron or trivalent iron coordinated other the octahedrally.

At 4.2 K the Mössbauer spectrum exhibits a magnetic hyperfine splitting into a six-line pattern that is again broadened, indicating a distribution of magnetic hyperfine fields (Figure 3.6). The outermost lines clearly show a broader wing towards the outside than towards the inside if the spectrum. This feature required fitting the spectrum with a superposition of two Gaussian distributions with different mean hyperfine fields and different variances of the fields and with a larger variance for the component with the larger field. The fields resulting from the least squares fit are B_{hf}=46.1(4) and 44.6(4) T and the respective variances $\delta B_{hf} = 3.4(1)$ and 1.1(1) T. The intensities of the two components are 32(1) and 54(1)%, respectively. The remaining 14% intensity was fitted as a very broad distribution of hyperfine fields that yields a structureless pattern but improved the adjustment of the slightly sagging baseline of the spectrum ($B_{hf} = 38(8)$ T; $\delta B_{hf} = (1)$ T).

Above 4.2 K the asymmetry of the outermost sextet components diminishes. Above 20 K the sextet could be fitted with a single Gaussian distribution of hyperfine fields, and the intensity of the broad structureless component increases. At about 40 K an additional quadrupole component becomes visible in the spectra. At 50 K this component is already quite pronounced, and above 60 K only the quadrupole doublet remains.

This behaviour is reflected in the mean hyperfine fields calculated as the weighted average over the fields of the individual components, including the zero field for the doublet component, which are shown in Figure 3.7 as a function of temperature. The results of the least-squares fit of the individual spectra are reproduced in supplementary material 3.4.

3.1.4 Discussion

Factors influencing the precipitation of schwertmannite

It is well-known that iron oxides can encrust bacteria cells (Schädler et al 2009, Kappler 2005). Naturally occurring schwertmannite often shows a morphology of micrometer sized round aggregates (referred to as schwertmannite hedgehogs in this work). The interpretation of the hedgehogs as bacteria overgrown by schwertmannite (Ferris et al. 2004) seems evident, but the present study shows that schwertmannite does not grow on the walls of *Leptospirillum ferrooxidans* EHS-2 as also proposed by others (Eneroth & Bender Koch 2004). Furthermore, sections through schwertmannite hedgehogs do not show any sign of bacterial cells inside, which may have acted as a nucleation site - the sections rather appear as massive mineral aggregates. We also showed that the hedgehog morphology can be produced by means of inor-
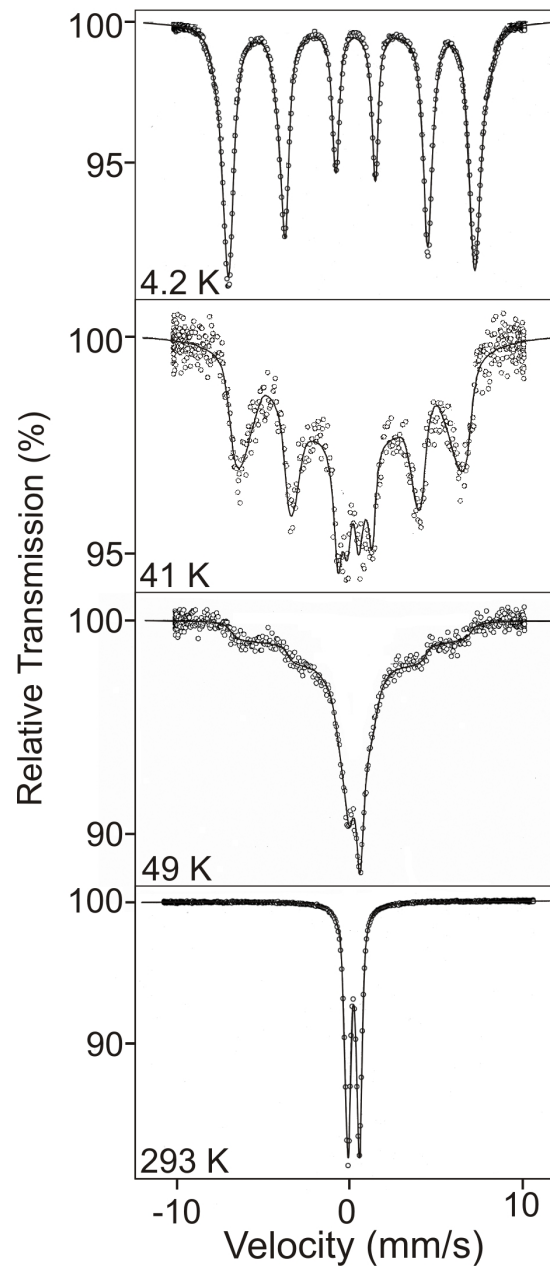
Figure 3.6: Fitted Mössbauer spectra of schwertmannite precipitated by H_2O_2. The temperature at which the measurement was performed is stated in the graph. At 4.2 K a purely antiferromagnetic spectrum is present. At 41 K the phase transition to a paramagnetic state is ongoing and it is nearly finished at 49 K. At room temperature the material appears as purely paramagnetic.
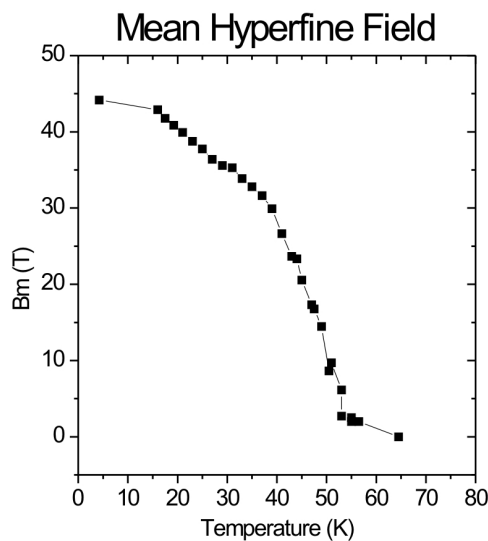
Figure 3.7: The mean hyperfine-field of fast H_2O_2-schwertmannite calculated from Mössbauer spectroscopy as a function of temperature.

ganic precipitation. This underlines the independence of the hedgehog morphology from the morphology of bacterial cells.

In a comparative study between different microbial strains, Schädler et al. (2009) described how cells can prevent a possibly lethal overgrowth by iron oxides. They produce EPS that is used to bind ferric iron, which precipitates on the EPS. Chan et al. (2009) demonstrated that Fe-(III) that is bound to polysaccharides takes days to weeks to precipitate as iron oxide minerals. Polysaccharides can keep the mineralization in a safe distance from the cell. Despite the fact that this mechanism prevents the encrustation of the cell by mineral, the organism can gain further profit by the release of protons that occurs during mineral formation (e. g. Chan et al. 2009 and Chan et al 2004). The EPS allows this process to take place close to the cell but not directly on the cell. In the TEM and SEM analyses performed in this study fibrous structures are present. As these structures appear in chemically and physically fixed samples and in different sample batches, we interpret them as EPS that is secreted by *L. ferrooxidans* EHS-2. Schwertmannite whiskers that are present within this EPS indicate that the mineralization might be taking place within these fibrous structures.

We showed that at 30°C schwertmannite directly and inorganically precipitates from a Fe-(III) and sulfate solution in acidic environment. However, this method is not applicable for a precipitation of larger amounts of schwertmannite.

Crystallographic Structure of Schwertmannite

Most of the literature dealing with schwertmannite assumes that it has the β-FeOOH (akaganeite)-structure as proposed by Bigham (Bigham et al. 1990, Bigham et al. 1994, Cornell & Schwertmann 2003). Our experiments comparing schwertmannites produced by faster and slower mechanisms (30 °C and the slow H_2O_2 synthesis)

show that the precipitation rate does not have a strong influence on the degree of long range order of the material. We conclude that there is a structural element or chemical component present that prevents long range ordering of schwertmannite. In the presence of Cl^- rather than SO_4^{2-} akaganeite crystallizes with long-range order. Hence the tetrahedral sulfate complex is most likely the structural element that prevents long-range order.

The most recent work on which most of our Rietveld-refinements are based uses a modified structure by introducing defects into the β-FeOOH-structure (Fernandez-Martinez et al. 2010). This model was mainly developed from pair distribution function analysis. In our Rietveld refinements it fits the data significantly better than the β-FeOOH-structure. However, the fit is still not perfect. The PDF refinements as they were performed by Fernandez-Martinez et al. (2010) suffer from the same problem as the Rietveld refinements in this study: both are not able to shed light on the position of the sulfate. In our case it turns out that the intensity contribution of one or two sulfur ($Z_S = 16$) atoms per unit cell compared to the strongly scattering iron cage ($Z_{Fe} = 26$) with 16 Fe atoms per unit cell is very low and the very wide diffraction lines prevent any study of such details. In the Rietveld refinements of the present work a linear background model was used to avoid a fitting of peaks by the background function. This approach is limited as we do not take into account the diffuse scattering that occurs due to the nano-crystalline nature of schwertmannite. Still, by refining the Fernandez-Martinez-structure with an anisotropic line broadening model with a needle-like crystallite shape allows stable Rietveld refinements of the structure and an estimate of the crystallite size. The needle axis comes out as being parallel to the channels (b-axis). This is corroborated by the fact that the 040 reflection is the sharp peak at 1.5 Å. A refinement of the other structural models, e. g. the akaganeite structure, do not result in fits of similar quality. The anisotropy of the grain size can be determined with reasonable error (± 0.2 nm). This estimate evidences that schwertmannite shows preferred growth along its channels (b-axis) and that the directions perpendicular to the channels (a- and c- axis) are smaller. In our study the refinements the crystallite dimensions in a- and c- direction are estimated around 2 nm, or about the dimension of two unit cells. In the b-direction the crystallite size is estimated to range from 5 to 11 nm, or $10 - 20$ unit cells. The crystallite size calculated by Fernandez-Martinez et al. (2010) is 3-4 nm depending on their compound in question. As these values do not assume an anisotropic crystallite size they are in reasonable agreement with our results. As Fernandez-Martinez et al. (2010) mention their model (just like ours) does not include relaxations on the grain boundary, an important influence in clusters or particles consisting of only a few unit cells. It is debatable whether or not nanoparticles with complex structures should be described by means of unit cells or better as a complete cluster, a feature that would be accessible by PDF analysis. In the Fernandez-Martinez-model it is disturbing that one of the iron ions is not in octahedral coordination but has one unsaturated bond. As our Mössbauer data shows, there is only Fe-(III) present and there is no indication of other coordination numbers than 6. We suggest that this unsaturated iron is connected with the sulfate tetrahedron that could not be located. This would also give an explanation of

why sulfate prevents long-range ordering: it is too strongly bound to the Fe-O-OH octahedra to be easily stripped off by β-FeOOH crystallization.

Obviously different ways of synthesizing schwertmannite lead to different products regarding their microstructure. Note that the apparent crystallite size calculated by Rietveld refinements is more than one order of magnitude lower as the size of the observed schwertmannite whiskers. Thus the whiskers are aggregates of schwertmannite crystallites. The diffractograms of 85 °C- and dialysed- schwertmannite, materials that were synthesized at elevated temperature, show an additional peak in their diffractograms (d=1.7 Å). The Rietveld refinements show that this peak can be explained by a combination of anisotropic grain sizes and a strain on the lattice.

Magnetic properties

Our Mössbauer results show that there are no signs of Fe-(II) present in schwertmannite and the basic characteristics at 4.2 K and room temperature are comparable to what Bigham et al. (1990 and 1994) described. The magnetic hyperfine field found by Bigham et al. (1990) at 4.2 K is 45.4 T, a value that matches our results of 44.2 T well. At 50 K they report a field of 38.4 T. This does strongly differ from our observations that indicate a field of around 10 T. This discrepancy is due to the fact that the magnetic transition temperatures are different: The transition to a magnetically ordered state appears at an average temperature of 75 K in the Bigham studies (Bigham et al. 1990 and 1994) and in our data it is finished at 65 K and half of the material already transformed at 55 K. Bigham et al. (1990 and 1994) investigated dialyzed-schwertmannite while we used fast-H_2O_2-schwertmannite. Our Rietveld data show that the fast-H_2O_2-schwertmannite has a smaller crystallite size than the dialyzed schwertmannite. It was shown that the transition temperature to magnetically disordered phases in nanocrystalline materials decreases with grain size (Herr et al. 1987), a phenomena that is also known to occur in akaganeite (Rezel and Genin 1990). This discrepancy of transition temperatures due to crystallite size prevents the use of Mössbauer spectroscopy to distinguish between different iron-oxides as it was performed in earlier studies (Eneroth & Bender Koch 2004).

Fitting the observed Mössbauer spectra at low temperatures requires the calculation of two independent hyperfine-fields. This indicates that there are at least two magnetically distinct iron positions present in schwertmannite. Similar observations were made for akaganeite where between two (Murad 1979) and four (Barrero et al. 2006) independent hyperfine-fields have been used to fit Mössbauer spectra.

3.1.5 Concluding Summary

1. Schwertmannite hedgehogs are not overgrown bacteria. The contribution of bacteria such as *Leptospirillum ferrooxidans* EHS-2 to schwertmannite formation seems to be limited to the oxidation of ferrous to ferric iron in acidic conditions. However, EPS that is secreted by the cells might act as a seed or substrate.

2. The calculated XRD pattern of the structural model of schwertmannite proposed by Fernandez-Martinez et al. (2010) is very similar to the observed XRD of our schwertmannite samples. No information of the structural position of sulfate can be gained.

3. Schwertmannite crystallites show an anisotropic, rod-like morphology where the rod axis is parallel to the channels. These crystallites are one order of magnitude smaller than schwertmannite whiskers as they are observed in SEM and TEM.

4. Mössbauer spectroscopy shows that schwertmannite is a pure Fe-(III) compound with six-coordinated Fe-(III) only.

References

Adams, L. K., Harrison, J. M., Lloyd, J. R., Langley, S., Fortin, D. (2007): Activity and Diversity of Fe-(III)-Reducing Bacteria in a 3000-Year-Old Acid Mine Drainage Site Analogue. Geomicrobiology Journal, 24, 295-305.

Barrero, C. A., Garcia, K. E., Morales, A. L., Kodjikian, S., Grenche, J. M. (2006): New analysis of the Mössbauer spectra of akaganeite. Journal of Physics: Condensed Matter, 18, 6827-6840.

Bigham, J. M., Schwertmann, U., Carlson, L., Murad, E. (1990): A poorly crystallized oxygydroxysulfate of iron formed by bacterial oxidation of Fe-(II) in acid mine water. Geochimica et Cosmochimica Acta, 54, 2743-2758.

Bigham, J. M., Carlson, L., Murad, E. (1994): Schwertmannite, a new iron oxyhydroxysulphate from Pyhäsalmi, Finnland, and other localities. Mineralogical Magazine, 58, 641-648.

Bigham, J. M., Schwertmann, U., Traina, S. J., R.L. Winland, Wolf, M. (1996): Schwertmannite and the chemical modeling of iron in acid sulfate waters. Gechimica et Chosmochimica, 60, 211-2121.

Bradley, W.F. (1957): Analysis of Mixed-Layer Clay Mineral Structures. Analytical Chemistry, 25, 727-130.

Burton, E. D., Johnston, S. G., Watling, K., Bush, R. T., Keene, A. F., Sullivan, L. A. (2010): Arsenic Effects and Behaviour in Association with the Fe-(II)-Catalyzed Transformation of Schwertmannite. Environmental Science & Technology, 44, 2016-2021.

Carlson, L., Bigham, J.M., Schwertmann, U., Kyek, A., Wagner, F. (2002): Scavenging of AS from Acid Mine Drainage by Schwertmannite and Ferrihydrite: A Comparison with Synthetic Analogues. Environmental Science and Technology, 36, 1712-1719.

Chan C. S., De Stasio, G., Welch, S. A., Girasole, M., Frazer, B. H., Nesterova, M. V., Fakra, S., Banfield, J. F. (2004): Microbial Polysaccharides Template Assembly of Nanocrystal Fibers. Science, 303, 1656-1658.

Chan C. S., Fakara, S. C., Edwards, D. C. Emerson, D., Banfield, J.F. (2009): Iron oxyhyydroxide mineralization on microbial extracellular polysaccharides. Geochimica et Cosmochimica Acta, 73, 3807-3818.

Cornell, R. M., Schwertmann, U. (2003): The Iron Oxides. WILLEY-VCH, Weinheim, Germany. Second edition. ISBN-3-527-30274-3.

Eneroth, E., Bender Koch, C. (2004): Fe-Hydroxysulphates from Bacterial Fe^{2+} Oxidation. Hyperfine Interactions, 156/157, 423-429.

Eusterhues, K., Wagner, F., Häusler, W. H., Hanzlik, M., Knicker, H., Totsche, K. U., Kögel-Knabner, I., Schwertmann, U. (2008): Characterization of Ferrihydrite-Soil Organic Matter Coprecipitates by X-ray Diffraction and Mössbauer Spectroscopy. Environmental Science and Technology, 42, 7891–7897 .

Fernandez-Martinez, A., Timon, V., Roman-Ross, G., Cuello, G.J., Daniels, J.E., Ayora, C. (2010): The structure of schwertmannite, a nanocrystalline iron oxyhydroxysulfate. American Mineralogist, 95, 1312-1322.

Ferris F. G., Hallbeck, L., Kennedy, C.B., Pedersen, K. (2004): Geochemistry of acidic Rio Tinto headwaters and role of bacteria in solid phase metal partitioning. Chemical Geology, 212, 291-300.

Giagliano, W. B., Brill, M. R., Bigham, J. M., Jonesm F. S., Traina, S. J. (2004): Chemistry and mineralogy of ochreous sediments in a constructed mine drainage wetland. Geochimica et Chosmochimica Acta, 68, 2119-2128.

Hedrich, S., Heinzel, E., Seifert, J., Schlömann, M. (2009) Isolation of novel iron-oxidizing bacteria from an acid mine water treatment plant. Advanced Materials Research, 71-73, 125-128

Herr, U., Jing, R., Birringer, R., Gonser, U., Gleiter, H. (1987): Investigation of nanocrystalline iron materials by Mössbauer spectroscopy. Applied Physics Letters, 50, 472-474.

Hockridge, J. G., Jones, F., Loan, M., Richmond, W. R. (2009): An electron microscopy study of the crystal growth of schwertmannite needles trough oriented aggregation of goethite nanocrystals. Journal of Crystal Growth, 311, 3876-3882.

Johnson, D. B., Hallberg, K. B (2007): Biodiversity of Acidophilic Microorganisms That Have Direct and Secondary Roles in Mineral Dissolution. In: Biomining. Edited by: Rawlings, D. E., Johnson, D. B.; Springer, Germany, ISBN: 3-540-34909-X. Pages 237-262.

Kawano, M. and Tomita, K. (2001) Geochemical modeling of bacterially induced mineralization of schwertmannite and jarosite in sulfuric acid spring water. American Mineralogist, 86, 1156-1165.

Kappler, A, Schink, B, Newman, DK (2005): Fe-(III) mineral formation and cell encrustation by the nitrate-dependent Fe-(II)-oxidizer strain BoFeN1. Geobiology, 3, 235-245.

Kupka, D., Rzhepishevska, O. I., Doposon, M., Lindström, E. B., Karnachuk, O. V., Tuovinen, O. H. (2007): Bacterial oxidation of ferrous iron at low temperatures. Biotechnology and bioengineering, 97, 1470-1478.

Larson, A.C., Von Dreele, R.B. (2004): Gerneral Structure Analysis System (GSAS). Los Alamos National Laboratory Report LAUR, 86-748.

Loan, M., Cowley, J. M., Hart, R., Parkinson, G. M. (2004): Evidence on the structure of synthetic schwertmannite. American Mineralogist, 89, 1735-1742.

Loan, M., Richmond, W.R., Parkinson, G. M. (2005): On the crystal growth of nanoscale schwertmannite. Journal of Crystal Growth, 275, e1875-e1881.

Majzlan, J. and Myneni, S. C. B. (2005): Speciation of Iron and Sulfate in Acid Waters; Aqueous Clusters to Mineral Precipitates. Environmental Science and Technology, 39, 188-194.

Manceau, A. (2009): Evaluation of the structural model for ferrihydrite derived from real-space modeling of high-energy X-ray diffraction data. Clay Minerals, 44, 19-34.

Mikutta, C., Mikutta, R., Bonneville, S., Wagner, F., Voegelin, A., Christl, I., Kretzschmar, R. (2008): Synthetic coprecipitates of exopolysaccharides and ferrihydrite. Part I: Characterization. Geochimica et Cosmochimica Acta, 72, 1111-1127.

Murad, E. (1979): Moessbauer and X-ray data on beta -FeOOH (akaganeite). Clay Minerals, 14, 273-283 .

Parafiniuk, J., Siuda, R. (2006): Schwertmannite precipitated from acid mine drainage in the Western Sudetes (SW Poland) and its arsenate sorption capacity. Geological Quaterly, 50, 475-486.

Post, J.E., Buchwald, V.F. (1991): Crystal structure refinement of akaganeite. American Mineralogist, 76, 272-277.

Regenspurg, S., Brand, A., Pfeiffer, S. (2004): Formation and Stability of schwertmannite in acidic mining lakes. Geochimica et Cosmochimica Acta, 68, 1185-1197.

Regenspurg, S., Peiffer, S. (2005): Arsenate and chromate incorporation in schwertmannite. Applied Geochemistry, 20, 1226-1339.

Rezel, D., Genin, J.M.R. (1990): The substitution of chloride ions to OH–Ions in the akaganeite beta ferric oxyhydroxide studied by Mössbauer effect. Hyperfine Interactions, 57, 2067-5076.

Schädler, S., Burkhardt, C., Hegler, F., Straub, K.L., Miot, J., Benzerara, K., Kappler, A. (2009): Formation of Cell-Iron-Mineral Aggregates by Phototrophic and Nitrate-Reducing Anaerobic Fe-(II)-Oxidizing Bacteria. Geomicrobiology Journal, 26, 93-103.

Toby, B.H. (2001): EXPGUI, a graphical user interface for GSAS. Journal of Applied Crystallography, 34, 210-213.

Walter, P. and Ziegler, A. (2002): Freeze substitution of high-pressure frozen samples: the visibility of biological membranes is improved when the substitution medium contains water. Journal of Microscopy, 208, 3-10.

Waychunas, G.A., Xu, N., Fuller, C. C., Davis, J. A., Davis, J. A., Bigham, J. M. (1995): XAS study of AsO43- and SeO42- substituted schwertmannites. Physica B, 208&209, 481-483.

Webster, J. G., Swedlund, P. J., Webster, K. S. (1998): Trace Metal Adsorption onto an Acid Mine Drainage Iron(III) Oxy Hydroxy Sulfate. Environmental Science and Technology, 32, 1361-1368.

Supplementary Material

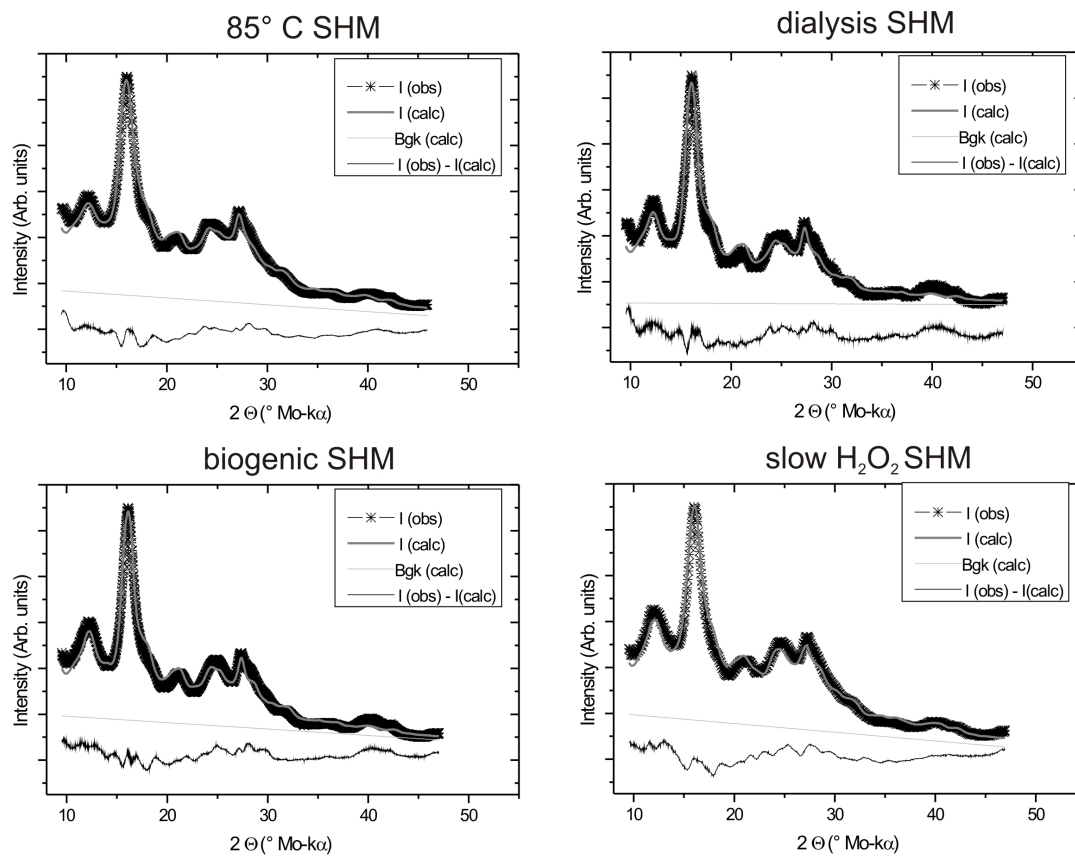The following Figure 3.8 and Table 3.4 were submitted as supplementary material.

Figure 3.8: Diffractograms and result of Rietveld refinements of schwertmannites precipitated by different ways.

Table 3.4: Results from the fitting of Mössbauerdata recorded at the fast-H_2O_2-schwertmannite.

T (K)	B_{eff} (T)	A_mag	A_tot	IS-Mean	Fited with	$\chi 2$
4.2	44.18	1	0.29	0.25	3*sextet	5.554
16	42.92	1	0.285	0.25	2*sextet	1.227
17.5	41.78	1	0.284	0.25	2*sextet	1.225
19.25	40.87	1	0.2945	0.25	2*sextet	1.069
21	39.93	1	0.293	0.24	2*sextet	1.263
23	38.76	1	0.303	0.24	2*sextet	1.247
25	37.75	1	0.305	0.24	2*sextet	1.138
27	36.41	1	0.305	0.24	2*sextet	1.004
29	35.58	1	0.295	0.24	2*sextet	0.966
31	35.28	1	0.286	0.25	2*sextet	0.96
33	33.86	1	0.315	0.24	2*sextet	0.96
35	32.8	1	0.294	0.24	2*sextet	0.929
37	31.65	0.99	0.315	0.24	1*doublet, 2*sextet	1.033
39	29.93	0.99	0.304	0.25	1*doublet, 2*sextet	1.164
41	26.66	0.97	0.289	0.23	1*doublet, 2*sextet	1.084
43	23.65	0.97	0.29	0.24	1*doublet, 2*sextet	1.115
44	23.35	0.97	0.283	0.23	1*doublet, 2*sextet	1.031
45	20.55	0.945	0.268	0.23	1*doublet, 2*sextet	1.015
47	17.31	0.925	0.261	0.22	1*doublet, 2*sextet	1.034
47.5	16.77	0.938	0.26	0.23	1*doublet, 2*sextet	0.913
49	14.48	0.905	0.263	0.24	1*doublet, 2*sextet	0.942
50.5	8.64	0.726	0.242	0.23	1*doublet, 1*sextet	0.959
51	9.71	0.862	0.271	0.29	1*doublet, 2*sextet	0.998
53	6.15	0.795	0.256	0.27	1*doublet, 2*sextet	1
53	2.7	0.548	0.245	0.27	1*doublet, 1*sextet	1.057
55	2.5	0.542	0.231	0.25	1*doublet, 1*sextet	1.546
55	2	0.503	0.235	0.25	1*doublet, 1*sextet	0.923
56.5	2	0.453	0.235	0.24	1*doublet, 1*sextet	1.087
64.5	0	0	0.221	0.25	1*doublet	1.855
298	0	0	0.1212	0.26	1*doublet	6.45

3.2 Calcite morphology, texture and hardness in the distinct layers of rhynchonelliform brachiopod shells

Calcite morphology, texture and hardness in the distinct layers of rhynchonelliform brachiopod shells

Andreas J. GOETZ[1], Erika GRIESSHABER[1,*], Rolf D. NEUSER[2], Carsten LÜTER[3], Manfred HÜHNER[4], Elisabeth HARPER[5] and Wolfgang W. SCHMAHL[1]

[1] Department für Geo- und Umweltwissenschaften, Ludwig-Maximilians-Universität München, München, Germany
*Corresponding author, e-mail: E.Griesshaber@lrz.uni-muenchen.de
[2] Institut für Geologie, Mineralogie und Geophysik, Ruhr-Universität Bochum, Bochum, Germany
[3] Museum für Naturkunde der Humboldt-Universität zu Berlin, Berlin, Germany
[4] Institut für Werkstoffe, Werkstoffwissenschaft, Ruhr-Universität-Bochum, Bochum, Germany
[5] Department of Earth Sciences, University of Cambridge, Cambridge, U.K.

Abstract: We have investigated the texture and shell microstructure together with the individual hardness distribution patterns of recent calcitic brachiopods of the species *Kakanuiella chathamensis, Liothyrella uva* and *Liothyrella neozelanica*. One of the most distinctive features of the studied species is the number of layers that compose the shell. *Kakanuiella chathamensis* is built entirely of nano- to microcrystalline primary layer calcite. *Liothyrella uva* contains a nanocrystalline outer primary layer and an inner fibrous secondary layer. *Liothyrella neozelanica* is composed of three layers, a nanocrystalline outer primary layer, a columnar secondary and an innermost fibrous tertiary shell layer. Even though *Kakanuiella chathamensis* consists only of primary layer material we observe some textural features and a pattern in the distribution of hardness within the shell. The texture of *Liothyrella uva* and of *Liothyrella neozelanica* is significantly more defined than that of *Kakanuiella chathamensis*. Within the valves calcite crystal *c*-axes are perpendicular to and rotate accordingly with the shell vault. In contrast to the valves, a multimodal *c*-axis distribution pattern is present within the hinge region. The hardness distribution in *Liothyrella neozelanica* and *Liothyrella uva* is such that the outermost part of the shell is hard while the innermost shell portion is soft. In general, *Liothyrella uva* is significantly harder than *Liothyrella neozelanica* and *Kakanuiella chathamensis*, even though *Kakanuiella chathamensis* contains only primary layer calcite.

Key-words: SEM, EBSD, microstructure, ultrastructure, texture, nanocomposite, biomineralization, nacre, Vickers hardness.

This peer-reviewed article is published in:

3.3 Interdigitating Biocalcite Dendrites form a 3D-Jigsaw-Structure in Brachiopod Shells

Interdigitating biocalcite dendrites form a 3-D jigsaw structure in brachiopod shells

Andreas J. Goetz [a,*], David R. Steinmetz [b], Erika Griesshaber [a], Stefan Zaefferer [b], Dierk Raabe [b], Klemens Kelm [c], Stephan Irsen [d], Angelika Sehrbrock [d], Wolfgang W. Schmahl [a]

[a] Department für Geo-und Umweltwissenschaften, LMU, Theresienstr. 41, D-80333 München, Germany
[b] Max-Planck-Institut für Eisenforschung, Max-Planck-Straße 1, D-40237 Düsseldorf, Germany
[c] German Aerospace Center (DLR), Institute for Materials Research, Linder Höhe, D-51147 Köln, Germany
[d] Forschungszentrum CAESAR, Ludwig-Erhard-Alle 2, D-53175 Bonn, Germany

ARTICLE INFO

ABSTRACT

We report a newly discovered dense microstructure of dendrite-like biocalcite that is formed by marine organisms. High spatial resolution electron backscatter diffraction (EBSD) was carried out under specific analytical conditions (15 and 10 kV) on the primary layer of the modern brachiopod *Gryphus vitreus*. The primary layer of modern brachiopods, previously termed nanocrystalline, is formed by an array of concave/convex calcite grains with interdigitated recesses and protrusions of abutting crystals without any cavities in or between the dendrites. The interface topology of this structure ranges from a few tens of nanometres to tens of micrometres, giving a nanoscale structure to the material fabric. The dendritic grains show a spread of crystallographic orientation of several degrees and can thus be referred to as mesocrystals. Individual dendritic mesocrystals reach sizes in one dimension larger than 20 μm. The preferred crystallographic orientation is similar in the primary and adjacent fibrous shell layers, even though these two layers show completely different crystal morphologies and grain boundary topologies. This observation indicates that two separate control mechanisms are active when the primary and the fibrous shell layers are formed. We propose a growth model for the interdigitated dendritic calcite grain structure based on a precursor of vesicles filled with amorphous calcium carbonate (ACC).

This peer-reviewed article is published in:

3.4 An Easy Approach to Increase the Precision of EBSD Analysis – Examples from a Sea Urchin Calcite Study

An Easy Approach to Increase the Precision of EBSD Analysis – Examples from a Sea Urchin Calcite Study

A. Goetz[1, a], E. Griesshaber[1,b] and W. W. Schmahl[1,c]

[1] Department für Geo- und Umweltwissenschaften, Ludwig-Maximilians-Universität München, München, Germany

[a]andreas.goetz@lrz.uni-muenchen.de, [b] e.griesshaber@lrz.uni-muenchen.de, [c]wolfgang.schmahl@lrz.uni-muenchen.de

Keywords: EBSD, high angular resolution, calcite, biomineralization, sea urchin spine

Abstract. Sea urchins mineralize Mg-calcite skeletons, both, within their exoskeletons as well as in their spines. In this study we have investigated sea urchin spines of the species *Amblypneustes pachistus*. The spines are round and consist of several wedges that extend from the base to the tip of the spine. The wedges are connected to each other by porous calcite. Rocking curves of the spines show a distribution of 0.5° of the 110 reflection, with the domains being misoriented by 0.1° to each other. In our EBSD system the average mean angular (MAD) deviation is 0.3°. This is higher than the signal that is needed for the detection of small misorientations of domains within a sea urcin spine.

In order to increase the precision (not the accuracy) of the EBSD measurements several factors, such as geometric artifacts and charging of calcite were minimized. Handling of these factors and utilizing the subsequently described statistical approach allowed for the identification of different domains within the spines. It further allowed calculating the degree of misorientation between these domains. Our EBSD analyses and the subsequent evaluation of the data show that the wedges forming the spines of *Amblypneustes pachistus* are mosaic crystals. The misorientation of the wedges to each other increases from the base of the spine towards its tip.

The here proposed method for increasing the precision of the angular resolution showed reproducibility on silicon of 0.05°.

This peer-reviewed article is published in:

Solid State Phenomena, 2010, 160, 229-234
TITLE: An Easy Approach to Increase the Precision of EBSD Analysis – Examples from a Sea Urchin Calcite Study
AUTHORS: Andreas Goetz, Erika Griesshaber and Wolfgang W. Schmahl.

3.5 Are sea urchin spines really perfect single crystals?

This section is a manuscript in preparation that will be submitted to:

3.5.1 Introduction

Sea urchins are marine animals that live on the sea floor. They consist of a spherically shaped, calcitc exoskeleton onto that calcitic spines are attached in a radial arrangement (e.g. Märkel & Röser 1983). The spines are porous (Smith 1980; Su et al. 2000) and occur in a wide range of sizes and shapes. On the basis of diffraction experiments sea urchin spines have been regarded as perfect single crystals (Currey & Nichols 1967, Donnay & Pawson 1969, Magdans & Gies 2004, Paquette & Reeder 1990, Schmidt 1930, Su et al. 2000). Thus, each spine is considered to be a large single crystal where the central axis of the spine corresponds with the crystallographic c-axis of the calcite crystal. However, the single crystal nature of sea urchin spines is currently under debate, they are also regarded as highly ordered aggregates of polycrystals (Oneill 1981, Tsipursky & Buseck 1993) or as mesocrystals (Meldrum & Cölfen 2008). One indication for the mesocrystalline nature of sea urchin spines was given by Aizenberg and co-workers (Aizenberg et al. 1997), who showed with synchrotron radiation experiments that, depending on the crystallographic orientation, the coherence length of sea urchin spine calcite is 100 - 250 nm compared to 250 - 500 nm for non-biological, inorganically precipitated calcite.

In this study we investigated the spines of the sea urchin *Holopneustes porosissimus*. This sea urchin species lives in shallow water environments and is entirely surrounded by kelp that tightly covers the animal. Thus *Holopneustes porosissimus* has developed small spines (<5 mm length) since these are best suited for this specific habitat. The spines of *Holopneustes porosissimus* can be divided into a base (the connection between spine and the body of the animal, the corona) and a shaft portion. The shaft consists of several septa or wedges that are built of massive calcite. In the spine the wedges are aligned to each other in a concentric manner. They form about 2/3 of the radius of the spine and get thicker towards the outer rim of the spine. Each wedge spreads over the entire length of the complete shaft. The wedges are separated from each other by a highly porous calcite. This porous calcite is also present in the center of the spine.

Even though the wedges and the porous calcite between the wedges and in the center of the spine have distinct microstructures, sea urchin spines exhibit a highly ordered or even perfect calcite crystal orientation. The major aim of this study is the investigation of the degree of calcite crystal ordering within the wedges, the porous calcite within the wedges and finally within the entire spine. For this purpose we have investigated on several scale levels (macro,- micro, and nanoscale) the microstructure and the texture of the spine forming components in addition to a possible chemical and mechanical structuring within the spines.

3.5.2 Samples and Methods

Samples

We analyzed spines of *Holopneustes porosissimus*, obtained from the Zoologische Staatssammlung München (Reg. Nr. 20060657). 10 spines were investigated from one individual. 3 spine samples were analyzed with EBSD, 4 spine samples with

EPMA and 3 spine samples with nanoindentation testing, respectively. We have investigated both, parallel and perpendicular, sections to the longitudinal axis of the spines. All spine samples were fixed to a glass slide and were subsequently ground down to thickness of 300 - 400 μm. Sample surface was highly polished and was finished with the use of diamond paste containing 10 μm sized diamonds. Sample preparation for EBSD analysis comprised additional polishing of the sample surface, a subsequent etching of the surface with OP-A solution for 45 minutes and subsequent coating with a 5 - 10 nm layer of carbon. For microprobe analyses the samples were also further polished. Polishing was finished with the use of a diamond paste containing 0.25 μm sized diamonds. For EPMA samples were coated with 15 nm of carbon. Microprobe results obtained on the spines were compared to two non-biological calcite references: a transparent calcite single crystal from Rodeo, Durango, Mexico and an opaque calcite single crystal of calcite from India. For TEM sample preparation a portion of the spine was clipped in a grooved titanium ring. The 4000 μm thick portion of the spine was ground from both sides to a thickness of 1000 μm, dimpled from both sides to 500 μm thickness and finally ion-etched on both sides at 4 kV with argon ions.

Methods

SEM
The EBSD analyses were conducted in a field emission gun SEM (JEOL JSM 6500 F) with an accelerating voltage of 20 kV under a tilt angle of 70°. Kikuchi patterns were recorded with a NORDLYS detector and were indexed with the CHANNEL 5 software package. Average MAD (mean angular deviation) during EBSD measurement was 0.3°, measurements above 0.5° were discarded.

TEM
The TEM analyses were carried out on a Philips Tecnai F30 STEM electron microscope equipped with EDAX EDX and Gatan EEL spectroscopy systems. Accelerating voltage was 300 kV.

Conventional EBSD and high angular resolution EBSD
For the high precision EBSD measurements a statistical attempt was used. For this several small maps (10*10 pixels, 1.5 μm step size) were measured. After finishing one map the stage was moved parallel to the tilt axis by 15 μm and a new map was measured, all conditions including the focus were kept constant. This procedure only allows measurements parallel to the tilt axis and is very sensitive to non-perfect sample surface leading to less precession.

The obtained data sets were evaluated with the computer algebra program MATHEMATICA. As a first step an estimate of the average orientation of the complete data set was calculated, using all indexed points with a MAD lower than 0.5°. To avoid the mathematically non-trivial normalization of the orientation matrix, the average orientation of the a- and c-axes was calculated independently of each other. The analysis point closest to the average orientation of both axes, was then defined as the average orientation. The error induced is usually two orders of magnitudes

lower than the resulting angular resolution. After the definition of the estimated average orientation, "wild spikes", wrong indexations that can occur during measurements, were removed by discarding all points that were not within three times the standard deviation of the average orientation. The rest of the dataset (usually more than 95%) was then used to determine again the average orientation of the entire data set. The average orientation, obtained as described above, of the data sets was compared and small differences in orientation (around 0.1°) could be differentiated.

This attempt is based on the fact, that the analyses have a stochastic distribution of the orientation. In the Appendix (Figure 3.15) is demonstrated that this is the case. The applied method is described in greater detail elsewhere (Goetz et al. 2010).

XRD

Rocking curves of complete sea urchin spines were obtained on a Stoe powder diffractometer using Mo-kα_1 radiation. We performed omega scans of the 110 - reflection of the sea urchin spines. To protect the detector from strong reflections it was covered by several layers of aluminium foil. An omega step size of 0.01° was used.

Rocking curves of single wedges were obtained with synchrotron radiation at the SUL-X beamline (ANKA Karlsruhe) with a wavelength of 0.72 Å and a spot size of $50 \, \mu m$. Rocking curves were obtained in reflection with a CCD Camera equipped with a Kodak Chip on a 2-theta position of 110°. The used omega step size was 0.025°.

EPMA

Quantitative chemical data was obtained by electron microprobe analysis (EMPA) using a CAMECA SX100 operated at 15 kV acceleration voltage and 20 nA beam current with a measurement time of 60 ms per point. Synthetic wollastonite (Ca, Si), periclase (Mg), hematite (Fe), albite (Na) and orthoclase (K) were used as standards for the elements mentioned in brackets. Matrix correction was performed by the PAP procedure (Pouchou and Pichoir 1984). The reproducibility of standard analyses was <1% and for each element routinely analysed. The PAP corrected data were stoechiometrically calculated as carbonate.

Nanoindentation

Nanoindentation measurements were performed with an MTS nanoindenter (SA2) equipped with a contact stiffness measurement (CSM) indenter-head allowing a depth depending measurement. The measurements were performed with a Berkovich indenter tip to an indentation depth of 300 nm and a CSM frequency of 45 Hz. Only the data from 100 - 300 nm depth was used for calculating the hardness, as the first 100 nm did not yet converge to the true hardness values. The strain frequency was set to 0.2 Hz. An isotropic Poisson ratio of 0.3 was assumed for the investigated biological material. For the calculation of average hardness and average modulus values invalid indents due to breaking of the indenter into micropores had to be removed. Therefore investigations of the indents and their positions were performed by re-

flected light microscopy and coupled to histogram analyses of the nanoindentation data. It turned out, that a minimum value of 3 GPa (indicated in the nanohardness figures by a red line) for hardness chosen to exclude invalid indents due to breaks resulting from the microposity of the spine from the dataset. There are practically no indents present with hardnesses between 2.5 GPa and 3 GPa. Only indents with hardness higher than 3 GPa were included in the calculation of the average hardness and Young's modulus.

3.5.3 Results

Spine micro- and nanostructure

The spines of sea urchin *Holopneustes porosissimus* consist of massive calcitic wedges that are connected to each other by porous calcite (Figure 3.9). Pore sizes are between 5-10 μm, the wedges are connected to each other by also 5-10 μm thick calcite bridges. The length of one wedge is as large as 2/3 of the radius of the spine, the inner third of the spine is filled by the same porous material that connects the wedges (Figure 3.9b). A single wedge spreads from base to top of the spine. Note that the wedges together with the porous calcite reflect in diffraction experiments as one single crystal. However, in fracture surfaces the calcite 104 - cleavage plane is completely missing. The surface exhibits an agglomeration of small particles (Figure 3.9e - h), 20-30 nm in size.

The etching applied in the course of EBSD sample preparation resulted in a patterned structure that shows very homogeneous growth marks. These growth marks have dimensions of some hundred nanometres and lead concentrically away from the centre of the spine (Figure 3.9c). In the porous stereom (the center of the spine) we find, concentric micro-growth lines around several seed locations (micro spines, Figure 3.9d). At points where the concentric lines would interfere they join and further micro growth lines are a superposition of the two former lines.

TEM analyses on the spines of *Holopneustes porosissimus* reveal that the porosity of the spines is not only on the micrometer scale (as clearly visible in SEM imaging) but also on the nanometer scale (Figure 3.10). TEM imaging reveals pores in the size down to 3 nm. The contrast within the pores indicates that we see a section through a spherically shaped pore (Figure 3.10b). They have usually an elongated shape with an aspect ratio average of 1.9 (+/-0.9, Figure 3.10). All observed pores with an elongation occur perpendicular to the longitudinal axis of the spine. The length of the grains is between 3 - 400 nm whereas pores with lengths of 20 nm, 100 nm, 150 nm, 220 nm and 280 nm (Figure 3.10) are very abundant. Occasionally, we observe spine portions, where pores are not present, even not on a nm scale. The thickness of these portions is about 1 μm.

Spine mesocrystallinity

EBSD measurements were performed on transverse and longitudinal sections of the spines. The above described procedure allowing us to find that the wedges within one spine are tilted within 0.6° towards each other (Figure 3.11 and Table 3.5-3.7).
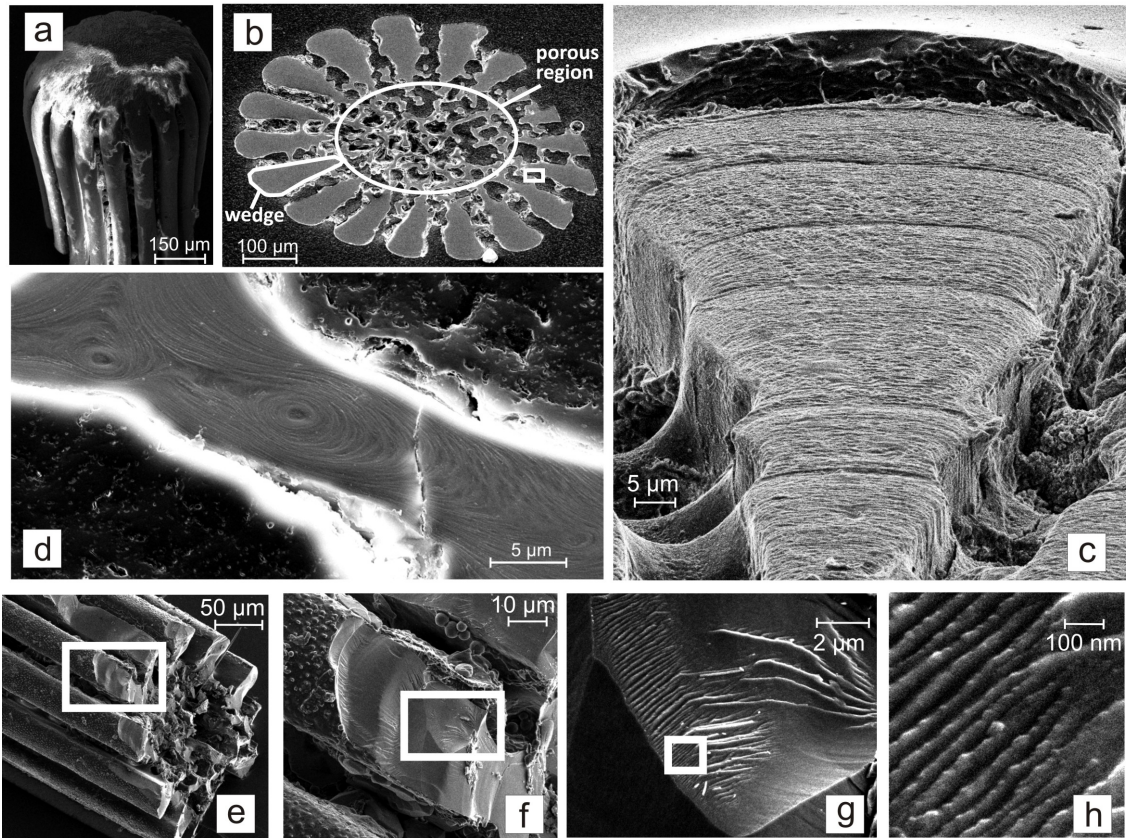
Figure 3.9: SEM images of sea urchin spines. a) represents the tip of the spine. b) is a transversal section the spine, tilted by 23°. Like all spines of *Holopneustes porosissimus*, the outer part of the spine consists of wedges, while the central spine portion is built of porous calcite. c) is the magnification of a transversal spine section that was etched for a longer time. Micro growth lines are not concentric. Growth of the spine is only taking place in the outer portion of the spine, leading to its thickening. d) represents a magnification of the white rectangle shown in Figure 3.9b. The growth lines indicate, that the porous parts of the spine are growing concentrically around nucleation zones. In the case where two distinct growth lines join they form a common line that is a superposition of both growth lines. Figures e - h show a magnification series of fracture surfaces of the spine. The fracture of sea urchin spines is unlike to non-biological calcite fracture and resembles fracture in a glassy material. The highest magnification of the fragments show, that the spine consist of an aggregation of small particles, 20-30 nm in size.

Figure 3.10: a) and b) TEM (HAADF) images of different magnifications of the pores present in sea urchin spines. The clear preferred orientation of the pores is well visible. As visible in Figure 3.10b, the contrast in some pores is not constant (indicated by black arrows), it is darker in their center and indicates that the pore i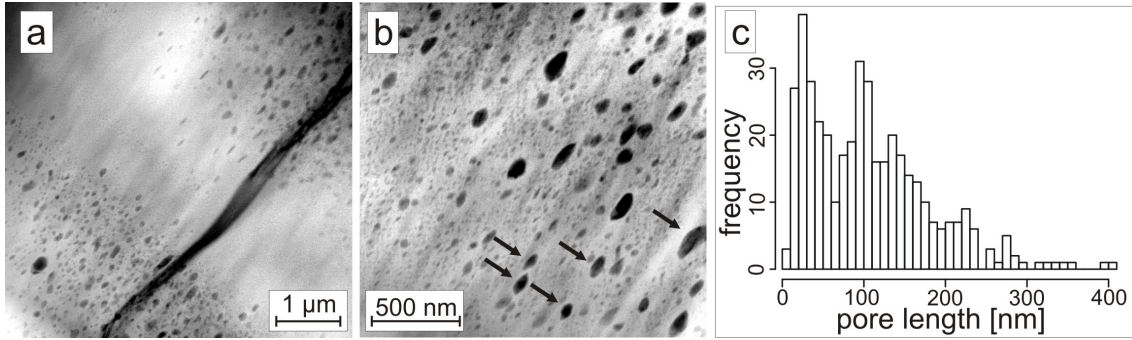s not cylindrical but is a double section through a sphere. c) shows in a histogram the distribution pattern of pore length within a representative portion of the spine.

Table 3.5: Misorientation between the EBSD maps measured along a profile on the longitudinal cut (Figure 3.11a, profile 1) of a sea urchin spine. Maps 1 to 4 are located on wedge 1, maps 5 & 6 are located on wedge 2 and maps 7 - 9 are located on wedge 3.

	Map 1	Map 2	Map 3	Map 4	Map 5	Map 6	Map 7	Map 8	Map 9
Map 1	0.00	0.06	0.05	0.09	0.45	0.53	0.38	0.34	0.34
Map 2	0.06	0.00	0.06	0.04	0.50	0.58	0.42	0.39	0.39
Map 3	0.05	0.06	0.00	0.1	0.46	0.53	0.41	0.36	0.36
Map 4	0.09	0.04	0.10	0.00	0.54	0.61	0.44	0.42	0.42
Map 5	0.45	0.5	0.46	0.54	0.00	0.12	0.25	0.14	0.14
Map 6	0.53	0.58	0.53	0.61	0.12	0.00	0.36	0.24	0.24
Map 7	0.38	0.42	0.41	0.44	0.25	0.36	0.00	0.14	0.14
Map 8	0.34	0.39	0.36	0.42	0.14	0.24	0.14	0.00	0.00
Map 9	0.34	0.39	0.36	0.42	0.14	0.24	0.14	0.00	0.00

Table 3.6: Average misorientation between the wedges of profile 2 (Figure 3.11b).

	wedge 1	wedge 2	wedge 3	wedge 4	wedge 5	wedge 6	wedge 7
wedge 1	0.03	0.25	0.31	0.27	0.20	0.14	0.37
wedge 2	0.25	0.06	0.13	0.20	0.20	0.11	0.17
wedge 3	0.31	0.13	n/a	0.16	0.17	0.19	0.09
wedge 4	0.27	0.20	0.16	n/a	0.13	0.18	0.18
wedge 5	0.2	0.20	0.17	0.13	n/a	0.16	0.23
wedge 6	0.14	0.11	0.19	0.18	0.16	n/a	0.24
wedge 7	0.37	0.17	0.09	0.18	0.26	0.24	0.04
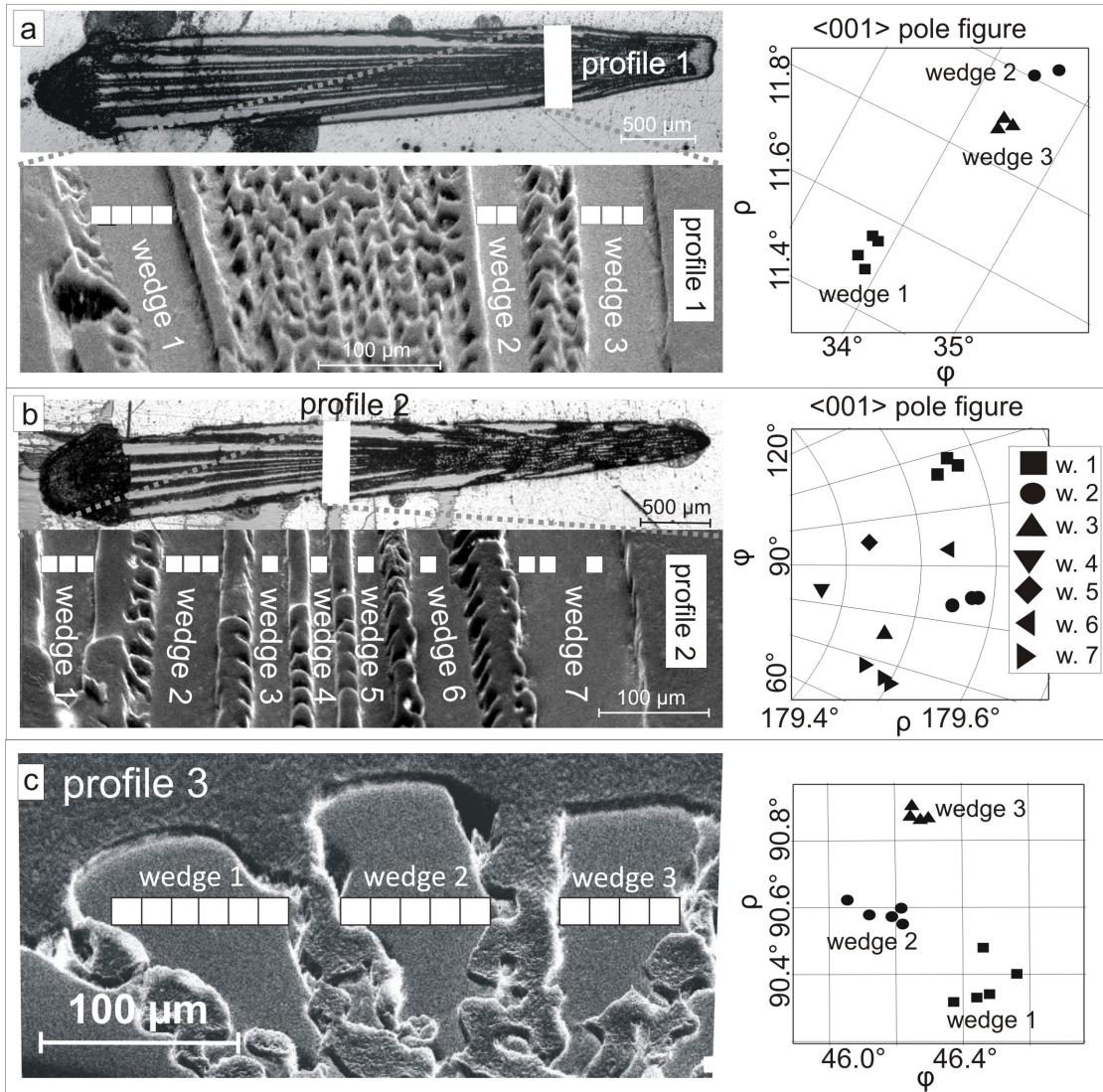
Figure 3.11: EBSD profiles measured on different wedges. SEM images give a magnification of the investigated spine/wedge portions. The white boxes in the SEM micrographs indicate the specific portion where EBSD maps are located. On the left hand side of the SEM images selected areas of pole figures (see Fig. 1 for definition of the angles) show the c-axes orientation of the different wedges. Figures a) and b) show EBSD profiles on a longitudinal spine section. Figure c) gives EBSD profiles on a transversal spine section. Regardless of the mode of sectioning, the EBSD data demonstrate well the tilt of individual wedges to each other (see also Table 3.5).

Table 3.7: Average misorientation between the wedges of profile 3 (Figure 3.11c). The standard deviation is below 0.1° for all values.

	wedge 1	wedge 2	wedge 3
wedge 1	0.07°	0.33°	0.56°
wedge 2	0.33°	0.06°	0.30°
wedge 3	0.56°	0.30°	0.03°

Profile 1 (Figure 3.11a) was measured close to the tip of a longitudinal section from the spine. The misorientation between every measured map is given in Table 1. The EBSD maps on one particular wedge show a misorientation below 0.1° towards each other. The comparison of EBSD maps from different wedges shows misorientations to each other of up to 0.5°. The most pronounced misorientation between two wedges is between wedge 1 and wedge 2 (about 0.5°) - two neighbouring wedges. Profile 2 (Figure 3.11b) investigated a larger number of wedges closer to the base of the spine. The observed misorientation between the wedges (Table 3.6) is with a maximum of 0.4° slightly smaller than that observed in profile 1.

On a perpendicular cut through the spine three neighbouring wedges were analyzed with EBSD (Figure 3.11c). The EBSD data is in good agreement with the data sets obtained from longitudinally cut samples: a maximum of 0.55° misorientation can be observed between neighbouring wedges (Table 3.7).

Rocking curves (omega scans) of complete spines of the 110-reflection were measured on different parts of a sea urchin spines. They showed that the single crystal spine consists of different mosaic domains that have a maximum misorientation of 0.5°. The domains are misoriented to each other by about 0.1°(Figure 3.12). The XRD data indicates, that the mosaicity is getting more pronounced towards the tip of the spine. sorientation of 0.5°. The domains are misoriented to each other by about 0.1°(Figure 3.12). The XRD data indicates, that the mosaicity is getting more pronounced towards the tip of the spine.

Additional rocking curves were obtained at higher spatial resolution with synchrotron radiation. Omega scans of the (-7 11 12) and the (-9 9 12) reflection were obtained on 17 wedges of a spine and on the porous center. For the (-7 11 12) reflection the wedges are tilted to each other by 0.05° to 0.45° and towards the porous center of the spine, for the (-9 9 12) reflection, between -0.025° and 0.4° (Table 3.8).

Compositional variations

Energy dispersive scans of the spines show that oxygen, carbon, calcium, magnesium and sodium are well detectable by EPMA. Ca concentration varies between 30 and 40 wt-% and has an average of 33.8 wt-% ($\pm$ 2 wt-%), Mg between 0 to 1.2 wt-% with an average of 0.8 wt-% ($\pm$ 0.3 wt-%) resulting in a molar $MgCO_3$ / $CaCO_3$ ratio of 3.9%. Na content varies between 0 and 1 wt-% with an average of 0.5 wt-% ($\pm$0.25 wt-%, Figure 3.13, Table 3.9). Measurements on the spines were only performed on the wedges, as the porous spine regions are too small to be analyzed precisely.
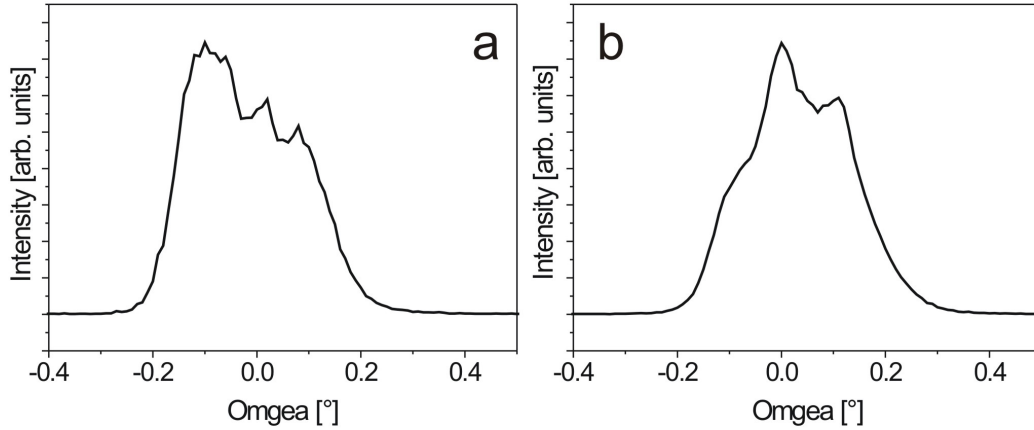
Figure 3.12: 110 rocking curves (omega scans) of the sea urchin spine shown in Figures 3.11a and 3.11b. The range of misorientation of the domains in the spine is around 0.5 degrees. Domains that are tilted by 0.1° can easily be distinguished from each other. Figure 3.12a shows the rocking curve that has been measured close to the tip of the spine, while Figure 3.12b gives an example of a rocking curve which has been analyzed close to the base of the spine. The mosaicity increases towards the tip of the spine.

Table 3.8: Omega values of the maxima of the rocking curves obtained from the spine center. Wedges 1 and 17 are neighbours. Wedge 12 and 14 show the highest misorientation.

	spine center	wedge 1	wedge 2	wedge 3	wedge 4	wedge 5	wedge 6	wedge 7	wedge 8
(-7 11 12)	0.00°	0.30°	0.23°	0.13°	0.05°	0.20°	0.10°	0.20°	0.08°
(-9 9 12)	0.00°	0.25°	0.15°	0.03°	0.00°	0.15°	0.05°	0.15°	0.05°

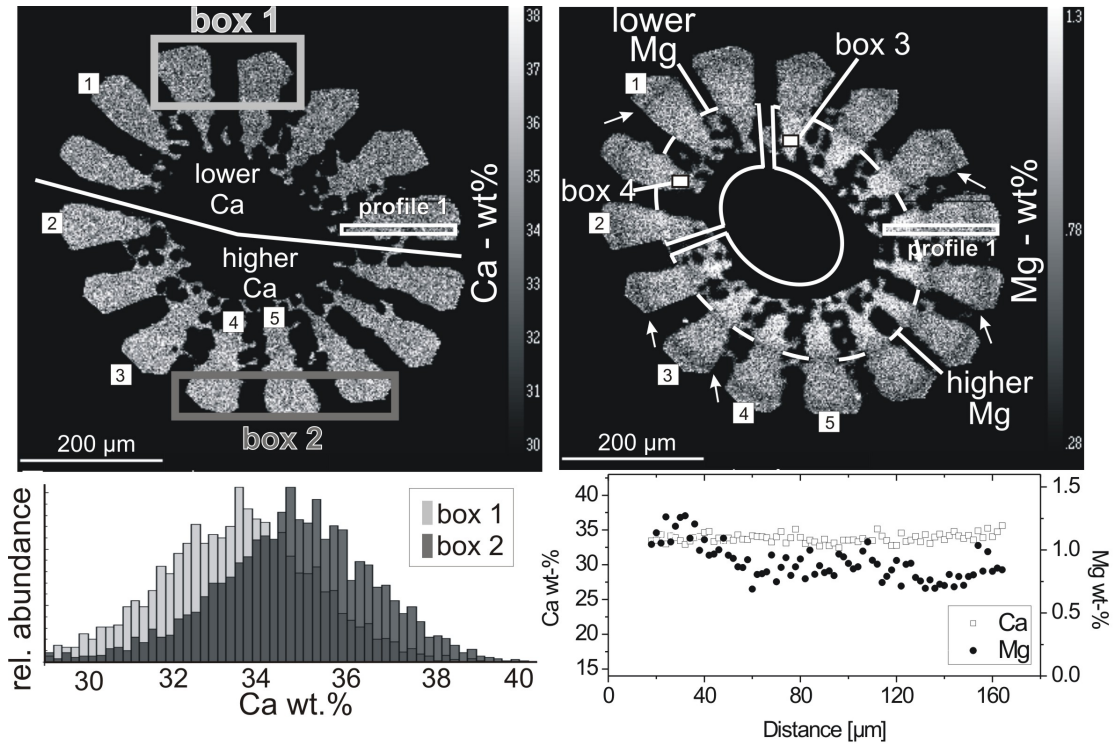|	wedge 9	wedge 10	wedge 11	wedge 12	wedge 13	wedge 14	wedge 15	wedge 16	wedge 17
(-7 11 12)	0.10°	0.25°	0.20°	0.28°	0.38°	0.45°	0.30°	0.30°	0.25°
(-9 9 12)	0.08°	0.18°	0.15°	0.23°	0.33°	0.40°	0.28°	0.15°	0.08°

Figure 3.13: EPMA results from a transversally cut spine sample. The chemical composition of the boxes and profiles shown in the upper two images is given in Table 3.9. This specific sample is also used for nanoindentation testing, the numbers on the upper images indicate the wedges that were investigated by nanoindentation (Figure 3.14). The spine can be subdivided in a region with a higher Ca content and one with a lower Ca content. Despite data scatter the histograms of a lower Ca content (box 1) and that of a higher Ca content (box 2) differ from each other due to the difference in nanoporosity. There is no structuring in Ca contents within wedges. The Mg content of the spine is not correlated to the Ca content. The outer part of the wedges contains less Mg in comparison to its inner part. The distribution pattern of an increase in Mg within the inner portion of the spine is not even. Arrows indicate a ring of Mg depletion. The difference between the homogeneous Ca content and the decreasing Mg content can be found in the lower left graph, a concentration - distance diagram of profile 1.

Table 3.9: EPMA results of the investigated spine compared to the non-biologic calcite references. Note the low total sum of elements for the investigated spine.

	Ca [wt-%]	Mg [wt-%]	Na [wt-%]	CO$_3$ [wt-%] (calculated)	Mg/Ca molar ratio	Sum [wt-%]
All Spine	33.8 ± 2	0.8 ± 0.3	0.5 ± 0.2	55.3	3.89%	90.4
Box 1	33.4 ±1	0.8 ±0.2	0.5 ±0.2	54.7	3.94%	89.4
Box 2	34.8 ± 2	0.3 ±0.1	0.5 ±0.2	55.6	1.42%	91.2
Box 3	33.6 ± 3	1.1 ± 0.2	0.6 ± 0.2	53.3	5.70%	88.6
Box 4	33.7 ± 3	0.8 ± 0.2	0.6 ± 0.2	52.7	3.99%	87.8
Profile 1: 0-40 μm	33.4 ± 3	1.1 ± 0.3	0.5 ±0.2	55.4	5.42%	90.4
Profile 1: 40-160 μm	33.8 ±2	0.8 ± 0.2	0.6 ± 0.3	55.8	3.89%	91
Reference calcite 1 (porous)	38.1 ± 2	0.2 ± 0.1	<0.01	57.6	0.86%	96
Reference calcite 2 (non-porous)	40.0 ± 2	0.2 ± 0.1	<0.01	60.5	0.82%	100.1

77

Calcium is unevenly distributed in the spine. We find a region with a lower (33.4 wt-% ± 1.7 wt-% rectangle 1 in Figure 3.13) and a region with a higher calcium content, respectively (34.8 wt-% ±1.7 wt-% rectangle 2 in Figure 3.13). As calcium is the major element these variations result in a different total sum of observed elements: 89.4 wt-% and 91.2 wt-%, respectively. Within individual wedges calcium contents is distributed evenly.

Also magnesium is not distributed homogeneously within the spines (Figure 3.13). In about three quarters of the wedges, the Mg concentration in the outer, more bulky part of the wedges is lower (0.8 wt-% ±0.3 wt-%) in comparison to that present within the inner wedge portions (1.1 wt-% ±0.1 wt-%). The molar Mg/Ca ratio changes from 1.4 wt-% to 5.7 wt-%. Thus, there is an increase in Mg content from the outer rim towards the center of the spine.

Sodium is well detectable within spine calcite and has a homogeneous distribution pattern (0.5 wt-% ±0.25 wt-%, Table 3.9). The non-biologic calcite references have an average Ca-content of 38.1 wt-% ± 2 wt-% in case of the porous, opaque calcite and of 40.0 wt-% ± 2 wt-% in case of the clear, non-porous calcite. Both references have an average Mg-content of 0.2 wt-% (± 0.1 wt-%). This results in in a sum of observed elements of 96.0 wt-% for the opaque calcite and 100.7 wt-% for the clear calcite respectively (Table 3.9).

Material properties

Nanoindentation experiments were performed on both, longitudinal and transversal sections of the spine. The transversal section investigated with nanoindentation was the same sample that has been analyzed with EPMA. Nanoindentation testing was only possible on the wedges as the micro-porous spine parts broke under the indenter load and led to wrong hardness and E-modulus values. Nanoindentation experiments performed on the longitudinal section (Figure 3.14) of the spine revealed an average hardness of 4.3 ± 0.5 GPa and an average Young's modulus of 72.5 ± 7.0 GPa (Table 3.10). The hardness and E-modulus decreased slightly from the base to the tip of the spine (4.2 - 4.5. GPa) whereas the highest E-modulus was observed in the central portion of the spine length.

The transversal section of the spine shows a rather homogeneous hardness and E-modulus (4.2 - 4.5 GPa, 70 - 80 GPa respectively). However, one wedge shows a distinct lower hardness and E-modulus (3.3 - 3.9 GPa, 53 - 65 GPa, respectively) in comparison to the other wedges. Mechanically properties values of the transversal section of the spine (Figure 3.14) are slightly lower than those obtained from the longitudinal section. The average hardness is 4.0 ± 0.3 GPa and the average E-modulus is 58.0 ± 4.4 GPa (Table 3.10). The mechanical properties are homogeneously distributed within this section. The investigation of longitudinally and transversally sectioned spines by nanoindentation revealed an anisotropy of the average E-moduli, the E-modulus of the longitudinal section is 25% higher than that of the transversal section.
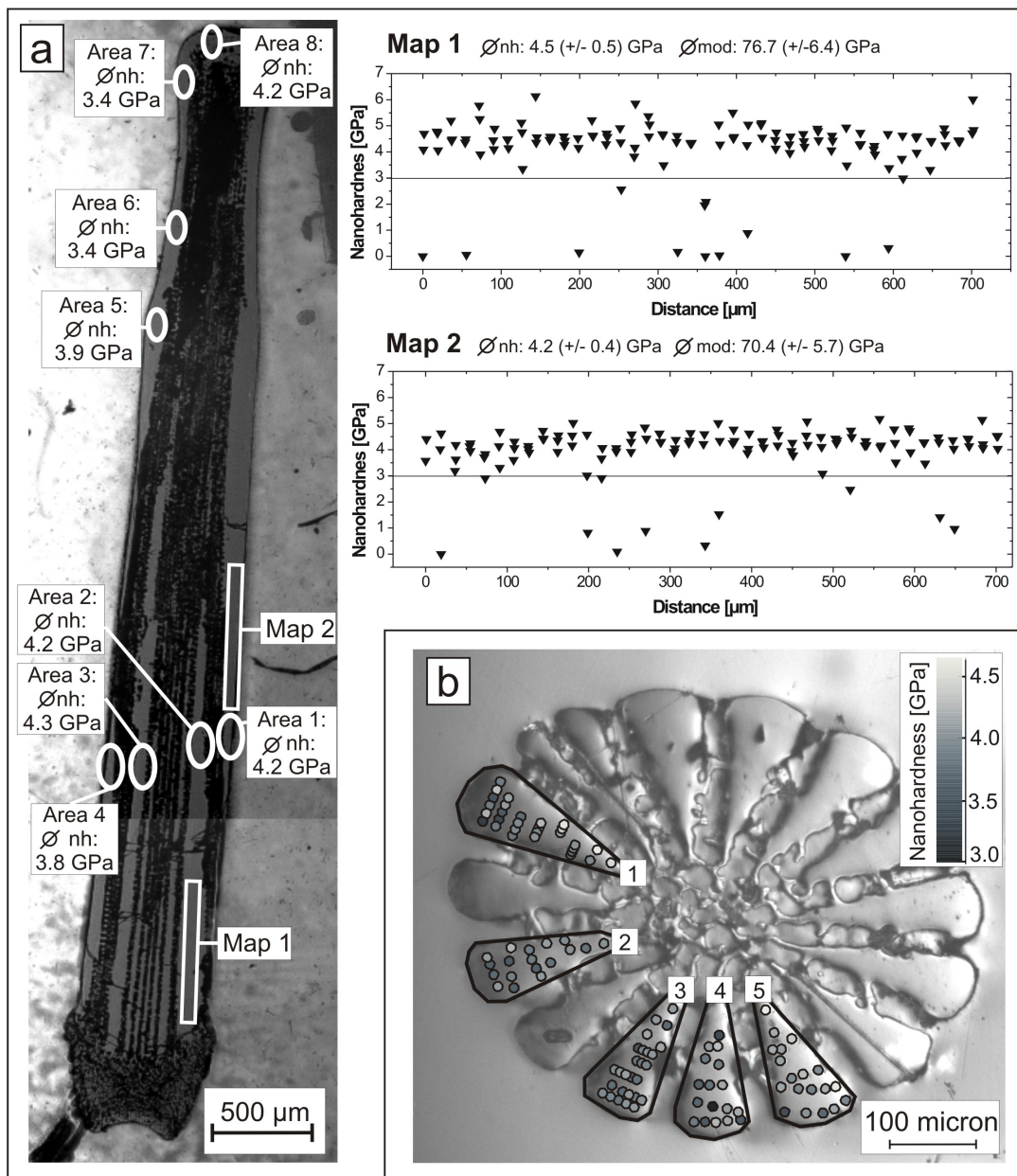
Figure 3.14: Locations on the spine of the indented areas, a) longitudinal section and b) transversal section. Corresponding hardness and E-modulus values are given in Table 3.10. There is an overall trend that the hardness of the material decreases from the base to the tip. The gray markers show the position of the single indents and the gray level represents the nanohardness. The investigated wedges are marked by numbers, these are also used in Table 3.10 and Table 3.9. No special pattern of hardness distribution is observable within the wedges.

Table 3.10: Nanoindentation testing results. The upper part of the table gives the results from a longitudinally sectioned sample, the lower part of the table from a transversally sectioned sample. Z is the number of valid indents.

	Nanohardness [GPa]	σ	E-Modulus [GPa]	σ	Z
Area1	4.24	0.23	69.65	1.78	5
Area 2	4.28	0.44	68.04	3.99	6
Area 3	4.40	0.17	69.01	1.82	6
Area 4	3.80	0.26	62.94	3.80	6
Area 5	4.27	0.55	66.99	4.43	6
Area 6	3.35	0.13	53.56	2.09	5
Area 7	3.41	0.33	53.37	2.00	4
Area 8	3.89	0.50	71.6	5.03	6
Map 1	4.52	0.49	76.65	6.38	107
Map 2	4.25	0.40	81.17	5.72	109
All longitudinal	4.31	0.50	72.53	7.04	260
Wedge 1	4	0.33	58.33	4.66	29
Wedge 2	3.91	0.20	56.19	3.29	18
Wedge 3	3.95	0.16	56.74	2.63	27
Wedge 4	3.87	0.35	57.57	3.69	17
Wedge 5	4.12	0.28	60.71	6.46	19
All transversal	3.97	0.28	58	4.37	110
All	4.21	0.47	68.23	9.2	370

3.5.4 Discussion

Spine Growth and Calcite Crystal Orientation during the Growth Process

The micro-growth lines observed in this study - that should not be mixed up with conventional growth lines resulting mainly from a change in porosity (e.g. Ebert 1986, Stump & Lucas 1990) - are due to the presence of organic matrices within the spine (Benson et al. 1983) and yield some information on the growth of a spine. The growth of sea urchin spines was extensively studied due to the fact, that spines can continue growing after breaking apart. The spine renewal mechanism (e.g. Dubois and Ameye 2001, Heatfield 1971, Märkel and Röser 1983) in different sea urchin species is similar. The regeneration of the spine starts with small conical prolongations (microspines) from the broken spine. These prolongations continue to grow parallel to the longitudinal axis of the spine and eventually form lateral branches. This process is consistent with the observed micro growth lines in the porous regimes of the spine that show concentric rings indicating growth in all directions. The concentric growth lines around two microspines overlap and join to one growth ring. The shape of the growth ring is a superposition of the individual shapes of growth lines around the microspines. We assume that in this process the slight differences in orientation between the two joining growth rings are compensated. Studies (Dubois & Ameye 2001, Heatfield 1971, Märkel & Röser 1983) of different sea urchin species show that after the initial process of growing and connecting microspines, resulting in lengthening of the spine, a second process leads to a thickening of the spines by building the wedges. As it can be observed from the micro growth lines, the wedges grow in a concentric manner around one single nucleus or microspine. Thus there is only influence of one nucleus, slight misorientations during growth cannot be compensated but can be accumulated leading to a slight tilt of the wedges, observed from the high angular resolution EBSD. This accumulation of disorder in the wedges was also found with synchrotron radiation techniques by Aizenberg et al. (1997): young spines consisting mainly of porous calcite show a higher degree of calcite ordering in comparison to spines of adult sea urchins, where wedges are also present in addition to porous calcite. A porous calcite microstructure allows more easily the compensation for orientation disorder in comparison to the wedges composed of solid calcite. This growth pattern differs from that of many other calcitic biominerals that are produced by competitive growth such as brachiopod shells (Goetz et al. 2009) or avian egg-shells (Dalbeck & Cusack 2006). Competitive growth results in a high co-orientation of calcite c-axes without a pronounced co-orientation of the a-axes directions. The spines in contrast are produced by a differing growth mechanism and exhibit a true single crystal like orientation behaviour. Moureaux et al. (2010) observed with conventional EBSD that sea urchin spines are single crystals (Moureaux et al. 2010). Previous high resolution EBSD studies of Goetz et al. (2010)could show the presence of small orientation differences up to 0.1° within a spine (Goetz et al. 2010). These differences - as also shown in the present study - appear between different wedges and result in a total misorientation of up to 0.6°. Thus careful EBSD analyses reveals that sea urchin spines are not single crystals.sorientation of up to 0.6°. Thus careful EBSD analyses reveals that sea urchin spines are not single crystals.

Patterns of Chemical Compositional Variation Within a Sea Urchin Spine

The magnesium content in sea urchin skeletons was studied for a long time by means of XRD (Magdans & Gies 2004, Weber 1969). Weber (1969) mentions that Temnopleuridea, the order of *H. porosissimus* has an average Mg concentration of 7.6 $\pm$ 1 mol-% Mg. However, we observed in this study an average MgCO$_3$ content of 3.9 mol-%. This discrepancy might be due to the fact that the Mg content was determined by measuring the calcite lattice constants by Weber (1969). In an inorganically precipitated calcite the Mg content is determined by smaller lattice parameters due to the smaller Mg ion on Ca positions. This is not necessarily the case in calcites that were precipitated by biologic mediation as there is a strong influence of organic molecules on the lattice parameters (Pokroy et al. 2006). Thus studies that determine Mg content of biominerals by lattice parameters should be handled cautiously.

Sodium in sea urchin spines was detected with both, EPMA and TEM analyses. Even though sample preparation was different for the two techniques, both included extensive polishing and grinding with tap water. Regarding the microprobe samples the same sample preparation (and the same tap water) was used for the preparation of inorganic calcite standards. These standards did not show any signs of sodium in the EPMA analyses. Whereas it is commonly assumed that sea urchin calcite does not contain Na, we find it also in sea urchin tooth calcite (Section 3.6).

The total sum of observed elements (plus calculated carbonate) is usually around 90 wt-% in the spines. The missing 10 % can be explained by the nano-pores that were observed in TEM. This finding is in concert with the observation that the geologic non-porous calcite shows a total sum of elements of sightly above 100 wt-% whereas the porous geologic calcite shows a sum around 96 wt-%. This indicates that there is no homogenous distribution pattern of nano-pores within the investigated sea urchin spines. The different content of pores might result from a different orientation of the pores towards the animal, a notion we did not consider any further in the study.

Assuming a concentric growth of a spine indicates that the Mg/Ca ratio can vary within spine material by several weight percent even when it grows at the same time (Figure 3.13 rectangles 3 & 4 and Table 3.9). Ca and Mg variations that are taken for paleoenvironmental studies are in the same order of magnitude (Ries et al. 2002). Thus paleoclimate and paleoseawater reconstructions have to account for those inhomogeneities.

Pore Size Distribution and Pore Distribution Patterns Within Sea Urchin Spines

The most intriguing feature of the TEM analyses are the very abundant nanometer sized pores within sea urchin calcite. We interpret these as pores that are filled with organic material in the living organism. As it is known that amorphous CaCO$_3$ (ACC) occurs in the stereom (Beniash et al. 1997, Politi et al. 2004) these pores could also result from the lower mechanical resistance of ACC to the ion-milling. This explanation can be excluded as the pores are not cylindrical but show a spher-

ical shape. Also solution of the ACC during sample preparation can be excluded as water was only involved in the very first preparation steps and the investigated material was never in contact with water. Similar pores were observed by *Heterocentrotus trigonarius* (Su et al. 2000) with the difference that the pores had a homogeneous size in that study and where interpreted as protein-inclusions. We expect them to be filled with extracellular organic matter, as they are too small to contain cells. Proteins or glycoproteins would be a good guess as it was shown in several studies that they are present within the calcite of sea urchin spines (Aizenberg et al. 1997, Ameye et al. 2001, Berman et al. 1988, Weiner 1985).

Mechanical Properties of Sea Urchin Spines

Nanoindentation on sea urchin spines was applied in different studies but it is not easy to compare them: Moreaux et al. (2010) applied 50 mN and to investigate both, stereom and wedges of Paracentrotus lividus and Presser et al. (2010) used 15 mN, only evaluating the first 100 nm of indentation, resulting in around 1 mN to investigate the stereom of *Heterocentrotus mammillatus*, *Phyllcanthus imperialis* and *Prinocidaris baculosa*. In our study we applied around 6-7 mN to investigate only the wedges. These low indentation depth used by Presser et al. (2010) are problematic and usually not used in nanoindentation as they lead to wrong results: the contact between indenter tip and sample is not completely established due to several factors (oscillation of the tip in CSM mode, deformation of the sample surface roughness and others). Furthermore is the tip never perfectly sharp, one usually assumes a radius of 50 nm, meaning that the indenter tip shape during the first 100 nm of indentation can be approximated more by a sphere then by a pyramid. The equations to calculate the mechanical properties are only valid when using the correct description of the indenter geometry.

Even though it is hard to compare the absolute values due to the factor of ten in applied force we found, as (Moureaux et al. 2010) did, that there is no correlation between mechanical properties and magnesium content, an explanation that is usually given to explain hardness differences in calcitic biominerals (Lowenstam 1981, Magdans & Gies 2004, Märkel et al. 1986, Wang et al. 1997). It has been shown on non-biological composites that a higher content of organic polymers in the composites increases its hardness (Lipowsky et al. 2007) and it was speculated that this mechanism might also have influence on sea urchin teeth (Section 3.6). The pores we observed in this study hint to such a mechanism also in sea urchin spines.

Presser et al. (2010) investigated transversal sections and most of the indentations were done in the porous stereom. The obtained hardness and E-modulus are slightly lower than those obtained in this study. Anyhow, the spines of *Prinocidaris baculosa* also showed small wedges in the outer part. Presser and co-workers (2010) found an average E-modulus of 71.3 ± 3.8 GPa and hardness of 3.5 ± 0.2 GPa. In the present study we report the hardness on transversal sections to be 4 ±0.3 GPa and an E-modulus of 58 ±4 GPa. This difference might be due to the evaluation of hardness. We calculated mechanical property values only from an indentation depth of 100-300 nm whereas Presser et al. (2010) calculated hardness and E-modulus from 0-100 nm, a choice that is problematic due to the reasons mentioned above. We could observe a slight decrease of hardness from the base to the tip of the spine from 4.5

- 4.2 GPa and there was one wedge that was over all the length of the spine softer (around 3.8 GPa) than all the other spines (4.2 GPa).

3.5.5 Concluding Summary

1. The single crystalline nature of sea urchin spines is achieved by a high density of microspines. A decrease in the density or/and the abundance of the microspines also decreases the perfection of the single crystallinity. Therefore we observe a tilt between the different wedges of the spine. These nucleate from only one microspine.

2. Sea urchin calcite contains 0.5 wt-% Na that is evently distributed within the spine.

3. The Mg/Ca ratio within a specific spine is not constant. Thus environmental reconstructions based on the Mg/Ca system are not feasible.

4. For sea urchin spines, we do not find a correlation between Mg contents of the bio-calcite and properties of the biological material. This is in contrast to other biological calcites, such as sea urchin teeth, where we observe a strong correlation between hardness and Mg contents of the calcite.

5. We find that the mechanical properties of sea urchin spines are correlated to the organic material present in nanopores within the spine. These pores have sizes ranging from 3 - 400 nm.

ACKNOWLEDGEMENTS

References

Aizenberg, J., Hanson, J., Koetzle, T.F., Weiner, S., Addadi, L. (1997): Control of macromolecule distribution within synthetic and biogenic single calcite crystals. Journal of the American Chemical Society, 119, 881-886.

Ameye, L., De Becker, G., Killian, C., Wilt, F., Kemps, R., Kuypers, S., Dubois, P. (2001): Proteins and saccharides of the sea urchin organic matrix of mineralization: Characterization and localization in the spine skeleton. Journal of Structural Biology, 134, 56-66.

Beniash, E., Aizenberg, J., Addadi, L., Weiner, S. (1997): Amorphous calcium carbonate transforms into calcite during sea urchin larval spicule growth. Proceedings of the Royal Society of London Series B-Biological Sciences, 264, 461-465.

Benson, S., Jones, E.M.E., Crisebenson, N., Wilt, F. (1983): Morphology of the Organic Matrix of the Spicule of the Sea-Urchin Larva. Experimental Cell Research, 148, 249-253.

Berman, A., Addadi, L., Weiner, S. (1988): Interactions of Sea-Urchin Skeleton Macromolecules with Growing Calcite Crystals - a Study of Intracrystalline Proteins. Nature, 331, 546-548.

Chen, C.C., Lin, C.C., Liu, L.G., Sinogeikin, S.V., Bass, J.D. (2001): Elasticity of single-crystal calcite and rhodochrosite by Brillouin spectroscopy. American Mineralogist, 86, 1525-1529.

Currey, J.D., Nichols, D. (1967): Absence of Organic Phase in Echinoderm Calcite. Nature, 214, 81-83.

Dalbeck, P., Cusack, M. (2006): Crystallography (electron backscatter diffraction) and chemistry (electron probe microanalysis) of the avian eggshell. Crystal Growth & Design, 6, 2558-2562.

Dickson, J.A.D. (2002): Fossil echinoderms as monitor of the Mg/Ca ratio of phanerozoic oceans. Science, 298, 1222-1224.

Donnay, G., Pawson, D.L. (1969): X-Ray Diffraction Studies of Echinoderm Plates. Science, 166(3909), 11147-1150.

Dubois, P., Ameye, L. (2001): Regeneration of spines and pedicellariae in echinoderms: A review. Microscopy Research and Technique, 55, 427-437.

Ebert, T.A. (1986): A New Theory to Explain the Origin of Growth Lines in Sea-Urchin Spines. Marine Ecology-Progress Series, 34, 197-199.

Goetz, A., Griesshaber, E., Schmahl, W.W. (2010): An Easy Approach to Increase the Precision of EBSD Analyses - Examples from a Sea Urchin Calcite Study. Solid State Phenomena, 160, 229-234.

Goetz, A.J., Griesshaber, E., Neuser, R.D., Lüter, C., Hühner, M., Harper, E., Schmahl, W.W. (2009): Calcite morphology, texture and hardness in the distinct layers of rhynchonelliform brachiopod shells. European Journal of Mineralogy, 21, 303-315.

Heatfield, B.M. (1971): Growth of Calcareous Skeleton during Regeneration of Spines of Sea Urchin, *Strongylocentrotus purpuratus* (Stimpson) - Light and Scanning Electron Microscopic Study. Journal of Morphology, 134, 57–89.

Hermans, J., Borremans, C., Willenz, P., Andre, L., Dubois, P. (2010): Temperature, salinity and growth rate dependences of Mg/Ca and Sr/Ca ratios of the skeleton of the sea urchin Paracentrotus lividus (Lamarck): an experimental approach. Marine Biology, 157, 1293-1300.

Lipowsky, P., Hirscher, M., Hoffmann, R.C., Bill, J., Aldinger, F. (2007): Zinc oxide microcapsules obtained via a bio-inspired approach. Nanotechnology, 18, 165603.

Lowenstam, H.A. (1981): Minerals Formed by Organisms. Science, 211, 1126-1131.

Magdans, U., Gies, H. (2004): Single crystal structure analysis of sea urchin spine calcites: Systematic investigations of the Ca/Mg distribution as a function of habitat of the sea urchin and the sample location in the spine. European Journal of Mineralogy, 16(2), 261-268.

Märkel, K., Röser, U. (1983): The Spine Tissues in the Echinoid Eucidaris-Tribuloides. Zoomorphology, 103, 25-41.

Märkel, K., Röser, U., Mackenstedt, U., Klostermann, M. (1986): Ultrastructural Investigation of Matrix-Mediated Biomineralization in Echinoids (Echinodermata, Echinoida). Zoomorphology, 106, 232-243.

Meldrum, F.C., Cölfen, H. (2008): Controlling Mineral Morphologies and Structures in Biological and Synthetic Systems. Chemical Reviews, 108, 4332-4432.

Moureaux, C., Perez-Huerta, A., Compere, P., Zhu, W., Leloup, T., Cusack, M., Dubois, P. (2010): Structure, composition and mechanical relations to function in sea urchin spine. Journal of Structural Biology, 170, 41-49.

Oneill, P.L. (1981): Polycrystalline Echinoderm Calcite and Its Fracture-Mechanics. Science, 213, 646-648.

Paquette, J., Reeder, R.J. (1990): Single-Crystal X-Ray Structure Refinements of 2 Biogenic Magnesian Calcite Crystals. American Mineralogist, 75, 1151-1158.

Pokroy, B., Fitch, A.N., Marin, F., Kapon, M., Adir, N., Zolotoyabko, E. (2006): Anisotropic lattice distortions in biogenic calcite induced by intra-crystalline organic molecules. Journal of Structural Biology, 155, 96-103.

Politi, Y., Arad, T., Klein, E., Weiner, S., Addadi, L. (2004): Sea urchin spine calcite forms via a transient amorphous calcium carbonate phase. Science, 306, 1161-1164.

Pouchou, J.L., Pichoir, F. (1984): A New Model for Quantitative X-Ray-Microanalysis .1. Application to the Analysis of Homogeneous Samples. Recherche Aerospatiale, 3, 167-192.

Presser, V., Gerlach, K., Vohrer, A., Nickel, K.G., Dreher, W.F. (2010): Determination of the elastic modulus of highly porous samples by nanoindentation: a case study on sea urchin spines. Journal of Materials Science, 45, 2408-2418.

Ries, J.B. (2004): Effect of ambient Mg/Ca ratio on Mg fractionation in calcareous marine invertebrates: A record of the oceanic Mg/Ca ratio over the Phanerozoic. Geology, 32, 981-984.

Schmidt, W.J. (1930): Die Skelettstücke der Stachelhäuter als Biokristalle. Zoologisches Jahrbuch Allgemeine Zoologie, 47, 357-510.

Smith, A.B. (1980): Stereom Microstructure of the Echinoid test. Special Papers in Palaeontology, 25.

Strathmann, R.R. (1981): The Role of Spines in Preventing Structural Damage to Echinoid Tests. Paleobiology, 7, 400-406.

Stump, R.J.W., Lucas, J.S. (1990): Linear Growth in Spines From Acanthaster-Planci (L) Involving Growth Lines and Periodic Pigment Bands. Coral Reefs, 9, 149-154.

Su, X., Kamat, S., Heuer, A.H. (2000): The structure of sea urchin spines, large biogenic single crystals of calcite. Journal of Materials Science, 35, 5545-5551.

Tsipursky, S.J., Buseck, P.R. (1993): Structure of Magnesian Calcite from Sea-Urchins. American Mineralogist, 78, 775-781.

Wang, R.Z., Addadi, L., Weiner, S. (1997): Design strategies of sea urchin teeth: Structure, composition and micromechanical relations to function. Philosophical Transactions of the Royal Society of London Series B-Biological Sciences, 352, 469-480.

Weber, J.N. (1969): Incorporation of Magnesium into Skeletal Calcites of Echinoderms. American Journal of Science, 267, 537-566.

Weiner, S. (1985): Organic Matrix-Like Macromolecules Associated with the Mineral Phase of Sea-Urchin Skeletal Plates and Teeth. Journal of Experimental Zoology, 234, 7-15.
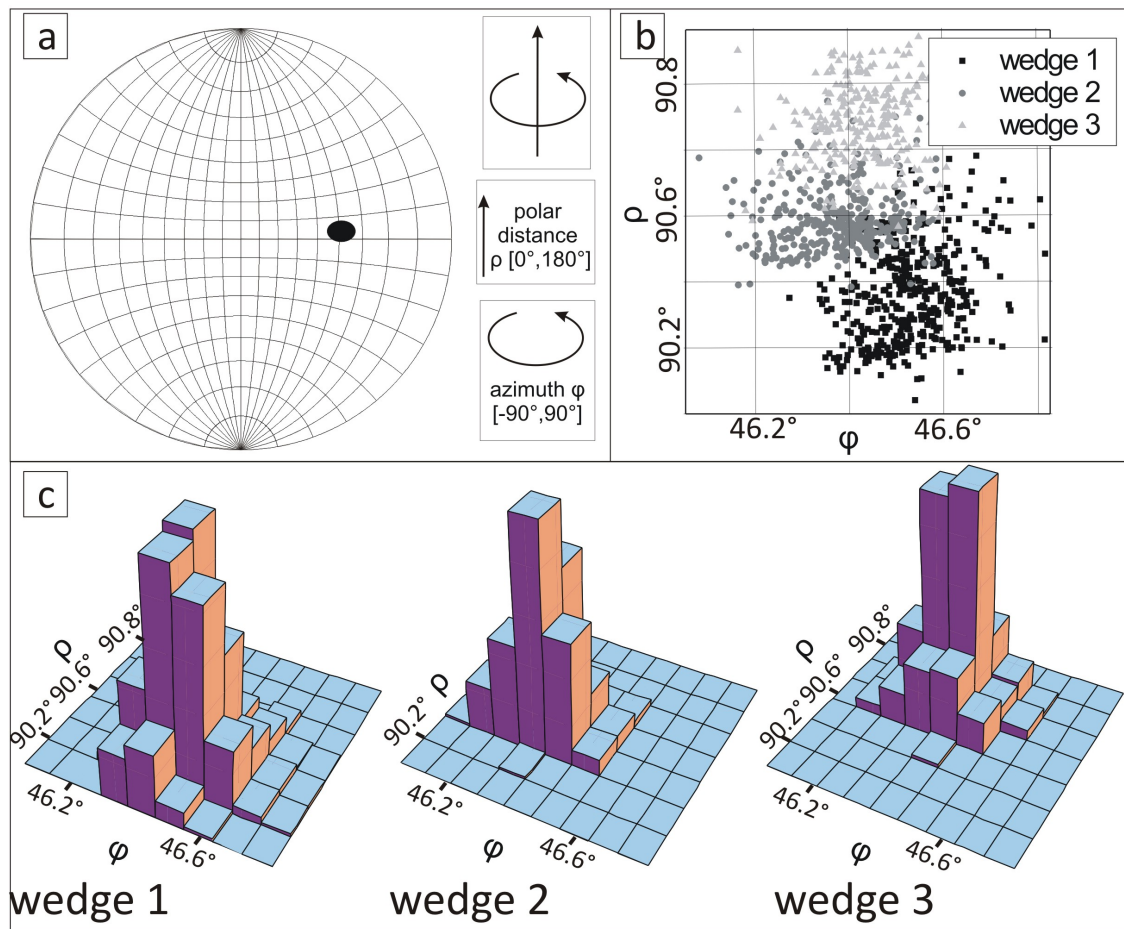
Appendix

Figure 3.15: a) Wulff's net and angles that were used for the construction of the pole figures shown in this study. The polar distance ranges from 0°-180° starting in the downer part of the figure and the azimuthal distance ranges from -90° - 90° from the left to the right part of the figure. The black dot in Figure 3.15a shows the data given in the pole figure section of Figure 3.15b. Figure 3.15b is a magnification of one portion of the pole figure obtained from data points of profile 1 in Figure 3.11. The squares correspond in Figure 3.11 to wedge 1, the circles to wedge 2 and the rhombs to wedge 3. Figure 3.15c shows the 3D-histograms that represent the frequency of indexed orientations of the pole figure shown in Figure 3.15b.

3.6 Biomechanical functionalisation by composite crystal hierarchical architectures: crystallography of the tooth of the sea urchin *Paracentrotus lividus*

Abstract

The crystallographic architecture of the hierarchical composite crystal of the tooth of the sea urchin *Paracentrotus lividus* was investigated together with variations in chemical composition and nanomechanical properties by micro-/ nano-tomography, scanning-electron-microscopy, electron-backscatter-diffraction, electron-beam-micro-analysis, and nanoindentation testing.

Sea urchin teeth are Mg-calcite hybrid composites, forming a hierarchical composite crystal. This architecture consists of the slightly (3-5°) misoriented major structural units (i.e. stone, lamellar needle complex, prisms, primary-, secondary- and carinar process plates), each of which is assembled of subunits, such as single platelets, which are again misoriented by 1-2° relative to each other. The misorientation is systematic. The crystallographic orientation rotates with the curvature of the tooth. The crystallographic direction of the growth is [631]. The mirror plane parallel to the keel of the tooth is the a*-c*-plane, perpendicular to [010]. The self-sharpening feature of the tooth is enabled by the close interplay of the highly evolved micro- to nanostructure, specific textural properties of constituting structural elements, distinct calcite grain size variations and gradients in the amount of incorporated organic polymers. The Mg-calcite composite crystal is distinctly harder than inorganic calcite and exceeds even the hardness of dolomite. A strong structuring of mechanical properties has been observed which is mainly correlated with the magnesium contents. The nanohardness of the tooth scatters between 3.5 GPa and values over 8 GPa, showing a consistently higher hardness than non-biological calcite (3.0 GPa) and dolomite (7.3 GPa) and almost reaching the hardness of magnesite (9.2 GPa).

3.6.1 Introduction

Sea urchin spines and skeleton plates have long been considered as prototypes for biologically formed large single crystals of Mg-calcite since they appeared to be perfect in polarized light and diffraction experiments (e. g. Currey and Nichols 1967, Goetz et al. 2010, Magdans and Gies 2004, Paquette and Reeder 1990, Schmidt 1930, Su et al. 2000). The teeth of sea urchins also consist of Mg-calcite and macroscopically show a single-crystalline appearance (Giesbrecht, 1880, Kniprath 1974, Märkel 1969, Märkel 1990, Märkel and Gorny 1973, Märkel et al. 1977). Calcite is a relatively soft and perfectly brittle mineral. Thus, for sea urchins a material optimization and strength enhancement of the calcite of their teeth is necessary in order to enable them to graze on hard sea floor substrates (e. g. Hozman 1983, Ma et al. 2008). As a consequence the calcitic teeth exhibit a unique and highly purpose-optimized microstructure to achieve the required mechanical properties. The masticator apparatus of a sea urchin (also called Aristotle's lantern) consists of a set of five convoluted teeth (e. g. Märkel 1990). These join at the anterior end of the masticator apparatus, where the animal grazes on the floor substrate and thus constantly grinds off the tips of the teeth. Correspondingly, the tooth is produced continuously at its posterior end, the plumula (Märkel 1990). The complex structure and development of the teeth has been described by Salter (Salter, 1861) and Giesbrecht (Giesbrecht, 1880). It was intensively reinvestigated in the 1970's (Kniprath 1974, Märkel 1969, Märkel and Gorny 1973, Märkel et al. 1977) and literature cited by Märkel 1990), and again recently by Robach et al. (Robach et al. 2005, Robach et al. 2006, Robach et al. 2009) and Stock et al. (Stock and Veis 2003, Stock et al. 2002, Stock et al. 2003a, Stock et al. 2003b, Stock et al. 2004a, Stock et al. 2004b, Stock et al. 2001, Stock et al. 2003c, Stock et al. 2003d) with additional key contributions of Wang et al. (1997), Ma et al. (Ma et al. 2008, Ma et al. 2009) and Killian et al. (2009). The tooth is a T-shaped girder which is curved along its longitudinal axis. Its cross-section shows a complex array of several major structural units. These are essentially a core of a hard and tough Mg-calcite fibre composite material which is encased in an assemblage of platy calcite elements. The composite material of the core has been described as calcite fibres reinforced by a matrix of very-high Mg-calcite (Killian et al. 2009, Ma et al. 2009). This composite further contains organic membranes separating the calcite fibres and matrix particles (Wang et al. 1997). This hard core unit is also called the stone and it resides at the junction of the "vertical" and "horizontal" lines of the T. The fibres of the stone have cross-sections in the order of 1 micrometre. According to (Wang et al. 1997) they extend through the adjacent lamellar needle complex and finally become the "prisms" of the keel (the vertical line of the "T"), where they reach a thickness of 20 micrometres. The platy elements encasing the stone and the prisms are distinguished into primary plates, secondary plates, and carinar process plates (Kniprath 1974, Märkel 1969, Märkel 1990, Märkel and Gorny 1973, Märkel et al. 1977, Robach et al. 2009). All units of the tooth show a single-crystal like crystallographic orientational coherence where at least two distinct (although quite similar) orientations were reported (Kniprath 1974, Ma et al. 2009, Märkel 1969, Märkel 1990, Märkel and Gorny 1973, Märkel et al. 1977). Rohbach et al. (2009) investigated the structure of the mineralized elements of the sea urchin *Lytechinus variegatus* and reported that the tooth is

formed during two distinct stages: First, the array of primary plates forms and is followed by the mineralization of the fibres of the stone and the secondary plates. Tooth mineralization is finished with the extension of the secondary plates to form the carinar process plates and the broadening of calcite needles between the carinar process plates to build the prisms (Robach et al. 2009). Wang et al. (1997) report that the initial mineralization occurs in the form of amorphous calcium carbonate (ACC), which subsequently crystallizes as the tooth matures. Most importantly the so-called "discs", the reinforcing nanoparticles, are implanted as ACC between the fibres or the plates after these latter elements have been formed. The crystallization product of this ACC is finally the very high-Mg-calcite (protodolomite) particle matrix reinforcing the fibrous or platy composite material in the mature tooth.

Sea urchin tooth calcite is significantly harder than non-biologic calcite and has a hardness that is close to that of dolomite (e.g. Hozman 1983, Ma et al. 2008, Schultz 2005). The structuring of the hardness and E-modulus according to the main structural units has been investigated with Vickers microhardness (Märkel and Gorny 1973, Wang et al. 1997) and recently by Ma et al. (2008) with instrumented nanoindentation. As the tooth edges are permanently ground down during feeding, sea urchins continuously grow their teeth. A complete regeneration of the teeth of *Strongylocentrotus purpuratus* was carried out under laboratory conditions and took about three months (Holland 1965), amounting to about 250 micrometres per day. The continuous abrasion at the tooth tip is accompanied by a perpetual self-sharpening mechanism (Wang et al. 1997). This poses additional functional requirements on the constitution of the teeth on top of strength and hardness. This is enabled through an interplay of several factors: the mode of arrangement of major structural units at distinct scale levels, the mode of crystal orientation within each major structural unit, chemical differences between and within the different tooth structural units and a grading of the organic-inorganic composite nature of the tooth.

In the present paper we focus on the crystallographic register of the different calcite units and elements constituting the tooth, a basic prerequisite to understand its functionality. In addition, computed tomography data, hardness and chemical information was collected to ensure that the results can be correlated correctly with the major structural units described in the literature.

The sea urchin species *Paracentrotus lividus* has been chosen for these investigations due to their high biological ubiquity in shallow water ($\sim$ 10 m) and their 2-3 cm long teeth.

3.6.2 Samples and Sample Preparation

Specimens of *Paracentrotus lividus* were collected at Côte Vermeille, Banyuls sur Mer, Mediterranean Sea, France. Tooth samples were cut in two different directions along their longitudinal axis resulting in a coronal and a sagittal cut. A detailed illustration of the cut lines is given in the Appendix (Figure 3.28). The obtained sections were fixed to a glass slide and were ground down to a thickness of 300 to 400 micrometres. A highly smooth sample surface was obtained by polishing the samples with a diamond paste containing 0.25 micrometre sized diamond particles

in the final step. For electron backscatter diffraction (EBSD) analysis an additional attack-polishing with a suspension of alumina nanoparticles was applied for 4-5 minutes. For SEM and EBSD analyses the samples were coated with a 5 to 10 nm thin layer of carbon. For electron microprobe analyses (EPMA) the samples were coated with 15 nm of carbon. We investigated two teeth with nanoindentation, one tooth with EBSD analysis and one tooth with EDX and one with EPMA mapping.

3.6.3 Methods

Tomographical mapping of the teeth was carried out with a Metris X-Tek HMX ST microtomography system. Nanotomographical imaging was performed with a Gatan X-ray Ultra-Microscope (XuM) where a high-resolution 3D x-ray tomography accessory was attached to a Philips XL30 SEM.

Nanoindentation measurements were performed with an MTS nanoindenter (SA2) equipped with a continuous stiffness measurement (CSM) indenter-head. The measurements were performed with a Berkovich indenter tip to an indentation depth of 300 nm and a CSM frequency of 45 Hz. The strain frequency was set to 0.2 Hz. An isotropic Poisson's ratio of 0.3 was assumed for the investigated biological material. Indentation depth for all indents was set to 300 nm. For the CSM indentation we report the average hardness between 100 and 300 nm depths. The data taken below 100 nm depth are discarded since the radius of curvature of the indenter tip is approximately 50 nm. Since the indented biological material is highly structured the validity of all indentation measurements was checked after indentation by light microscopy, SEM and histogram analysis. All indents that were placed at the boundary of two distinct structural units or at the edge of a hole were discarded.

EBSD analyses were performed on a JEOL JSM 6500 F field emission SEM, using 20 kV accelerating voltage. The signal from the sample that was tilted to 70° was detected with a Nordlys detector and was indexed by the HKL CHANNEL 5 software. The three Euler angles are shown in RGB colours. In order to emphasize small orientation differences only a range of 8° to 12° of each Euler angle was plotted. Indexing of the Kikuchi patterns of the stone was the least successful due to a lower Kikuchi pattern quality that was encountered in this portion of the tooth.

Chemical data were obtained by electron microprobe analysis (EMPA) using a CAMECA SX100 system operated at 15 keV acceleration voltage and 20 nA beam current. Measurement time per point was 60 ms. In order to avoid beam damage an electron beam spot size of 5 μm was chosen. Synthetic wollastonite (Ca,Si), periclase (Mg), hematite (Fe), albite (Na) and orthoclase (K) were used as standards. Matrix correction was performed by the PAP procedure (Pouchou and Pichoir, 1984). The reproducibility of standard analyses was <1% for each routinely analysed element. The PAP corrected data were stoechiometrically calculated as carbonate.

3.6.4 Results

Tomography

In order to visualize the teeth arrangement within the masticator apparatus, the mode of overlap of the teeth tips and the occurrence of fine-scale internal structural

units micro- and nano-tomography imaging was performed on both, an entire masticator apparatus as well as on single mature teeth (Figures 3.16, 3.17 and 3.18). A set of five teeth is present in the masticator apparatus of Paracentrotus lividus (Figures 3.16a, 3.16b, 3.16c). Each tooth is curved (Figures 3.16d, 3.16e and 3.16f) and extends from the top to the bottom part of the Aristotle's lantern (Figure 3.16a). At the bottom of the masticator apparatus the tips of the five teeth join (Figure 3.16c) and overlap slightly (Figures 3.16e, 3.16f, Figure 3.17a). The keeled sea urchin teeth exhibit a T shaped cross section (Figures 3.16e, 3.17a and 3.18).

Computed nano-tomography imaging (Figures 3.17b 3.17c, 3.18) reveals the major structural units that compose the tooth: the primary plates (pp) and secondary plates (sp) units together with the lamellar needle complex (lnc, Figure 3) encasing the stone (st). The keel (Figures 3.17c, 3.18) consists in its central portion of the lamellar needle complex (lnc) and the prisms (pr). These units are flanked at both sides along the keel by the carinar process plates (Figures 3.17c, 3.18). The keel together with the primary/secondary plates is visualized in top (Figures 3.17b) and bottom (Figures 3.17c) views and in a computed section performed perpendicular to the long axis of the tooth (Figure 3.18).

Nanoindentation

Nanoindentation experiments were performed on sea urchin tooth samples with two different modes of sectioning: the sagittal cut (Figure 3.19) and the coronal cut (Figure 3.20). Using the same instrumental settings the hardness of calcite, dolomite and magnesite was tested on their (104) cleavage faces. The results are summarized in Table 3.11. Seven nanoindentation maps were measured for each cut in different locations along the tooth and jaw (as indicated in Figures. 3.19 and 3.20). The maps on the tooth cover several of the major structural units of the tooth (Table 3.11). The nanohardness and Young's modulus of sea urchin teeth are stratified: the primary plates region is comparatively hard (4.6 GPa in the sagittal cut, 5.0,GPa in the coronal cut), the stone unit is extremely hard (average H = 5.7 GPa) and the needles/prisms units and secondary plates units give slightly lower hardness values than the primary plates unit (Table 3.11). For the primary plates and the secondary plates the microstructure allowed many valid nanoindents. This was much less the case for the stone and the needles/prisms units, where indents often broke into a cavity. These values were discarded.

The highest observed nanohardness value for the tooth of *Paracentrotus lividus* is 8.8 ± 0.4 GPa and was found in the stone (see individual nanohardness values in the hardness versus position diagrams in Figure 3.19). This value exceeds that of dolomite (7.3 GPa, Table 3.11) and is almost three times higher than that obtained for non-biologic calcite (3.0 GPa, Table 3.11). As an average Young's modulus for the tooth material of *Paracentrotus lividus* we obtained 64.6 GPa with a standard deviation of 12 GPa, and a maximum Young's modulus of 136.9 GPa was measured. Again this maximum value by far exceeds the Young's modulus of calcite (70 GPa, Table 3.11) and falls between the Young's moduli of dolomite (111 GPa, Table 3.11) and magnesite (145 GPa, Table 3.11). In Table 3.11 we also show the averaged hardness and E-modulus values for each map to indicate that in the sagittal cut there is a clear trend from higher to lower hardness and E-modulus from the tip
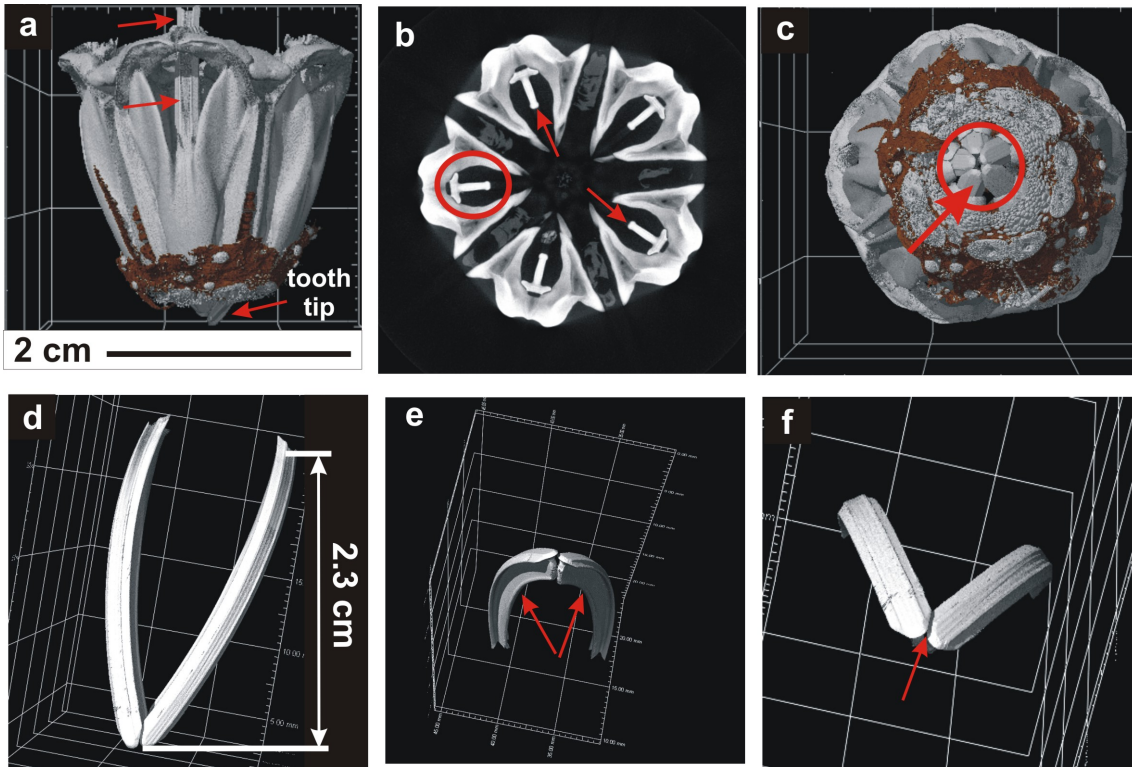
Figure 3.16: Computed micro-tomography images of the masticator apparatus of the sea urchin *Paracentrotus lividus*. Images 3.16a, 3.16b and 3.16c show the entire masticator apparatus with views from the top (3.16b), the bottom (3.16c) and from the side (3.16a). Arrows in Figures a, b and c point to single teeth. Figures 3.16d, 3.16e and 3.16f show micro-tomography images of single teeth: its curved shape and their overlapping. The keeled form of the teeth is well visible in Figures 3.16b and 3.16e.
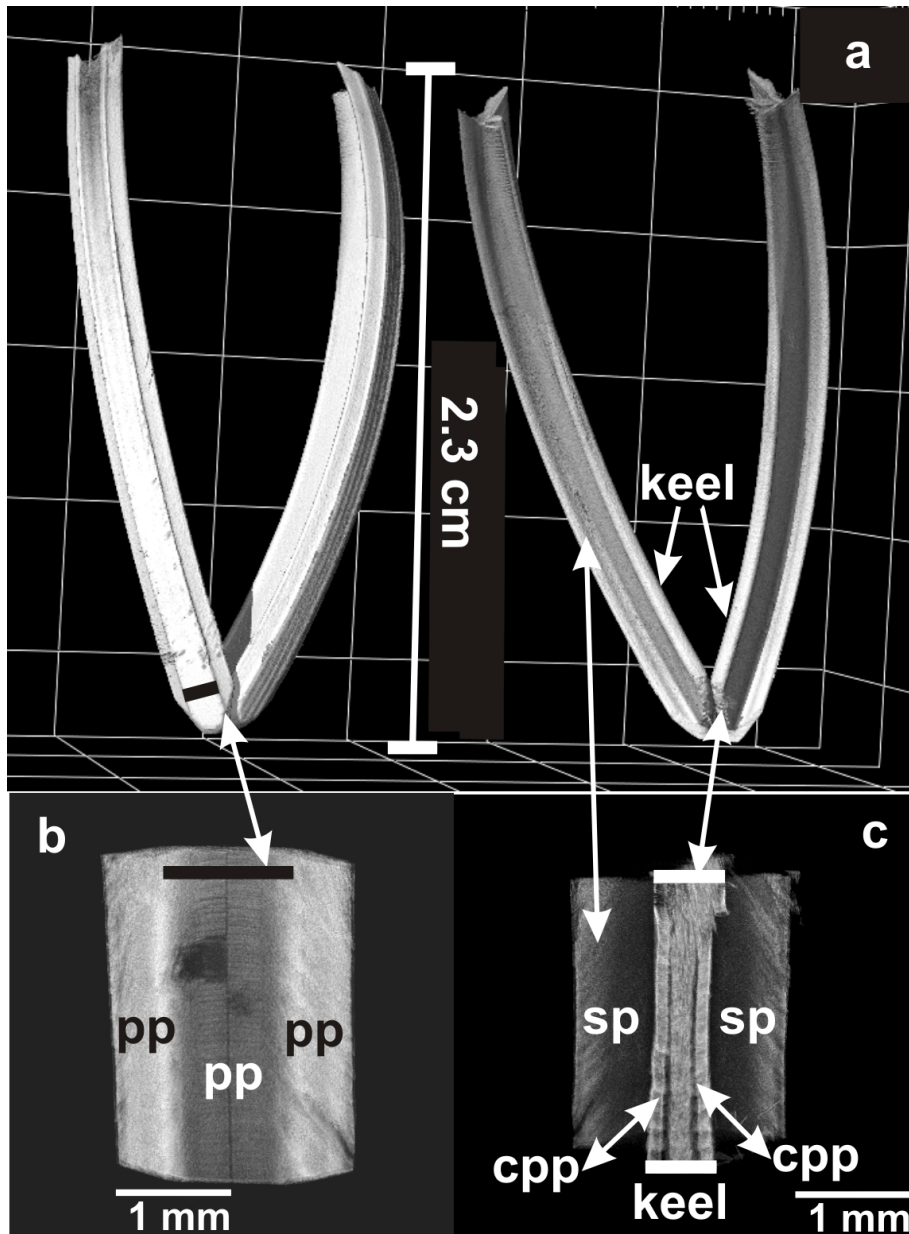
Figure 3.17: Computed micro- and nano-tomography images of the teeth of the sea urchin *Paracentrotus lividus*. Figure 3.17a highlights the external shape of the tooth viewed from the top (left hand image) and the bottom side (right hand image). Figures 3.17b and 3.17c reveal the highly structured architecture of the tooth and show some of its distinct structural units, the primary (pp) and the secondary plates (sp) and the keel with the carinar process plates (cpp) on its sides.

Table 3.11: Nanoindentation data obtained from a sagittal and a coronal section of the tooth as well as from the inorganic references calcite, magnesite and dolomite. We give averages for each map (see Figures 3.19 and 3.20) as well as averages for the different main structural units covered by the maps. Z is the number of valid indents.

|	Nanohardness [GPa]	σ	E-Modulus [GPa]	σ	Z
Sagittal section					
Map 4 - jaw (Figure 3.19)	4.3	0.5	76	10	13
Map 6 - jaw (Figure 3.19)	4.8	0.5	82	5	11
Average value for the jaw	**4.6**	**0.5**	**79**	**9**	**24**
Map 1 (Figure 3.19)	4.6	0.5	79	9	24
Map 2 (Figure 3.19)	4.7	0.6	79	9	5
Map 3 (Figure 3.19)	4.6	0.7	82	13	29
Map 5 (Figure 3.19)	4.3	0.7	68	10	8
Map 7 (Figure 3.19	4	0.8	60	13	9
Primary plates (saggital cut)	4.6	0.6	78	9	39
Stone	5.7	1.5	93	20	11
Neddles/prisms	4.4	0.7	76	16	26
Carinar process plates	4.7	0.8	69	7	7
Average value for the tooth	**4.6**	**0.9**	**76**	**15**	**105**
Coronal section					
Map 1 (Figure 3.20)	5.3	0.7	77	8	18
Map 2 (Figure 3.20)	5.1	0.5	63	7	26
Map 3 (Figure 3.20)	5.0	0.5	53	7	26
Map 4 (Figure 3.20)	5.1	0.8	601	10	29
Map 5 (Figure 3.20)	5.2	0.5	66	4	38
Map 6 (Figure 3.20)	5.3	0.8	63	7	39
Map 7 (Figure 3.20)	5.3	0.8	63	7	39
Primary plates	5.0	0.6	63	7	97
Secondary plates	4.5	0.6	64	6	147
Keel	5.3	0.6	64	6	147
Average value for the tooth	**5.2**	**0.6**	**64**	**7**	**287**
Inorganic standards					
Calcite	3.0	0.2	70	5	20
Aragonite	4.8	0.8	106	9	57
Dolomite	7.3	0.1	111	9	20
Magnesite	9.2	0.9	145	10	20
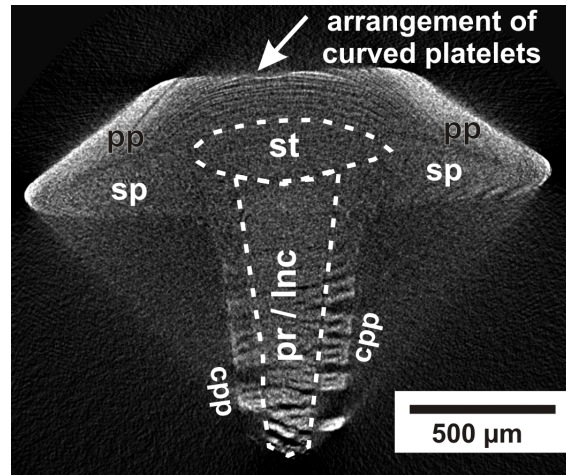
Figure 3.18: Computed nano-tomography image of a vertical section through the tooth. The stone is embedded in the structure of the tooth and is encased by the primary plates (pp), the secondary plates (sp) and the prisms - lamellar needle complex (pr/lnc) units. Note the well visible curved arrangement of the platelets of the primary plates.

and the mature parts of the tooth to the younger, proximal parts of the tooth. For the coronal cut the maps 1-4 cover different structural units at the tip, while map 5, 6, and 7 all cover the keel. Here we do not observe a clear trend in hardness and E-modulus.

Figure 3.19 shows nanoindentation results that were measured on a sagittal cut through the tooth and the adjacent jaw. The jaw yields an average hardness of 4.6 GPa and a Young's modulus of 78.6 GPa. The difference in mean hardness and Young's modulus between these two maps conducted on the jaw is attributed to occasional flawed indentation results due to the porosity in the jaw material. The nanoindentation maps that were conducted on the tooth itself comprise the primary plates, the stone, the needles/prisms and the carinar process plates. In general, the hardness and Young's modulus decreases from the tip of the tooth towards the plumula.

Figure 3.20 shows in a coronal cut section through the tooth indentation results from the keel as well as from the frontal cutting edge of the tooth including the primary, the secondary plates, the stone and the prisms. The keel exhibits homogeneous hardness values between 5.2 and 5.3 GPa (Figure 3.20a, Table 3.11, maps 5 to 7). At the cutting edge of the tooth no valid indents were obtained for the stone and the prisms due to the varying surface topography, even within highly polished sections through these units.

SEM

Figure 3.21 shows SEM images taken from polished surfaces of the samples that were used for nanoindentation measurements. The two plates, the needles/prisms and the stone units of the tooth of Paracentrotus lividus are well distinguishable from each due to their specific microstructure (Figure 3.21). Even though the major
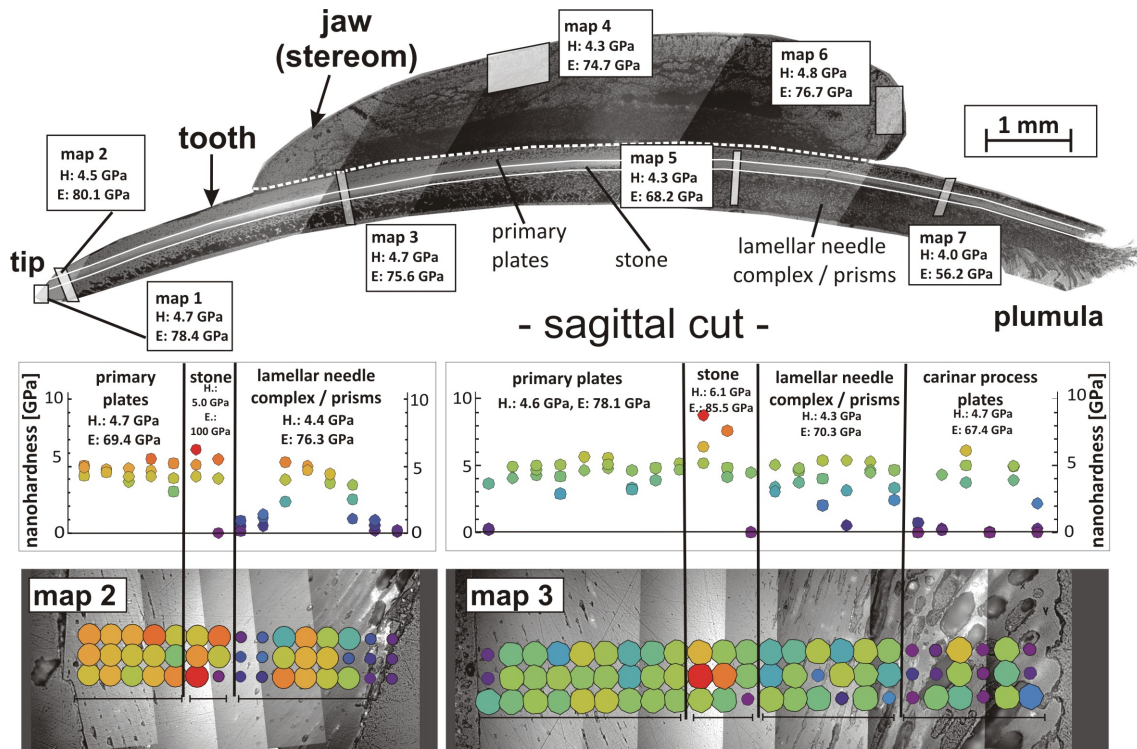
Figure 3.19: Maps 1 to 7 present nanoindentation results of a sagittally sectioned sea urchin tooth and jaw. The specific map positions are indicated on the tooth structure. Mean values for nanohardness and Young's modulus are also given for each particular map. A detailed presentation of the hardness and Young's modulus distribution patterns is illustrated in the two nanoindentation versus distance maps (map 2 and map 3) shown in the lower part of the figure. The indents are colour coded: red denotes a high hardness and blue to purple colours indicate a low hardness. In both maps it is well observable that the stone is the hardest part of the entire tooth structure. It is significantly harder than the plates and the prismatic tooth regions. The primary plates exhibit a slightly higher hardness in comparison to that of the needles/prisms.
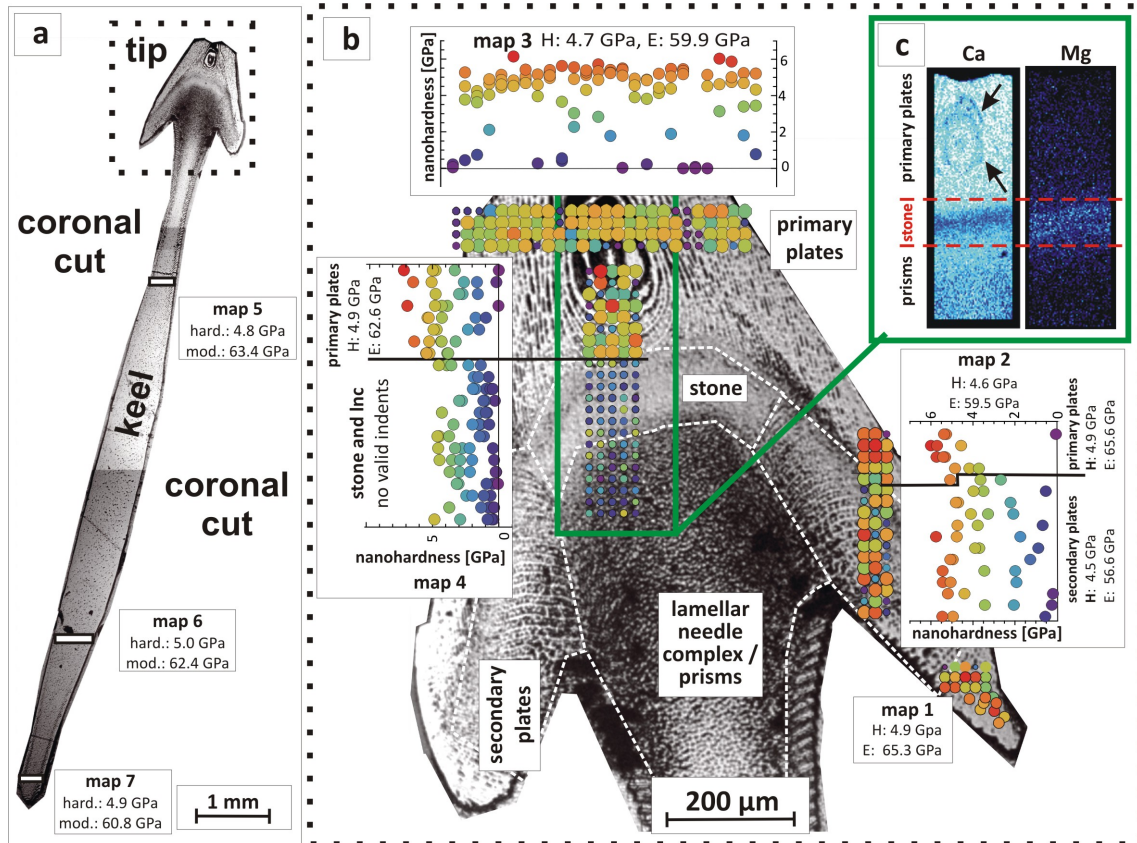
Figure 3.20: Nanoindentation maps are shown for a coronal cut of a sea urchin tooth. Maps 5, 6 and 7 (Figure 3.20a) present nanohardness and Young's modulus results from the keel. Nanoindentation maps 1 - 4 show the nanohardness distribution pattern at the tip of the tooth. Nanohardness values are given colour coded: red denotes a high hardness and blue to purple colours indicate a low hardness. In Figure 3.20c a portion of the tooth is given that has been scanned with EDX. Well observable is the high Mg content of the stone in comparison to the neighbouring major structural units: the needles/prisms and the primary plates.
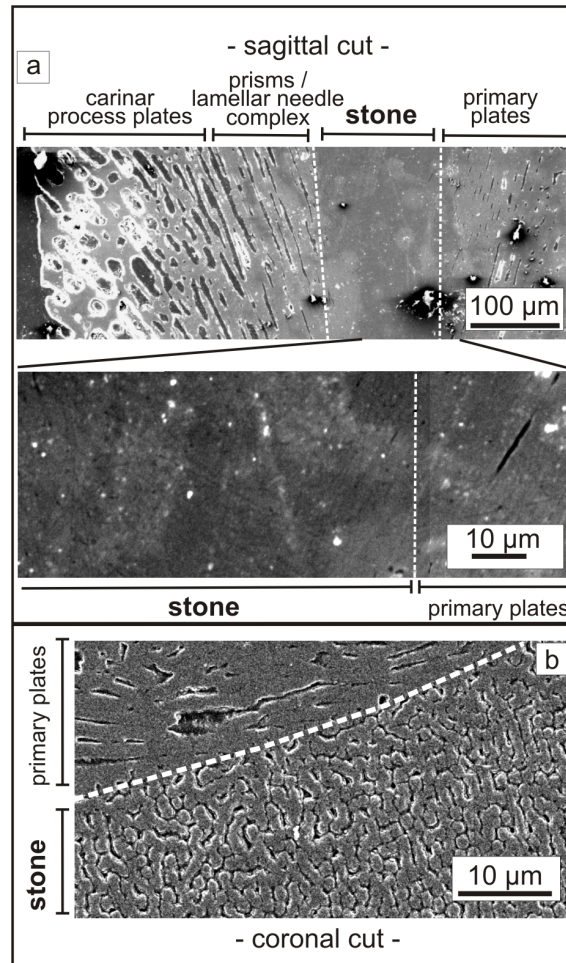
Figure 3.21: SEM image (SE contrast) of a sagittal (3.21a) and a coronal cut section (3.21b) of the sea urchin tooth. Well observable is the difference in surface topography of the stone between the two differently sectioned samples: smooth in the sagittal section (3.21a) and with a pronounced topography in the coronal sectioned sample (3.21b).

structural units (primary plates, prisms, carinar process plates and stone) are well distinguishable from each other, in the sagittal cut the stone has a uniformly flat surface (Figure 3.21a) while in the coronal cut (Figure 3.21b) a pronounced surface topography emerges for the stone. The lateral length-scale of the topography is in the order of a few micrometres and thus it is in the lateral size range of a nanoindent. This led to invalid indents.

Electron Microprobe and EDX analyses

Figure 3.22 shows two characteristic examples of element distribution maps from the sagittally sectioned sea urchin tooth. In addition to calcium we also measured sodium and magnesium. Iron and potassium were sought after but remained below the detection limit. The magnesium distribution pattern is structured within the tooth, it is not homogeneous even within one specific structural unit. On the basis

of major element concentration maps we can distinguish well between the primary plates the needles/prisms and the stone (Table 3.12). Magnesium concentrations in the stone are highest and occasionally reach to 5.2 wt-%. Most measured points in the stone contain between 2.5 and 3.6 wt-% magnesium, the primary plates and the prisms contain in average only 1-2 wt-% magnesium. Small domains of elevated magnesium concentrations can be observed in the carinar process plates (cf. Table 3.12). The observed sodium content is statistically distributed within the tooth and is on average 0.34 ± 0.2 wt-%, with peak values of up to 1 wt-% sodium.

Our most important observation is the fact that the sum of Ca-, Mg-, and Na-carbonate in the primary plates and notably in the stone is significantly lower than 100% (Figure 3.22 and Table 3.12). We attribute this deficit in the EPMA to the presence of a significant content of organic polymers in the stone and in the needles/prisms unit. To deduce the magnesium content of the calcite it is thus necessary to calculate the Mg/Ca ratio. We observe a molar Mg/Ca ratio of 10% in the primary plates, 24.9% in the stone, 11.9% for the needles/prisms and 12.2% in the carinar process plates. In areas of high Mg content within the carinar process plates we observe a molar Ca/Mg ratio of 26%.

Inorganic calcite was also analysed as a reference. It contained 0.2 wt-% of magnesium (molar Ca/Mg ratio of 0.82%). Sodium in inorganic calcite was under the detection limit. Major element analyses from the coronal cut of the tooth (Figure 3.20) show similar major element distribution patterns to those obtained from the sagittaly cut sample. In this cut also Mg and Ca are anti-correlated, with Mg contents in the stone region being significantly higher in comparison to Mg concentrations within the primary plates and the carinar process plates (Table 3.12).

EBSD

Several EBSD maps were measured along the entire length of a sea urchin tooth, representative EBSD results are shown in Figure 3.23 to 3.27. Maps where a more detailed analysis is merited are shown in Figures 3.24, 3.25, and 3.26. As a general result it can be said that a coherent crystallographic orientation pattern is kept along the tooth in a way that the **c**- and the **a***-axis (parallel to the [210] direction in the hexagonal setting) form the sagittal mirror plane of the tooth. A constant angle of 56° ($\pm$ 3°) occurs between the radius of the tooth curvature and calcite c-axis direction ($< 001 >$, Figure 3.23). Thus, the crystallographic orientation of the calcite rotates in this structure also with the curvature of the skeletal element, as we showed already for brachiopod shells (Goetz et al. 2009, Griesshaber et al. 2007, Schmahl et al. 2004).

The good angular and high lateral resolutions of EBSD analyses allow to map the mosaicity of the crystallographic arrangement between and inside the major structural units of the tooth accurately. In the maps presented in Figures 3.23-3.26 the colours code for orientation: the three Euler angles obtained for the crystal orientation code for the three coordinates of RGB colours, and the covered angular range is given in each map. In Figure 3.23 map 2 a cross section is shown that covers the primary plates, the stone and the carinar process plates. A careful inspection of the EBSD data reveals that within the stone platelets of the pp and the sp interdigitate. The individual platelets exhibit a slight tilt to each other.
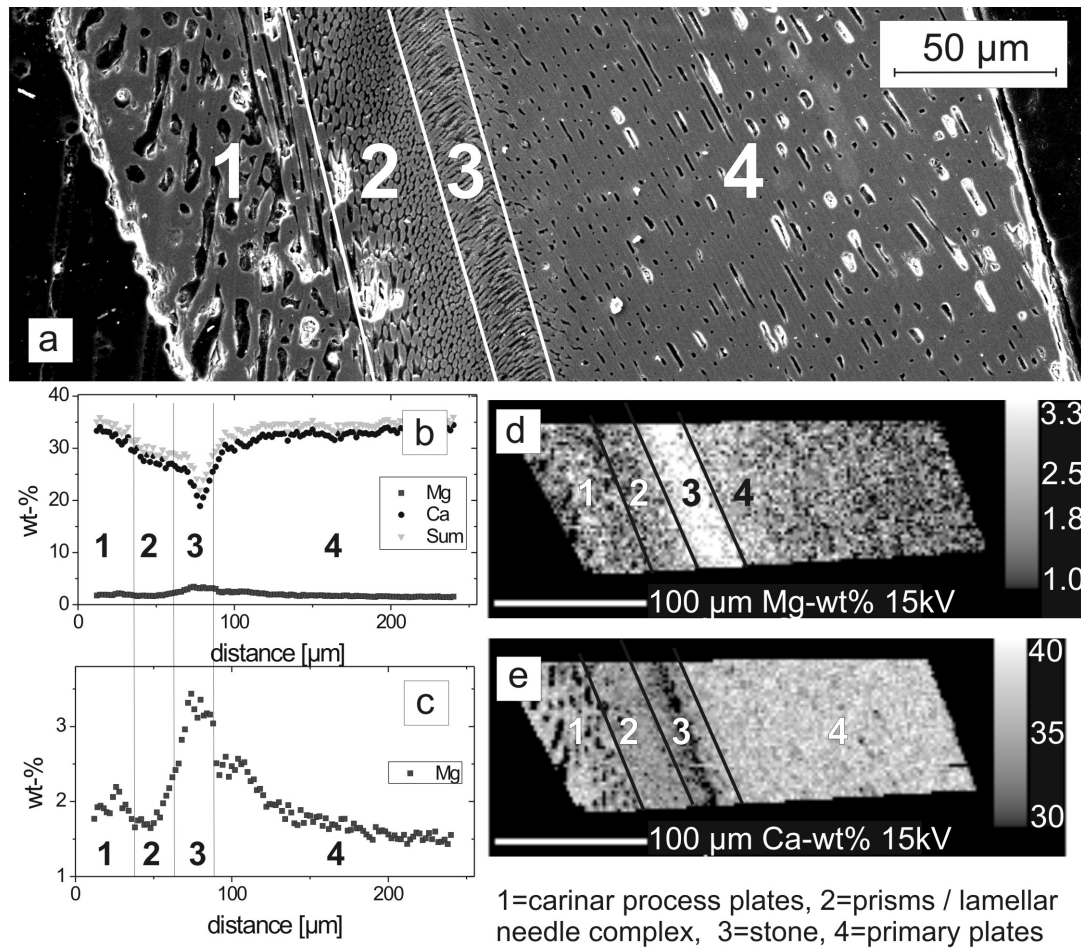
Figure 3.22: Distinction between the different major structural units of the sea urchin tooth: specific microstructural features of the distinct elements (3.22a), Mg, Ca and total element content distribution patterns determined determined with EPMA (3.22b to 3.22e). The tooth can well be differentiated (microstructurally as well as chemically) into the carinar process plates, the prisms, the stone and primary plates. The total sum of observed elements is changing along the chosen EPMA profile and indicates a concentration variation of included organic polymers.

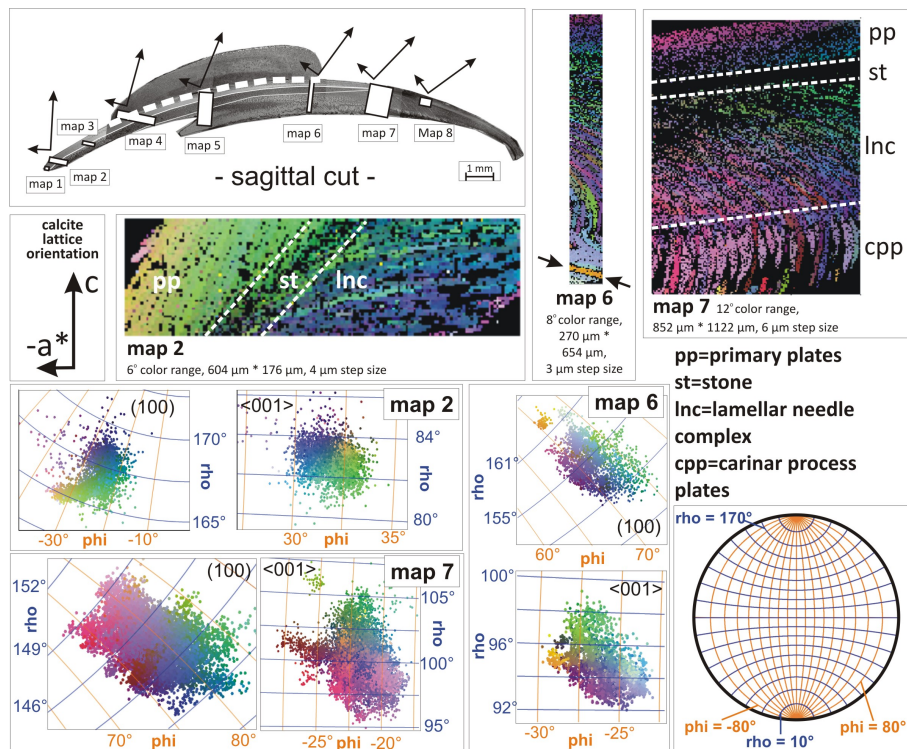Figure 3.23: EBSD results are shown for the sagittal section of the sea urchin tooth. The positions of the EBSD maps 1 to 8 are given on the optical image of the tooth. Maps 2, 6 and 7 display in great detail textural features not only from distinct major structural units of the tooth (such as the primary plates (pp), lamellar needle complex (lnc), carinar process plates (cpp) and the stone (st)) but also the orientational arrangement of individual major structural units relative to each other. The set of arrows on the optical image of the jaw and the tooth highlights the variation of **c**- and **a***-axes orientation patterns and visualizes the rotation of the **c**-axes with the curvature of the tooth arc. EBSD datasets (maps 2, 6 and 7) are represented colour coded. Black points denote those regions within the tooth where Kikuchi patterns could not be indexed. The three RGB colour components code for the three Euler angles of crystal orientation. In order to visualize small crystal orientation variations, colour coding applies to a limited range of the Euler angles. The used colour range is given below every EBSD map together with the size of the image and the used electron beam step size. The colour scales that were used to indicate orientation variations are given for each map in cut-out portions of the Wulff's net. While the crystallographic orientation of the major structural units of the tooth are tilted relative to each other by 3 to 5°. Within each structural unit the subunits are tilted relative to each other by only 1 to 2°. Occasional exceptions occur, such as shown by the orange platelet in the lower section of map 6 (indicated by arrows), where the misorientation of this platelet to neighbouring platelets is 5°.

103

Table 3.12: Element concentrations of exemplary EPMA point analyses obtained from major structural units of the tooth. Carinar plates I has a composition close to the average composition of the carinar plates, while carinar plates II is in a high Mg domain within the carinar plates. For comparison major element data obtained on inorganic calcite is also shown. The difference to 100% is attributed to be caused by the contribution of organic matter within the tooth.

	Ca [wt.-%]	Mg [wt.-%]	Na [wt.-%]	CO$_3$ [wt.-%] (calculated)	Sum [wt.-%]	Mg/Ca molar ratio	Na/Ca molar ratio
Primary plates	31.2	1.9	0.3	51.8	85.2	10 %	2 %
Stone	23.8	3.6	0.3	45.0	72.7	25 %	2 %
Needles / prisms	31.8	2.3	0.5	54.2	88.8	12 %	3 %
Carinar process plates I	35.1	2.6	0.3	59.3	97.3	12 %	2 %
Carinar process plates II	29.7	4.7	0.1	57.8	92.3	26 %	1 %
Inorganic calcite	38.1	0.2	<0.01	60.5	98.8	1 %	0 %

The lower parts of maps 6 and 7 (Figure 3.23) cover the curved carinar process plates of the keel, where we see misorientations of up to 5° from one plate to the next. Map 4 (location indicated in Figure 3.23) is analysed in more detail in Figure 3.24. This map covers a part of the jaw, followed by primary plates, the stone, the prism region adjacent to the stone the carinar process plates. The stereographic projection covering the complete hemisphere shows that the jaw and the tooth have quite different crystallographic orientations, differing by a 50° rotation around [$\bar{1}$20]. In the higher-resolved parts of the stereographic projection we see that the distribution of the crystallographic orientation of the tooth material in this map forms three clusters, one corresponding to the primary plates, another to the prism region, and a third to the stone. Superimposed to the orientation of the stone are the orientations of the carinar process plates (both, the cpp and the pp in the stone region have the same colour). The orientation changes gradually within each major structural unit. This gradual change corresponds to the overall rotation of the lattice following the curvature of the tooth, as it is indicated in Figure 3.23. With respect to crystallography this rotation is around the **b**-axis, i.e. perpendicular to the **c**-axis and the **a***-axis. Map 5, displayed in Figure 3.25, covers a cross-section that extends from the primary plates over the stone, the adjacent prism region to the carinar process plates, the latter show their characteristic morphological curvature. Apart from the clustering of orientational data indicating the crystallographic misorientation between the different major structural units, we also see very clearly how the concave/convex carinar process plates show the gradual orientational change from

left to right in the picture (Figure 3.25), again corresponding to the overall rotation of the crystallographic orientation following the curvature of the tooth. For easier comparison, we numbered the platelets from left to right (Figure 3.25). Note also, that going from plate to plate the orientational change is not uniform, but it is oscillating forward and backward, which can be seen by comparing the position in the pole figure for plates with even and odd numbers. The lattice orientation from platelet to platelet changes by $\pm$ 1 to 2°, and across the whole map the lattice rotation amounts to about 5°.

Figure 3.26 displays two EBSD maps of key areas of the tooth which were investigated with higher lateral resolution in comparison to the other EBSD maps: the tip (map 1), and the stone in a part of the tooth close to the tip but where no grinding and chipping action has taken place (map 3). Within this small map the individual plates keep their crystallographic orientation (pp in greenish and sp in bluish colours). Note the thin lines coloured in blue (like the sp) streaking out from the right and the material displayed in green (colour like the pp) between them. The blue lines, which are likely to be sections through plates with a thickness of 3-5 micrometres, directly join in the centre of the stone with one primary plate each. Note that both types of plates are slightly curved and at their join they form an angle of about 47° (due to the curvature of the plates and the fact that the observed angle will depend on the angle of the plane of the section with the plates, the angle cannot be determined rigorously). Map 3 in Figure 3.26 covers the primary plates, the carinar process plates, and the stone with the adjacent needles/prisms unit. In the stone we see again an interdigitation of two materials with slightly different crystallographic orientation. While the primary plates show an almost uniform orientation (pinkish colours), the material intercalated between the primary plates differs in orientation by about 3-6°. The material between the plates in the stone has a patchy appearance in the EBSD maps, we interpret the patches as intersections of the needles (fibres, prisms) of the stone with the polished surface.

In Figure 3.27 we present the experimental pole figures of selected sets of some crystallographic planes as determined by EBSD. The directions of some plane normals are shown as arrows in the map of Figure 3.27. The crystallographic orientation at the tip is such that the traces of the primary plates in the plane of observation are perpendicular to the plane normal. As our section is located close to the centre of the tooth, the plates should be perpendicular to the plane of observation in this area. Thus, we conclude that here the primary plates are parallel to the ($\bar{1}$02) planes. Following the same line of argument, secondary plates in the central tooth material near the stone are (001) planes. Note that none of the 104s plane normals is a candidate for the normal to any of the plates in this tooth area. The crystallographic direction of the central line of the stone connecting the V-shaped intersections of plates is close to the [631] direction or the (205) plane normal.

3.6.5 Discussion

Chemical structuring of the tooth

The chemical structuring of sea urchin teeth into a casing material with moderate Mg-contents and the Mg-rich stone was subject of many studies (Stock et al. 2003b,

map 4 — 9°color range, 1252 μm * 256 μm, 4 μm step size

50 μm

jaw   pp   st   lnc   cpp

rho = 170°
<001> tooth
(100) Jaw
<001> jaw
(100) tooth
phi = -80°   phi = 80°
rho = 10°

<001>
pp   pp/st, cpp
170°
rho
165°   lnc
5°   10°   phi   15°   20°

(100)
pp   90°
pp/st, cpp   85°
rho
lnc   80°
90°   phi   95°

pp=primary plates, st=stone, lnc=lamellar needle complex, cpp=carinar process plates
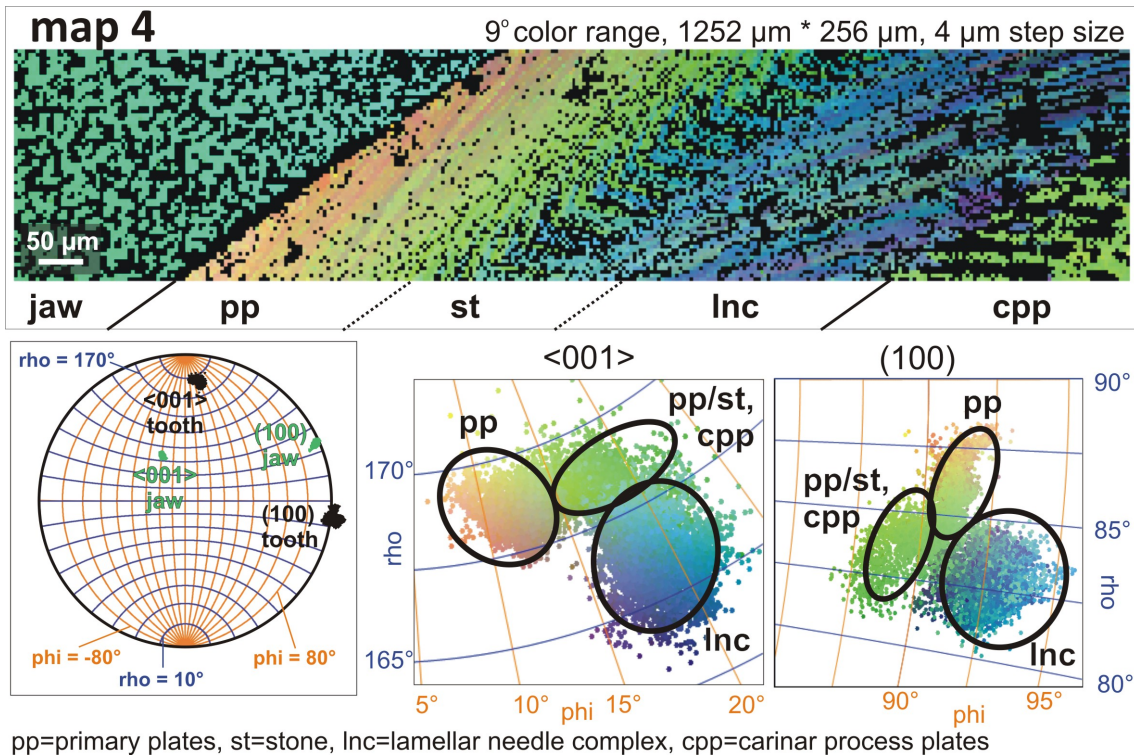
Figure 3.24: Map 4 shows EBSD results in high resolution for the jaw and the adjacent sea urchin tooth. The location of map 4 on the tooth is given in Figure 8. Crystallographic orientation is different for the jaw, the primary plates (pp), the stone (st), the lamellar needle complex (lnc) and the carinar process plates (cpp). Well visible are the two orientations within the primary plates: (a) orange to red at the outermost margin of the primary plates and (b) light green at the intersection with the stone. Note the interdigitating microstructure of the primary plates (light green) and the prisms (blue) within the stone part of the tooth. The carinar process plates (cpp, light green) have a similar orientation pattern to that of the primary plates. Below map 4 orientational patterns of the major structural units are shown in stereographic projections: (a) in a complete stereographic projection (left diagram) and (b) in selected areas of the stereographic projection (central and right diagram). We observe a tilt of 50° around the [-120]-axis between the jaw and the tooth. Furthermore, two orientations are present within the primary plates: (a) one orientation indicated by pink to orange colours (pp) and (b) another orientation indicated in light green (pp/st) where the orientation of the stone, a portion of the primary plates and the carinar process plates is similar.

pp = primary plates, st = stone, lnc = lamellar needle complex,
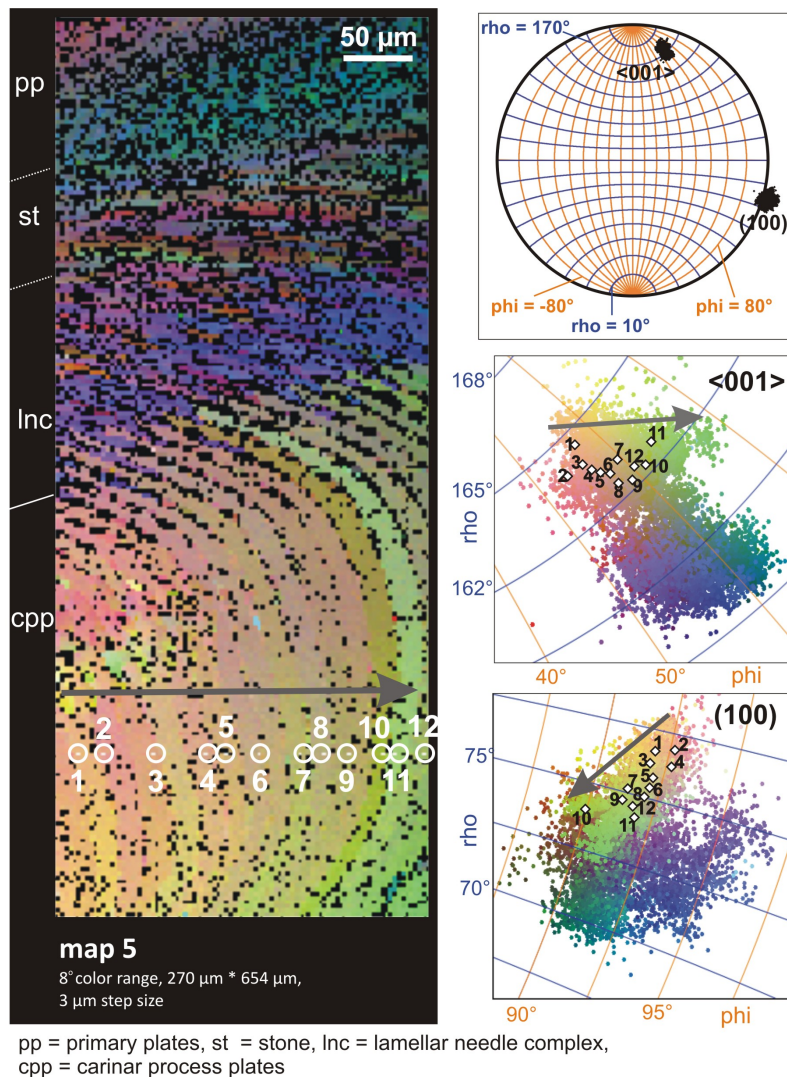cpp = carinar process plates

Figure 3.25: Map 5 and the stereographic projections highlight crystallographic orientation differences between the primary plates (pp), the stone (st), the lamellar needle complex (lnc) and the carinar process plates (cpp). The complete upper hemisphere of the stereographic projection with the **c**- and **a***-axis orientation of the entire map, while the central and the lowermost projections are portions of the complete stereographic projection. Individual platelets of the cpp tooth unit (numbered in the map and in the sections of the stereographic projection) are tilted relative to each other by 1 to 2 degrees, while the tilt of major structural units relative to each other is up to 5 degrees. Note the oscillating misorientation between adjacent platelets within the cpp unit.
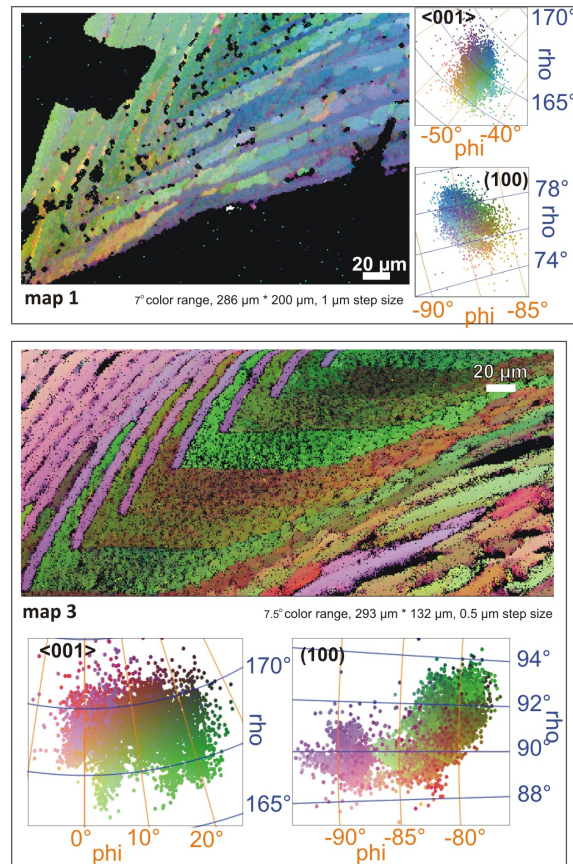
Figure 3.26: EBSD maps 1 and 3 show in high resolution crystallographic orientation patterns of the tooth at the tooth tip (map 1) and from a section very close to the tip (map3). The location of both maps is given in Figure 3.23. Orientation differences are shown colour coded in both, the maps as well as in sections of a stereographic projection. The very tip of the tooth consists of closely oriented primary plates and plates in the lamellar needle complex which are intercalated with the composite of calcite fibres embedded in a high Mg-calcite matrix. This composite gives micrometer-sized patches of uniform orientation (colour) in the EBSD pattern. As the similarity of the colours shows (green: pp and blue: sp), the difference in tilt between these two units here is very small, up to 0.5 degrees. The misorientation between the fibre composite and the secondary plates is up to 1 degree, while the the patches of the composite are misoriented against each other by 0.5 to 1 degrees. Orientational differences between major structural units become more distinct away from the very tip of the tooth (map 3). Well distinguishable is the difference in orientation between the primary plates and the fibre composite in the stone and the lamellar needle complex.
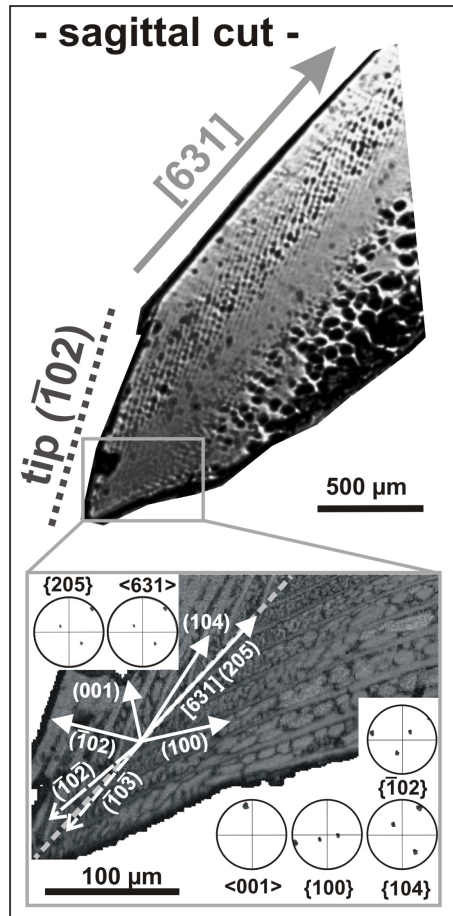
Figure 3.27: Specific microstructural arrangement with respect to crystallographic orientation at the cutting edge of the tooth, (a) reflected light micrograph, (b) magnification of the tip area displayed as EBSD band contrast map. The solid arrows show the (100) and (100) plane normals (i.e. the c* and a* directions) of the composite crystal together with plane normals and directions relevant to the morphology. The corresponding experimentally determined pole figures are also displayed as upper hemisphere stereographic projections. The mirror plane of the tooth is thus the **c*-a*** plane of the composite crystal. In this central section of the tooth tip, the primary plates form the upper outer boundary of the sharpened tooth tip and they are perpendicular to the $(\bar{1}02)$ plane normal. The plates in the lnc (lower part of the EBSD map) form the lower outer boundary of the tooth tip and they are perpendicular to the (001) plane normal. The line connecting the V-shaped intersections of the plates in the centre of the stone is parallel to the [631] direction. This direction is also the growth direction of the tooth, it forms the tangent to the arc of the tooth not just at the tip but everywhere along the tooth (grey arrow in (a), see also Figure 3.23). The direction [631] is almost parallel to the (205) plane normal. The thin dashed lines show the negative (102) and (103) plane normal directions which bracket the (205) orientation. The normal to the (104) cleavage plane of calcite and the 104 pole figure are shown to indicate that 104 cleavage is not relevant in the morphology and self-sharpening mechanism of the tooth tip.

Wang et al. 1997, Weber 1969, Weber 1973). In more recent work Killian et al. (2009) and Ma et al. (2009) applied X-ray photoelectron emission spectromicroscopy (X-PEEM) and Nano-SIMS (Ma et al. 2009) to differentiate chemical structuring of the stone on length scales of tens of nanometres, and they were able to demonstrate that the fibre composite structure constituted of fibres with moderate Mg-content ($\sim$ 12 mol-%) lodging in a matrix of extremely high-Mg-calcite ("protodolomite", 45 mol-% Mg). The fibres are formed in a first stage of mineralisation while the matrix particles form as a second-stage mineralisation.

Chemical analyses in our study were performed with a considerably lower lateral resolution (spot size was 5 μm) and were aimed to correlate our EBSD and hardness study with the major structural units as were described in previous papers (Killian et al. 2009, Ma et al. 2007, Ma et al. 2009, Robach et al. 2009, Wang et al. 1997). We find a good agreement between the results presented in this study and the results obtained by Wang et al. (1997): primary plates composition presented by (Wang et al. 1997) is around 8.5 mol-% $MgCO_3$ (it is 10 mol-% $MgCO_3$ in the present study) and the average composition of the stone is 24 mol-% $MgCO_3$ (it is 24.9 mol-% $MgCO_3$ in the present study). Our most important new finding, however, is that the measured Mg-, Ca- and Na-contents together with a corresponding amount of carbonate (CO_3^{2-}) add up to only 75 wt-% of the material for the stone (while we obtain 99% for the calcite standard). Hence we conclude that units must be present in the tooth which are non-detectable by EPMA. The most likely candidate material is organic matrix (or pores). Indeed, Wang et al. (1997) demonstrated the presence of organic matrix in the form of sheets separating the calcite fibres from the matrix crystals. The surface topography indicating the presence of pores can be seen in the coronal section of the stone in Figure 3.21b. Our surface preparation procedure removes organic matrix unless it is chemically fixed, which would explain the pores. In their synchrotron x-ray microtomography study Stock et al. (2003b) describe a "low absorption zone" in the centre of the tooth, which clearly corresponds to the centre of the stone. Excluding that the effect is due to the Mg/Ca ratio they conclude that "soft tissue", i.e. organic matrix, must be present. Secondary ion mass spectroscopy data (Robach et al. 2006) revealed an increased content of aspartic acid within the stone. The 25 wt % unaccounted mass in our EPMA analyses, however, should not be taken as a direct measure for the amount of organics due to systematic errors in the PAP correction if unaccounted material is present. Nevertheless, our data indicate that the organic content of the stone must be substantial. The presence of organic matter in biominerals is usually contributing significantly to the strength and notably to the toughness of the biomaterial. Our observation of increased nanohardness of low-Mg-biocalcite of brachiopods compared to inorganic calcite can only be attributed to the strengthening effect of the intra- and intercrystalline organic material in the calcite observed by TEM (Griesshaber et al. 2009, Merkel et al. 2009, Schmahl et al. 2008). For nacre the strengthening effect of the organic/inorganic composite structure compared to the pure brittle mineral has been subject of many studies (Barthelat and Espinosa 2007, Barthelat et al. 2007, Currey 1977, Wang et al. 2001).

In our EPMA data we found a low concentration of sodium within all structural elements of the tooth. This observation was also made by Moureaux et al. (2010) in sea urchin spines.

As the polishing preparation of the specimens was made with constant water exchange, we do not assume that any residual sodium chloride from sea water was left in the tooth. Furthermore, we did not observe any sodium in inorganic calcites that experienced the same sample preparation as that applied to the sea urchin teeth. We assume that sodium is located within the mineral phase, especially as there is no positive correlation between sodium content and presumed organic matter content (mass deficit). We attribute the sodium content in biocalcite to be inherited from the ACC precursor.

Nanohardness from Indentation

Vickers microhardness testing (Hozman 1983, Märkel and Gorny 1973, Wang et al. 1997) already showed the basic principles of the hardness distribution in sea urchin teeth, with the hard stone material encased in softer platy material. While we obtained the same pattern of relative hardness distribution in the tooth, our hardness values are significantly higher than those of a recent nanoindentation study by Ma et al. (2008) that was performed on teeth of the same species. However, the values obtained for Young's moduli appear to be comparable in both studies. We attribute the discrepancy in absolute hardness to the depth of nanoindentation used. Ma et al. (2008) applied an indentation depth of 75 nm using the same CSM indentation head as we did. The shallow indentation depth was chosen by the authors deliberately in order to achieve the highest possible lateral resolution for the discrimination between the ultra-high Mg matrix particles of the stone and the embedded fibres. We indented 300 nm deep and used only the data from 100-300 nm for the calculation of the hardness at each indentation, the hardness of the CSM algorithm does not converge as a function of depth below 100 nm. Since typical Berkovich indenters have a radius of curvature in the order of 50 nm at the tip (personal communication G. Pharr, Bei et al. 2005), for such shallow depths the indentation is somewhere between a spherical and the triangular pyramidal Berkovich geometry, while the latter must have been assumed in the evaluation algorithm.

Even though we probed into deeper levels, we observe a higher absolute hardness of the material in comparison to that found by Ma et al. (2008), an observation that is in contrast to what we would expect from an indentation size effect (Demir et al. 2009). Thus, it may well be that there is an additional effect related to the preparation of the indentation surface, as cutting and polishing creates a plastically deformed zone, which we remove by a final etch-polishing treatment (as required in particular for EBSD).

Micro- and nanostructural properties: The sea urchin tooth as a hierarchical composite crystal

a) The hierarchical composite structure
The tooth of *Paracentrotus lividus* shows a hierarchical architecture. On the sub-

millimetre scale we distinguished, following the previous literature, 5 major structural units which run in parallel along the length of the tooth: the primary plates, the secondary plates, the carinar process plates, the stone and the needles/prisms. Each of these units has a distinct internal microstructure. The plates encase the fibre-composite core of the tooth. The fibres of the composite forming this core change their diameter along their length (Wang et al. 1997). They have been called prisms at their thicker end at the base of the keel, while the term needles was used for fibres near their thinner end, which is located in the stone. Killian et al. (2009) used X-PEEM to demonstrate how the thin needles are intercalated with particles of high-magnesium calcite in the stone, while this particle matrix is not (or less) present at the thicker end of the fibres (the prisms). The "lamellar needle complex" is the transitional region between the stone and the prisms major structural units. We find it hard to clearly define any boundary between the needles/prisms, the secondary plates, and the carinar process plates. Neither is there any sharp boundary between the stone and the needles/prisms complex. Individual primary plates can be clearly discerned, they also intercalate with the fibres and the matrix of the stone. Thus, there are no real boundaries between the major structural units.

The assembly forms a hierarchical composite crystal. The parts of this object show a high 3-dimensional crystallographic orientational coherence with small misorientation of the discernable building units. In terms of classical crystallography the assembly may be termed a mosaic crystal, but in the composite crystal the mosaicity is not simply random but highly structured. Each of the slightly differently oriented major structural units is in turn a composite crystal on its own, consisting of micro- to nanoscale crystalline subunits of similar orientation.

Our EBSD data clearly show that calcite c-axis orientation rotates with the curvature of the tooth (Figure 3.23). With the exception of the very tip of the tooth a constant angle of 56° between calcite c-axis orientation and the tangent to the tooth arc is kept.

The self-sharpening of the tooth occurs with the chipping-off of plates at the tip of the tooth (Figs. 3.26 and 3.27). Consequently the tooth surfaces at the tip represent the V-shaped arrangement of the plates. Ma et al. (2009) investigated crystallographic orientation at the tooth tip with micro-XRD. Our results on the tooth tip are consistent with theirs, while our higher lateral resolution with EBSD provides more detailed information. Ma et al. (2009) report "two blocks" of "cooriented plates, needles, and polycrystalline matrix", which are interdigitated and which show slightly different lattice orientations. Their Figure 5 (a drawing) suggests that the "two blocks" are parallel plates corresponding to two different orientations of the primary plates in this area. Our EBSD study clearly shows that the primary plates all have similar lattice orientation (with a smooth gradual change corresponding to the curvature of the tooth), and that the second lattice orientation is given by the composite which intercalates between the plates, and which consists of needles and fine grained high-Mg matrix.

Their intercalated plate-shaped blocks correspond to either the upper half or the lower half of the stone. We see that two lattice orientations join in a V-shaped manner in the centre of the stone and that they are interdigitating (Figure 3.26).

With respect to the absolute crystallographic orientation of the tooth, the results are also consistent. In their drawing (their Figure 5A) Ma et al. (2009) place their (001) (= **c***) and (010) (= **b***) reciprocal space directions in the plane of observation (corresponding to the plane of our "sagittal section"), while we use the symmetry-equivalent **c*-a*** setting for these directions in this plane. The normal to the plane of observation, which is also the mirror plane of the tooth, in our setting is thus the vector product **c*** × **a*** = [010](the b axis). In their case it is the a axis [100]. Their conclusion that "cleavage planes (0$\bar{1}$4) ... are terminating the plate edges near the grinding surface" is approximately consistent with our observation (see the (104) plane normal in Figure 3.27, which is almost but not exactly parallel to the long axis of the tooth). However, with our better lateral resolution we see that the grinding "edge" does not exhibit any signs of (104) cleavage. The V-shaped blade at the tip is formed by the primary plates (which are parallel to the ($\bar{1}$02) plane) and the second type of plates intercalated in the lamellar needle complex (which are parallel to the (001) plane). The line of intersection of these two planes is [010]. These sets of crystallographic indices for morphological planes/directions apply only in the central section (the mirror plane) of the tooth: as the primary and secondary plates are curved (our Figures 3.17e, 3.19b, and Kniprath 1974, Märkel 1969, Märkel 1990, Märkel and Gorny 1973, Märkel et al. 1977, Stock et al. 2003b) they assume continuously changing crystallographic orientation towards the margin of the tooth. The cutting tip of the tooth is thus also of a rounded shape rather than displaying a true edge. The needle/matrix composite between the plates has its own orientation differing slightly from that of the plates between which it is intercalated.

b) Scenario of crystallisation

The current well supported paradigm of the exquisite control on the morphology of minerals excreted by organisms is the deposition of an amorphous precursor of the biomineral in an organic matrix which compartmentalises space (Addadi et al. 2003, Goetz et al. 2011). The subsequent crystallization of the ACC in the compartments lets the mineral inherit the morphology defined by the organic matrix. The ACC is likely to be produced in vesicles inside the cells of the mineralizing epithelium. The ACC nanoparticle freight of the vesicles must be exocytosed and attached to the growing skeletal element. Thus, the growth proceeds by attachment of nanoparticles which may still carry remnants of lipid membranes of the vesicles on their outside or collect other biomolecules on their surfaces before or as they are attached to the skeletal element (Goetz et al. 2011). In the subsequent crystallization process the organics within the amorphous precursor affect the precision of the crystallographic coherence. This leads to a mesoscale structure in the crystal with scatter of the 3D orientational crystallographic correlation between the constituting nanoparticles. Such crystals have recently been termed mesocrystals (Cölfen and Antonietti 2005, Meldrum and Cölfen 2008). Mesocrystalline structures are thus frequently observed in biologic materials and biomimetic synthetic objects (Cölfen and Antonietti 2005, Meldrum and Cölfen 2008, Vielzeuf et al. 2010). In low-resolution experiments such as standard polarized light microscopy (e.g. Wang et al. 1997) or standard x-ray diffraction (e.g. (Magdans and Gies 2004) these mesocrystalline aggregates appear as single crystals. As the sea urchin tooth forms from an ACC

precursor (Wang et al. 1997) it is likely to be mesocrystalline on the nanoscale such as other biocalcites formed from ACC (Griesshaber et al. 2009). The full tooth however, does not simply show a randomly scattering crystallite orientation (i.e. forming something like a Gaussian distribution around an average orientation), but it is a well-structured entity. This structuring can be explained by the presence of organic matrix membranes which block and guide the path of crystallization, such that some compartments in the matrix are connected (by "mineral bridges") and assume a similar crystallographic orientation, while others are reached by a crystallization front which has taken a different path and/or originates from a different nucleation site, and they thus assume a different orientation (Goetz et al. 2011). Although this scenario explains many if not all observations of mineral morphologies which are unusual in inorganic systems, it is still unclear how initial selection of crystallographic orientation of the nucleus does occur.

In the biogenic Ca-carbonates there is a continuous spectrum of crystallographic orientational correlation between the constituting crystallites, ranging from hierarchical composite single crystals (sharp 3D orientational correlation such as in the present case, see also Griesshaber et al. 2010), via uni-axial textures (with show a sharp correlation of one axis, usually [001], and a random distribution around this axis, such as observed e. g. in brachiopods (Goetz et al. 2007, Goetz et al. 2009, Griesshaber et al. 2007, Griesshaber et al. 2009, Schmahl et al. 2004, Schmahl et al. 2008), avian egg shells (Dalbeck and Cusack 2006) or the calcitic parts of bivalve skeletons (Hahn et al. 2011 manuscript in preparation)). Polycrystalline assemblages without orientational correlation are found in bioinduced mineralization (Section 3.1) and remain to be found in skeletons or teeth. A strong crystallographic alignment at different scale levels is an intrinsic feature of all biologically controlled mineral growth processes that we know of so far, not only of carbonate but also of phosphate biomaterials such as human teeth (Raue and Klein 2010).

Biomechanical features of sea urchin teeth

The sophisticated architecture of sea urchin teeth renders a brittle and relatively soft material such as calcite into a remarkably strong device with self-sharpening ability. The self-sharpening is obtained by encasing the hard and tough stone into a weaker, platy casing. Weak, non-mineralized zones between the plates outside the stone predefine the geometry of the chipping-off of the casing material in order to provide a pointed shape of the remaining stone core material. A pronounced difference between the elastic moduli of the stone material (average 93.4 GPa; a value of E = 98.5 GPa is reported for the ultra-high Mg matrix particles, Ma et al. 2008) and the casing plates (78 GPa and less) may also contribute to the chipping-off mechanism by generating differential strains under load at the interface between the stiffer and the more compliant material.

Keeled sea urchin teeth belong to the hardest calcitic biomaterials that were encountered so far. It has an average hardness between 5 and 6 GPa, maximum up to 8.8 GPa, and thus exceeds by far the hardness of calcite (3.0 GPa ± 0.7 GPa) and that of almost all non-biological carbonates with comparable composition (aragonite: 4.8 GPa ± 0.8 GPa, dolomite: 7.3 GPa ± 0.7 GPa). The organism uses a

number of nano- and microscale material design principles to modify the mineral structure compared to its mechanically unsuitable inorganic counterpart:

First, the formation of a hybrid (organic/inorganic) composite material is one of them. The mineral provides high elastic modulus and compressive strength, the organics provide tensile strength. The hybrid composite of both leads to bending strength and most importantly it reduces the risk of brittle fracture: the organics impede fracture propagation, i.e. they provide toughness and a degree of ductility if the strength of the material is exceeded by the mechanical load. With the methods applied in this study we cannot resolve the specific distribution pattern of organic polymers (Griesshaber et al. 2009, Merkel et al. 2009, Schmahl et al. 2008) in the stone, they occur as occluded polymers (Robach et al. 2005) within the crystals in addition to polymer films around calcite crystals (Wang et al. 1997) or as scaffolds around larger crystalline domains.

The second principle is substitution strengthening. The high Mg concentration in the stone contributes significantly to the hardness and the high elastic modulus of the sea urchin tooth. High Mg concentrations in calcitic biomaterials are expected to lead to solid solution hardening (Magdans and Gies 2004, Märkel et al. 1986, Stock et al. 2003b, Wang et al., 1997), i.e. the inhibition of dislocation glide through pinning at stress fields around the substitutional point defects. From Table 1 it can be seen that the pure Mg-carbonate (magnesite) is very hard and stiff compared to calcite, thus, there is an additional effect which is simply related to the stronger and more covalent Mg-O-bond compared to the Ca-O bond (stronger ionic field strength of the smaller Mg^{2+} ion compared to the larger Ca^{2+}). In the stone we find an average of 26 mol-% Mg, while the platy casing carries 10-12 mol-% Mg. It may be a matter of metabolic economy to use Ca^{2+} as the main readily available chemical component in the organism, rather than to construct the whole tooth from Mg-carbonate.

The third principle is dispersion/precipitation hardening. The sophisticated composite crystal microstructure provides many subgrain boundaries, which stop dislocations from moving and which divert and split-up cracks, thus consuming their energy and avoiding critical stress concentrations at crack tips. In common engineering materials such as Al-alloys or Ni-based superalloys, the hardening is obtained by controlled precipitation of hard particles in a softer matrix by exsolution from a precursor. In the sea urchin tooth the precursor is ACC.

The fourth principle is the formation of a particle-reinforced fibre composite. The hybrid fibre-composite architecture essentially provides strength and fracture toughness, the particle reinforcement with nanocrystalline ultra-high Mg-calcite, like it is intended in engineering polymer composites, adds to the E-modulus and to the fracture toughness along the lines described already above in Figure 3.18, and it additionally increases the hardness and wear resistance, and metal-bonded diamond cutting tool materials.

3.6.6 Concluding Summary

1. The keeled sea urchin tooth is a hierarchical composite crystal. The material has a 3-dimensional orientational coherence close to that of a single crystal. In contrast

to a common mosaic crystal it is built of systematically arranged, slightly misoriented subunits, which in turn consist of crystallites in a hierarchical microstructure covering many length scales. The mechanical strength of the composite crystal exceeds well the strength of its simple, inorganically built equivalent.

2. There is a distinct pattern of hardness distribution within the tooth. This pattern can well be correlated to some major element variations within the teeth, to the distribution pattern of magnesium and calcium and to functional properties required for self-sharpening.

3. Like in most other carbonate biomaterials the crystallographic orientation rotates with the curvature of the entire tooth structure. The sagittal mirror plane of the tooth contains the [001] and [210] directions, corresponding to the (001) and (100) plane normals, respectively (i.e. the **c***- and the **a***- reciprocal space directions). The overall growth axis of the tooth corresponds approximately to the (205) plane normal or [631] direction.

4. Near the cutting edge of the tooth the wedge is formed by ($\bar{1}$02) and (001) planes as platy material chips off parallel to these crystallographic planes.

5. Even though the overall crystallographic orientation (texture) of a sea urchin tooth is close to that of a single crystal, high-resolution two dimensional EBSD analysis has revealed that the main structural units (primary plates, carinar process plates, stone and needles/prisms) show slightly different orientations, and each major unit is divided into subunits with slightly different orientation.

6. The structured material properties together with a chemical stratification and a distinct micro- and nanostructure are the key factors that effect the self-sharpening of the sea urchin tooth.

ACKNOWLEDGEMENTS

References

Addadi, L., Raz, S., Weiner, S. (2003): Taking advantage of disorder: Amorphous calcium carbonate and its roles in biomineralization. Advanced Materials, 15, 959-970.

Ameye, L., De Becker, G., Killian, C., Wilt, F., Kemps, R., Kuypers, S., Dubois, P. (2001): Proteins and saccharides of the sea urchin organic matrix of mineralization: Characterization and localization in the spine skeleton. Journal of Structural Biology, 134, 56-66.

Barthelat, F., Espinosa, H.D. (2007): An experimental investigation of deformation and fracture of nacre-mother of pearl. Experimental Mechanics, 47, 311-324.

Barthelat, F., Tang, H., Zavattieri, P.D., Li, C.M., Espinosa, H.D. (2007): On the mechanics of mother-of-pearl: A key feature in the material hierarchical structure. Journal of the Mechanics and Physics of Solids, 55, 306-337.

Bei, H., George, E.P., Hay, J.L., Pharr, G.M. (2005): Influence of Indenter Tip Geometry on Elastic Deformation during Nanoindentation. Physical Review. Letters, 95, 045501.

Cölfen, H., Antonietti, M. (2005): Mesocrystals: Inorganic superstructures made by highly parallel crystallization and controlled alignment. Angewandte Chemie International Edition, 44, 5576-5591.

Currey, J.D. (1977): Mechanical-Properties of Mother of Pearl in Tension. Proceedings of the Royal Society London B Biological Sciences, 196, 443- 463.

Currey, J.D., Nichols, D. (1967): Absence of Organic Phase in Echinoderm Calcite. Nature, 214, 81-67.

Dalbeck, P., Cusack, M. (2006): Crystallography (electron backscatter diffraction) and chemistry (electron probe microanalysis) of the avian eggshell. Crystal Growth and Design, 6, 2558-2562.

Demir, E., Raabe, D., Zaafarani, N., Zaefferer, S. (2009): Investigation of the indentation size effect through the measurement of the geometrically necessary dislocations beneath small indents of different depths using EBSD tomography. Acta Materialia, 57, 559-569.

Giesbrecht, W. (1880): Der feinere Bau der Seeigelzähne. Morphologisches Jahrbuch 6, 79-105.

Goetz, A., Griesshaber, E., Schmahl, W.W. (2010): An Easy Approach to Increase the Precision of EBSD Analyses - Examples from a Sea Urchin Calcite Study. Solid State Phenomena, 160, 229-234.

Goetz, A., Griesshaber, E., Schmahl, W.W., Lueter, C. (2007): Crystal orientation selection during growth of brachiopod shell calcite. Geochimica et Cosmochimica Acta, 71, A335-A335.

Goetz, A.J., Griesshaber, E., Neuser, R.D., Lüter, C., Hühner, M., Harper, E., Schmahl, W.W. (2009): Calcite morphology, texture and hardness in the distinct layers of rhynchonelliform brachiopod shells. European Journal of Minerlaogy, 21, 303-315.

Goetz, A.J., Steinmetz, D.R., Griesshaber, E., Zaefferer, S., Raabe, D., Kelm, K., Irsen, S., Sehrbrock, A., Schmahl, W.W. (2011): Interdigitating biocalcite dendrites form a 3-D jigsaw structure in brachiopod shells. Acta Biomaterialia, 7, 2237-2243.

Goetz, A.J., Ziegler, A., Kipry, J., Wagner, F. E., Wang, Z.L., Hsieh, K.Y., Park, S.H., Pentcheva, R., Wiacek, C., Schlömann, M., Janneck, E., Schmahl, W. W. (submitted): On the Structure and Formation of Biotic and Abiotic Schwertmannite. European Journal of Mineralogy.

Griesshaber, E., Neuser, R., Schmahl, W.W. (2010): The application of EBSD analyses to biomaterials, microstructural and crysallographic texture variations in marina carbonate shells. Semin. Soc. Esp. Mineral. 07, 22-34.

Griesshaber, E., Schmahl, W.W., Neuser, R., Pettke, T., Blum, M., Mutterlose, J., Brand, U. (2007): Crystallographic texture and microstructure of terebratulide brachiopod shell calcite: An optimized materials design with hierarchical architecture. American Mineralogist, 92, 722-734.

Griesshaber, E., Kelm, K., Sehrbrock, A., Mader, W., Mutterlose, J., Brand, U., Schmahl, W.W. (2009): Amorphous calcium carbonate in the shell material of the brachiopod Megerlia truncata. European Journal of Mineralogy, 21, 715-723.

Hahn, S., Rodolfo-Metalpa, R., Griesshaber, E., Schmahl, W.W., Buhl, D., Hall-Spencer, J., Baggini, C., Immenhauser, A. (2011 manuscript in preparation): Exploring marine bivalve geochemistry and shell ultrastructure from modern low pH environments as possible archives of past ocean acidification. Earth and Planetary Science Letters.

Holland, N.D. (1965): An Autoradiographic Investigation of Tooth Renewal in Purple Sea Urchin (*Strongylocentrotus Purpuratus*). Journal of Experimentally Zoology, 158, 275-281.

Hozman, P. (1983): Das unterschiedliche Härteverhalten biogener und anorganischer Calcitkristalle. Bochumer Geologische und Geotechnische Arbeiten. Inst. für Geologie d. Ruhr-Univ. Bochum, Bochum, Germany.

Killian, C.E., Metzler, R.A., Gong, Y.U.T., Olson, I.C., Aizenberg, J., Politi, Y., Wilt, F.H., Scholl, A., Young, A., Doran, A., Kunz, M., Tamura, N., Coppersmith, S.N., Gilbert, P.U.P.A. (2009): Mechanism of Calcite Co-Orientation in the Sea Urchin Tooth. Journal of the American Chemical Society, 131, 18404-18409.

Kniprath, E. (1974): Ultrastructure and Growth of Sea-Urchin Tooth. Calcified Tissue Research, 14, 211-228.

Ma, Y., Weiner, S., Addadi, L. (2007): Mineral deposition and crystal growth in the continuously forming teeth of sea urchins. Advanced Functional Materials, 17, 2693-2700.

Ma, Y., Cohen, S.R., Addadi, L., Weiner, S. (2008): Sea urchin tooth design: An "All-Calcite" polycrystalline reinforced fiber composite for grinding rocks. Advanced Materials, 20, 1555-1559.

Ma, Y.R., Aichmayer, B., Paris, O., Fratzl, P., Meibom, A., Metzler, R.A., Politi, Y., Addadi, L., Gilbert, P.U.P.A., Weiner, S. (2009): The grinding tip of the sea urchin tooth exhibits exquisite control over calcite crystal orientation and Mg distribution. Proceedings of the National Academy of Science, 106, 6048-6053.

Magdans, U., Gies, H. (2004): Single crystal structure analysis of sea urchin spine calcites: Systematic investigations of the Ca/Mg distribution as a function of habitat of the sea urchin and the sample location in the spine. European Journal of Mineralogy, 16, 261-268.

Märkel, K. (1969): Morphology of Sea-Urchin Teeth .2. Keeled Teeth of Echinacea (Echinodermata, Echinoidea). Zeitschrift zur Morphologie der Tiere, 66, 1-50.

Märkel, K. (1990): Biomineralisation in Echinoderms. In: Echinoderm Research. Edited by: De Ridder, C., Dubois, P.; CRC Press, Rotterdam, ISBN: 90-6191-141-9. Pages 277–282.

Märkel, K., Gorny, P. (1973): Functional Anatomy of Sea-Urchin Teeth (Echinodermata, Echinoidea). Zeitschrift zur Morphologie der Tiere, 75, 223-242.

Märkel, K., Gorny, P., Abraham, K. (1977): Microarchitecture of sea urchin teeth. Fortschritte der Zoologie, 24, 103-114.

Märkel, K., Röser, U., Mackenstedt, U., Klostermann, M. (1986): Ultrastructural Investigation of Matrix-Mediated Biomineralization in Echinoids (Echinodermata, Echinoida). Zoomorphology, 106, 232-243.

Meldrum, F.C., Cölfen, H. (2008): Controlling Mineral Morphologies and Structures in Biological and Synthetic Systems. Chemical Reviews, 108, 4332-4432.

Merkel, C., Deuschle, J., Griesshaber, E., Enders, S., Steinhauser, E., Hochleitner, R., Brand, U., Schmahl, W.W. (2009): Mechanical properties of modern calcite- (Mergerlia truncata) and phosphate-shelled brachiopods (Discradisca stella and Lingula anatina) determined by nanoindentation. Journal of Structural Biology, 168, 396-408.

Moureaux, C., Perez-Huerta, A., Compere, P., Zhu, W., Leloup, T., Cusack, M., Dubois, P. (2010): Structure, composition and mechanical relations to function in sea urchin spine. Journal of Structural Biology, 170, 41-49.

Paquette, J., Reeder, R.J. 1990: Single-Crystal X-Ray Structure Refinements of 2 Biogenic Magnesian Calcite Crystals. American Mineralogist, 75, 1151-1158.

Pouchou, J.L., Pichoir, F., 1984. A New Model for Quantitative X-Ray-Microanalysis –I Application to the Analysis of Homogeneous Samples. Recherche Aerospatiale, 3, 167-192.

Raue, L., Klein, H. (2010): Location depending textures of the human dental enamel. Solid State Phenomena, 160, 281-286.

Robach, J.S., Stock, S.R., Veis, A. (2005): Transmission electron microscopy characterization of macromolecular domain cavities and microstructure of single-crystal calcite tooth plates of the sea urchin Lytechinus variegatus. Journal of Structural Biology, 151, 18-29.

Robach, J.S., Stock, S.R., Veis, A. (2006): Mapping of magnesium and of different protein fragments in sea urchin teeth via secondary ion mass spectroscopy. Journal of Structural Biology, 155, 87-95.

Robach, J.S., Stock, S.R., Veis, A. (2009): Structure of first- and second-stage mineralized elements in teeth of the sea urchin Lytechinus variegatus. Journal of Structural Biology, 168, 452-466.

Salter, J.A. (1861): On the Structure and Growth of the Tooth of Echinus. Philosophical Transactions of the Royal Society of London, 151, 387-407.

Schmahl, W.W., Griesshaber, E., Neuser, R., Lenze, A., Job, R., Brand, U. (2004): The microstructure of the fibrous layer of terebratulide brachiopod shell calcite. European Journal of Mineralogy, 16, 693-697.

Schmahl, W.W., Griesshaber, E., Merkel, C., Kelm, K., Deuschle, J., Neuser, R.D., Goetz, A.J., Sehrbrock, A., Mader, W. (2008): Hierarchical fibre composite structure and micromechanical properties of phosphatic and calcitic brachiopod shell biomaterials - an overview. Mineralogical Magazine, 72, 541-562.

Schmidt, W.J. (1930): Die Skelettstücke der Stachelhäuter als Biokristalle. Zoologisches Jahrbuch Allgemeine Zoologie, 47, 357-510.

Schultz, H. (2005): Sea Urchins. A guide to worldwide shallow water species. Heinke & Peter Schultz Partner Scientific Publications, Hemdingen, Germany.

Stock, S.R., Veis, A. (2003): Sea urchin mineralized tissue. In: Electron Microscopy: Its Role in Materials Science. Edited by: Weertman, J.R.; Minerals, Metals, & Materials Society. Pages 287-293.

Stock, S.R., Barss, J., Dahl, T., Veis, A., Almer, J.D. (2002): X-ray absorption microtomography (microCT) and small beam diffraction mapping of sea urchin teeth. Journal of Structural Biology, 139, 1-12.

Stock, S.R., Nagaraja, S., Barss, J., Dahl, T., Veis, A. (2003a): X-ray microCT study of pyramids of the sea urchin Lytechinus variegatus. Journal of Structural Biology, 141, 9-21.

Stock, S.R., Ignatiev, K.I., Dahl, T., Veis, A., De Carlo, F. (2003b): Three-dimensional micro architecture of the plates (primary, secondary, and carinar process) in the developing tooth of Lytechinus variegatus revealed by synchrotron X-ray absorption microtomography (microCT). Journal of Structural Biology, 144, 282-300.

Stock, S.R., Ignatiev, K., Veis, A., Almer, J.D. De Carlo, F. (2004a): Microstructure of sea urchin teeth studied by multiple X-ray modes. In: Echinorderms: München. Edited by: Heimzeller, T., Nebelsick, J. H.; Taylor & Francis Group, London, ISBN: 04-1536-481. Pages 359-364.

Stock, S.R., Ignatiev, K.I., Veis, A. , DeCarlo, F., Almer, J.D. (2004b): MicroCT of sea urchin ossicles supplemented with microbeam diffraction. Developments in X-Ray Tomography, 5535, 11-20.

Stock, S.R., Lee, W.K. , Fezzaa, K., Barss, J., Dahl, T., Veis, A. (2001): X-ray absorption microtomography and phase contrast X-radiography of the structure of sea urchin teeth. Journal of Bone and Mineral Research, 16, S443-S443.

Stock, S.R., Barss, J., Dahl, T., Veis, A., Almer, J.D., De Carlo, F. (2003c): Synchrotron X-ray studies of the keel of the short-spined sea urchin *Lytechinus variegatus*: Absorption microtomography (microCT) and small beam diffraction mapping. Calcified Tissue International, 72, 555-566.

Stock, S.R., Ignatiev, K., Dahl, T., Barss, J., Fezzaa, K., Veis, A., Lee, W.K., De Carlo, F. (2003d): Multiple microscopy modalities applied to a sea urchin tooth fragment. Journal of Synchrotron Radiation, 10, 393-397.

Su, X., Kamat, S., Heuer, A.H. (2000): The structure of sea urchin spines, large biogenic single crystals of calcite. Journal of Material Science, 35, 5545-5551.

Vielzeuf, D., Floquet, N., Chatain, D., Bonnete, F., Ferry, D., Garrabou, J., Stolper, E.M. (2010): Multilevel modular mesocrystalline organization in red coral. American Mineralogist, 95, 242-248.

Wang, R.Z., Addadi, L., Weiner, S. (1997): Design strategies of sea urchin teeth: Structure, composition and micromechanical relations to function. Philosophical Transactions of the Royal Society B, 352, 469-480.

Wang, R.Z., Suo, Z., Evans, A.G., Yao, N., Aksay, I.A. (2001): Deformation mechanisms in nacre. Journal of Material Research, 16, 2485-2493.

Weber, J.N. (1969): Incorporation of Magnesium into Skeletal Calcites of Echinoderms. American Journal of Science, 267, 537-566.

Weber, J.N. (1973): Temperature dependence of magnesium in echinoid and asteroid skeletal calcite: A reinterpretation of its significance. Journal of Geology, 81, 543-556.
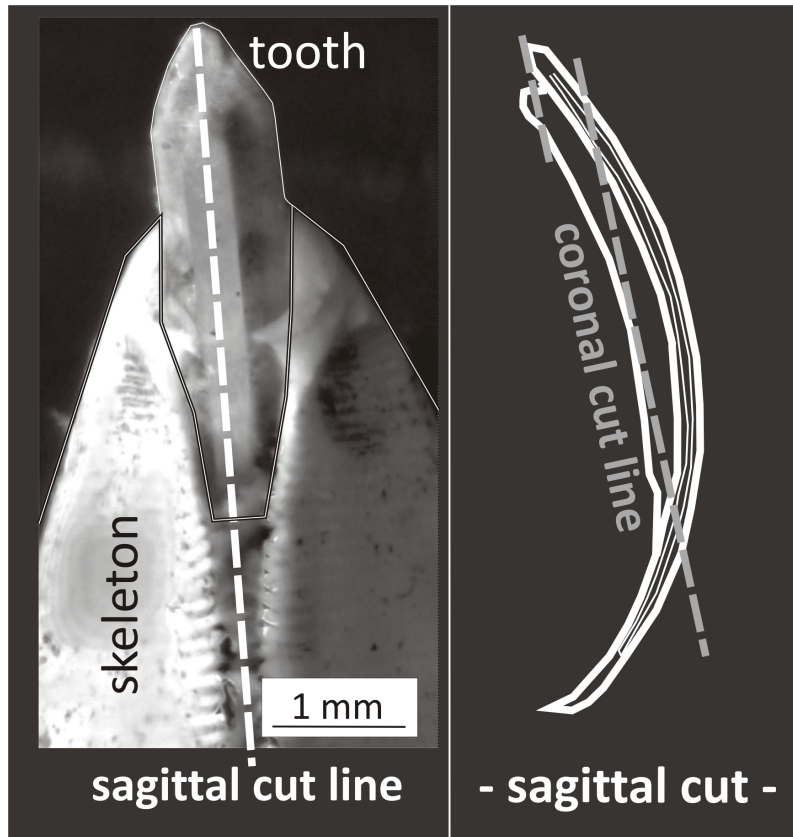
Appendix

Figure 3.28: Optical image of a portion of the masticator apparatus of the modern sea urchin *Paracentrotus lividus* showing an enlargement of a single tooth with its chewing tip, the keel and the embedding skeleton. The sagittal and the coronal cuts are indicated in the optical image and the schematic sketch through the tooth on the right hand side of the figure. It should be noted that the coronal cut line is parallel to the surface that is scrapped off during the self sharpening process.

4 Concluding Discussion

4.1 Structure and Formation of Schwertmannite

The results given in Section 3.1 show that the precipitation of schwertmannite by *Leptospirillum ferrooxidans* is a process of bioinduced mineralisation. *Leptospirillum ferrooxidans* produces Fe-(III) as a by-product during its respiration cycle and schwertmannite is favoured to precipitate under the pH-eH conditions in the culture vessels.

Older literature postulated that schwertmannite is precipitated by bacteria and that the bacteria are encrusted by schwertmannite during precipitation (Bigham et al. 1990, Ferris et al. 2004). It was shown in Section 3.1 that the influence of the bacterial strain *Leptospirillum ferrooxidans* EHS 2 on the precipitation of schwertmannite is limited: the bacteria oxidise Fe-(II) to Fe-(III) but they do not excrete schwertmannite from their cells. It was proposed by Ferris et al.(2004) that the hedgehog-like micromorphology of natural occurring schwertmannite (Fig. 4.1) results from the encrustation of bacteria cells with schwertmannite. This naturally implies that the microstructure of biogenic schwertmannite, produced by a process of bioinduced precipitation, results from the process of biomineralisation. However, Section 3.1 demonstrated that schwertmannite exhibits the same hedgehog structure in abiotic syntheses as the one present when it is precipitated by bacterial synthesis. Furthermore it is demonstrated that schwertmannite hedgehogs are massive mineral aggregates (Figure 4.1b). The present work showed that the microstructure of schwertmannite does not allow to distinguish between abiotically and a biotically precipitated schwertmannite. The micromorphology of schwertmannite can be changed by increasing the precipitation speed and it can thus be concluded that the micromorphology depends on kinetic effects.

Leptospirillum ferrooxidans formed EPS in the culture vessels where it was grown to produce schwertmannite (Section 3.1). It can be speculated whether the EPS is involved in the formation of schwertmannite. Banfield et al. (2000) showed that in EPS a process of oriented attachment of ferrihydrite nanoparticles to goethite crystals occurs. Furthermore it has been reported that in the EPS-analog *alginic acid* nanoparticles with akaganeite-like (and thus schwertmannite-like) assemble to goethite (Nesterova et al. 2003). That study was performed at a pH of 9.2 and thus far from the stability of schwertmannite (cf. Figure 1.1). An oriented attachment of iron oxide nanoparticles was also observed in aqueous solution and the absence of EPS or EPS-analogs (e. g. Burleson & Penn 2006). The EPS in schwertmannite formation by *Leptospirillum ferrooxidans* seems not to play a major role. The presence of EPS arises possibly from *Leptospirillum ferrooxidans'* mechanism for dissolving pyrite. This mechanism includes the separation of pyrite nanoparticles from their

substrate and the subsequent storage in an EPS capsule that surrounds the cell (Rochas-Chapana & Tributsch 2004). It is believed that this strategy allows the dissolution of pyrite that is stable within the redox potential that can be achieved by the cell: 600-1000 mV (Tributsch & Rochas-Chapana 2007). Within this regime the iron ions can not be removed from the pyrite lattice (Tributsch & Rochas-Chapana 2007). This created the need for the organism to develop a complex strategy to dissolve pyrite. In the case of the investigated pilot reactor the storage of pyrite particles in EPS is not necessary as the Fe-(II) is available in solution. The formation of EPS might be a result of the strong adaption of *Leptospirillum ferrooxidans* to pyrite dissolution.

It is interesting to compare the precipitation of schwertmannite by *Leptospirillum ferrooxidans* to the formation of *magnetosomes* as this shows how diverse the precipitation pathways of iron compounds by microorganisms are. Magnetosomes are a well-studied example for an iron mineral that is precipitated by a microorganism in a highly controlled manner. Magnetosomes are formed as specialized organelles by magnetotactic bacteria for geomagnetic navigation in aquatic habitats (Faivre & Schüler 2008). They consist commonly of magnetite (Fe_3O_4) or, less commonly, of greigite (Fe_3S_4) and are arranged in intracellular chains allowing the organism to swim along external magnetic fields (Faivre & Schüler 2008). This behaviour, known as *magnetotaxis*, facilitates the organisms to localize themselves in micro-oxic zones on the bottom of lakes. Magnetosomes are the most important constituent of magnetisation of sediments (Winklhofer & Petersen 2006). Magnetotactic bacteria are usually microaerophilic or anaerobic bacteria that are motile by a flagella (Bazylinski & Williams 2007). The best studied genus of magnetotactic bacteria belongs to the group of *Magnetospirillum*. Members of this genus are living in freshwater and form their magnetosomes from magnetite (Bazylinski & Williams 2007).

Magnetotactic bacteria can reduce and/or oxidise iron. Whereas *Leptospirillum ferrooxidans* is gaining its energy from the oxidation of large amounts of Fe-(II), there is no evidence that magnetotactic bacteria precipitate their magnetosensors to gain energy (Bazylinski & Williams 2007, Faivre & Schüler 2008): The amount of precipitated iron is from an energetic point of view insignificant as calculated by Blakemoore (1982) and also the availability of iron is no factor controlling their growth rate (Blakemore 1982, Meldrum et al. 1993, Faivre & Schüler 2008).

The iron reduction/oxidation of magnetotactic bacteria occurs in order to form magnetosomes. These magnetosomes are highly sensitive devices and in order to control the magnetic properties of the magnetosomes the organism precipitates them with an active control of phase (Faivre & Schüler 2008) and its morphology/habitus (Devouard et al. 1998). The particle size (Aratò et al. 2005) and the very pure chemistry (Thomas-Keprta et al. 2000) are features used to identify magnetite particles as magnetosomes (Winklhofer & Petersen 2006). From a crystallographic point of view the magnetite nanocrystals are of a high structural perfection with no extended lattice defects (Devouard et al. 1998). *Leptospirillum ferrooxidans* in contrast does not control any of these factors actively during schwertmannite formation.

The oxidation of Fe-(II) occurs in the case of *Leptospirillum ferrooxidans* in the periplasmic space (Tyson et al. 2004) and the precipitation of the mineral
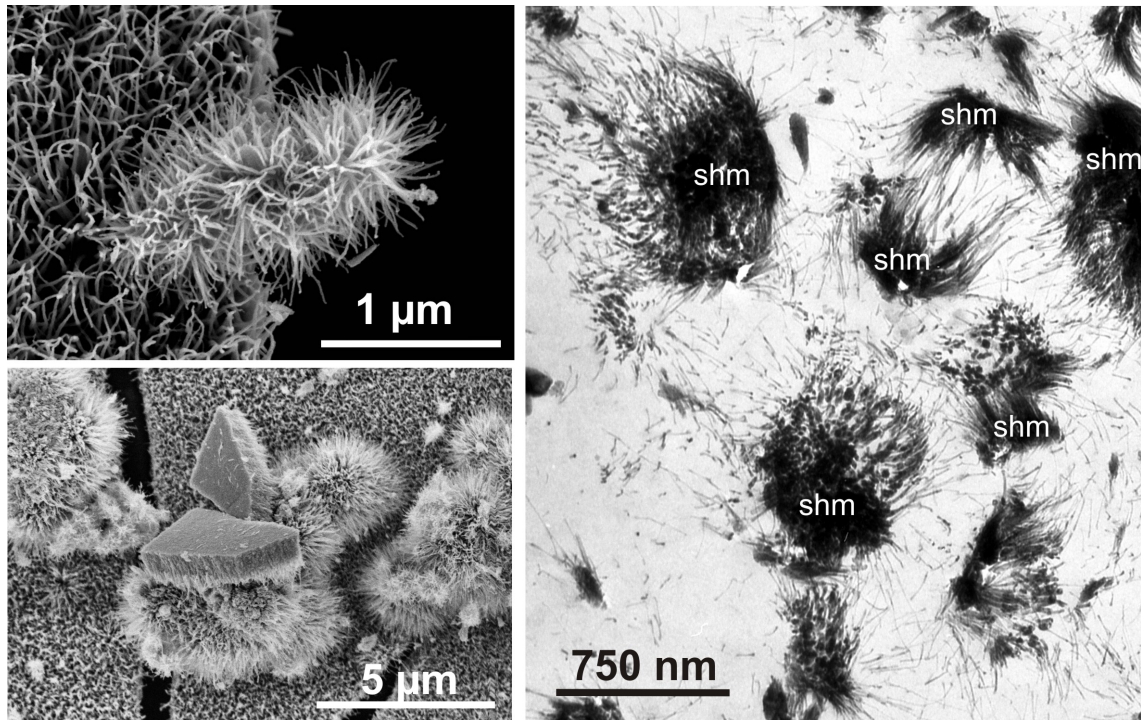
Figure 4.1: LEFT: SEM Images of typical schwertmannite hedgehogs as they are formed by biologically induced mineralisation as well as in abiotic experiments. Schwertmannite particles like shown in the upper image were wrongly interpreted as overgrown bacteria in older works. RIGHT: TEM sections through schwertmannite hedge hogs formed in the presence of iron oxidising bacteria. No signs of bacteria are inside the schwertmannite aggregates.

takes place extracellularly (Section 3.1). In the case of *Magnetospirillum* the reduction/oxidation of iron is taking place in the cytoplasm and the precipitation of magnetite crystals happens within magnetosome membranes that surround the crystal.

In conclusion the formation of magnetosomes is a highly controlled process of biomineralisation, whereas schwertmannite should be interpreted as a product of bioinduced mineralisation.

4.2 Structure and Growth of Calcitic Biominerals

Idiomorphic geologic calcite single crystals exhibit a habitus that is defined by their crystallography. In contrast, the morphology of sea urchin spines, whhich are large biogenic calcite single crystals (Section 3.4), is not influenced by the crystallographic structure of calcite. The only direction that can be correlated to a crystallographic axis is their longitudinal axis that is parallel to the calcite c-axis. The microporous structure of sea urchin spines (Figure 4.2), the *stereom*, is determined by the phylogenetic group of the organism (Smith 1980). This implies that the specific

morphology and micromorphology of the spine must be encoded genetically and is not controlled by environmental influences.

The mechanism by which the organism achieves the control over the microstructure is not well discussed in literature. Politi and co-workers showed that the spine is formed via a transition of ACC to calcite in adult (Politi et al. 2004) and larval sea urchins (Politi et al. 2008). ACC is isotropic and its shape can be controlled independent of the symmetry of a crystal lattice[1]. Furthermore it is known that areas in which sea urchin spines grow are surrounded by a thin cellular tissue, the *epithelium* (Märkel & Röser 1983). The control over the morphology of the spine is probably achieved by the following scenario: The spine can only continue growing where ACC is available. Thus the localized supply of ACC allows control over the morphology of the spine. The morphology of the ACC is controlled by the topology of the surrounding epithelium and thus the morphology of the spine is defined by the morphology of the epithelium.

Whereas the calcitic stereom does not resemble the structure of idiomorphic calcite single crystals, there are some similarities to another single crystalline calcitic biomineral: *calcareous sponge spicules*. The microstructure of calcarous sponge spicules was recently reviewed by Sethmann & Wörheide (2008). Calcarous sponge spicules are single crystals with sizes in the range of 100's of micrometers and can be distinguished in the simplest cases in *monoactine, diactine* and *triactine* morphologies[2]. Monoactine spicules have a needle-like morphology, diactine also but two tips are present. Triactine spicules can be oriented in various ways. The simplest way are star shaped spicules. The three equiradial actines are in one plane and have an angle of 120° (e. g. Aizenberg et al. 1995, Aizenberg et al. 1996). These morphologies correspond to the crystallographic symmetry of the calcite lattice: e. g. in the triactine structure described above the single actines are parallel to the a*-axes (Aizenberg et al. 1996). The influence of the crystallographic pattern seems to be limited to the orientation of the actines: the actines themselves are roundish and no signs of crystal faces are present (Sethmann & Wörheide 2008) as it is also observed in sea urchin spines. Sethmann & Wörheide (2008) compare the sea urchin stereom to calcareous sponge spicules and find several similarities: Both structures should be regarded as mesocrystals. They intercalate proteins and do not cleave along the calcite cleavage planes (Sethmann & Wörheide 2008). Also the Mg content of calcareous sponge spicules (5-18 mol-%, Sethman & Wörheide 2008) is similar to for sea urchin spines (cf. Magdans & Gies 2004 who observed Mg concentrations of 2-12 Mol-% in spines from various species). Both taxa control the crystallographic orientation of their single crystalline mineralisates but the morphology is not limited by the crystallography of calcite.

Geologic calcite exhibits a very pronounced cleavage along {104}. In none of the calcitic biominerals investigated in this work the prominent {104}-cleavage plane is visible (see SEM images of fractured surfaces throughout chapter 3 and Figure 4.2).

---

[1]The term *amorphous* originates from the fact that such materials do not have a distinct morphology.

[2]Additional morphologies like *tetractine* and *pentacine* spines are present (e. g. Boury-Esnault & Tützler 1997, Rossi et al. 2006)
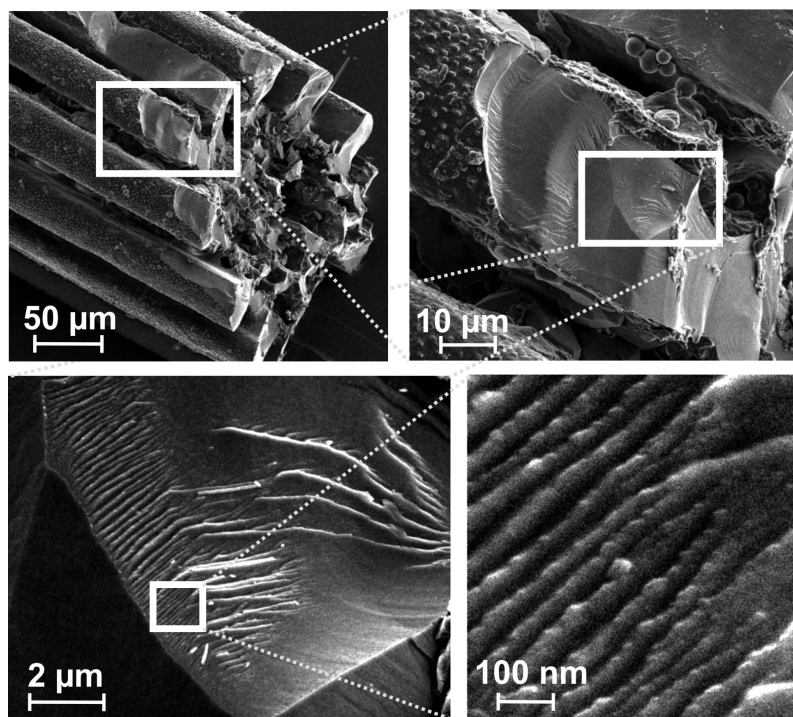
Figure 4.2: SEM images that show the subsequent magnification of a fractured sur-
face of a sea urchin spine of *Holopneustes porosissimus*. The complete
spine is one single crystal. Note that no sign of calcite cleavage is present
but that the surface at high magnification seems to consist of globular
aggregates.

Detailed images of the surface in contrast show that they consist of globular aggre-
gates (e. g. Figure 4.2). This effect is observed in a variety of calcitic biominerals.
Beside Magdans & Gies (2004) who tried to explain the absence of this cleavage
by the incorporation of Mg in the calcite lattice of sea urchin calcite, the com-
mon theory to explain the absence of the calcite {104}-cleavage is the intercala-
tion of proteins in the calcite structure. This model was proposed to be valid for
many organisms like brachiopods (Schmahl et al. 2008), sea urchins (Sethmann et
al. 2005), Foraminifera (Berman et al. 1993) and calcitic sponge spicules (Aizen-
berg et al. 1995). Whereas the idea of intercalated proteins in the calcite structure
is not new, it was only recently studied in more detail by Sethmann et al. (2005)
who showed that the incorporation of aspartic acid-rich proteins could prevent the
{104}-cleavage of synthetic calcite. Aspartic acid-rich proteins are common in cal-
citic biominerals (e. g. Mitterer 1978, Weiner 1979, Robach et al. 2006, Rahman &
Oomori 2008). Subsequently Sethmann et al. (2006) proposed that the proteins
are preferably intercalated between nano-clusters of tens of nanometres in size in
sponge spicules, a model that also fits very well the surface roughness observed in
fractured surfaces of the samples investigated in the present study (Figure 4.2 and
SEM images of fractured surfaces throughout Chapter 3).

The hardness of geologic calcite is lower than that of calcite formed by processes of biocontrolled mineralisation (Sections 3.2 and 3.6). This fact can be attributed to substitution strengthening: Mg, as it occurs in all calcites that were investigated in the present work, contributes significantly to an increase in hardness and elastic modulus of calcite. High Mg-concentrations in calcitic biomaterials are expected to lead to solid solution hardening (Section 3.6, Wang et al. 1997, Stock 2003, Magdans & Gies 2004). As it was shown in Section 3.6, the pure Mg-carbonate magnesite is very hard and stiff (nanohardness: 9.2 GPa, E-modulus: 145 GPa) compared to calcite (nanohardness: 3.0 GPa, E-modulus 9.2 GPa). This results from an additional effect: Mg^{2+} is smaller than Ca^{2+} and thus has a stronger ionic field strength leading to a more covalent bond of Mg-O compared to the Ca-O bond. The bond with a stronger covalent character results in a harder material. The Mg-incorporation in calcite is an example for another strategy of mechanical optimisations additional to those discussed in the introduction; it can be referred to as *chemical optimisation.*

In the majority of geologic carbonate rocks the microstructures are either dominated by sedimentary processes or by metamorphosis. These microstructures have little in common with the microstructure of the investigated polycrystalline calcitic biominerals. However, when speleothems are in constantly wet condition and the solution has a low supersaturation their microstructure (Frisa et al. 2000, Neuser & Richter 2007) is very similar to the microstructure of the columnar shell layer of the brachiopod *Liothyrella neozelanica* (Section 3.2 and Figure 4.3). This columnar shell layer microstructure is frequent in calcitic biominerals, it also appears in avian egg-shells (Rodriguez-Navarro et al. 2002, Dalbeck & Cusack 2006) and in the calcitic prismatic layer of certain gastropods (Pérez-Huerta et al. 2011). There are also examples of technical materials that show the same microstructure like magnesium-alloys (Eiken 2009), polycrystalline silicon of solar cells (Arafune et al. 2007) and other products produced from directional solidification (e. g. D'Souza et al. 2000). This similarity of structures can be explained by the fact that these microstructures are formed in a process of competitive growth: The microstructures evolve by a process in which nucleation of a crystalline phase starts on a plane that only allows the growth in one hemisphere. The development of seeds is either induced by a temperature gradient (Arafune et al. 2007, Eiken 2009), the drip rate (Frisa et al. 2000) or by the organism (Section 3.2, Dalbeck & Cusack 2006). The growing mineral phase has an anisotropic growth speed what implies that certain crystallographic orientations grow faster than others. Growth selection occurs as only seeds that are oriented in a way that the fastest growing direction is perpendicular to the nucleation layer grow faster and thus block crystals oriented in another manner (Section 3.2, Rodriguez-Navarro 2001). This mechanism of faster and slower growing crystallographic directions is technically exploited in the manufacturing of single crystalline turbine blades from Ni-base superalloys in order to select only one seed (Versnyder & Shank 1970, D'Souza et al. 2000).

In the all of the above mentioned calcitic microstructures that are formed by a process of competitive growth the longitudinal axes of the columns or prisms are parallel to the crystallographic c-axis. In the case of the avian egg-shell (Dalbeck & Cusack 2006) it was proposed that this is can be achieved by proteins (Hernández-
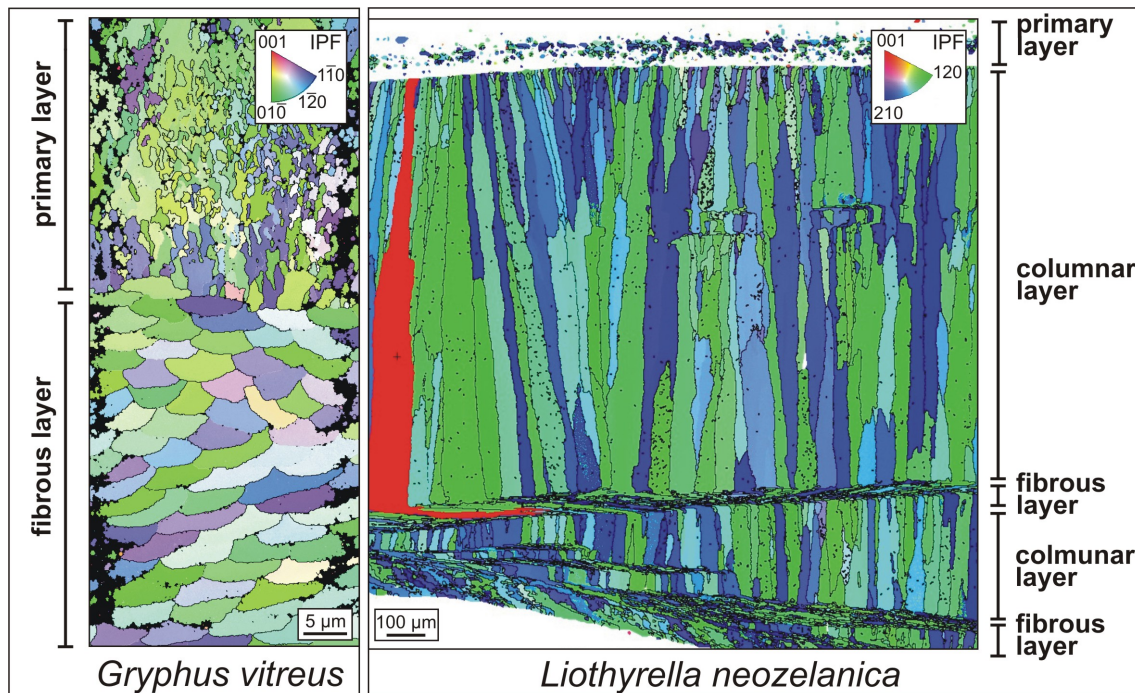
Figure 4.3: EBSD maps performed on recent brachiopod shells coloured in an inverse pole figure colouring (IPF). LEFT: EBSD map of the outer primary and the subsequent fibrous layer of the shell *Gryphus vitreus*. The strongly interdigitating 3D-jigsaw-like microstructure of the primary layer was described for the first time in this work. RIGHT: EBSD map of the outer primary and the subsequent columnar layer that is alternating with an fibrous layer of the shell of *Liothyrella neozelanica*.

Hernández et al. 2008) but the protein controlling it could not be identified. As the same preferred crystallographic orientation pattern is also observed in speleothems (Neuser & Richter 2007) it can be argued that such a control of the organism is not necessary as the c-axis is the fastest growing axis also in abiotic systems.

Whereas the columnar brachiopod shell layer has a microstructure well known from a variety of materials, the primary layer microstructure of brachiopod shells is unique for single phase materials (Section 3.3). This valve layer is formed by dendrite-like calcite crystals which are interdigitating in a jigsaw-puzzle-like manner. This results in a very strong and resistive microstructure (Section 3.2). The primary layer is the outermost calcitic layer of the brachiopod shell. It is thus not surprising that the primary layer microstructure is highly abrasion resistant as one crack is not sufficient to remove a grain (Section 3.3). However, it should noted that the primary layer is covered by a thin organic membrane, the periostracum (e.g. Williams et al. 1997). It is not certain that the high resistance to abrasion of the primary shell layer is of any advantage for the animal. The necessity of such an optimization may be proven by reports of injuries of the periostracum. However, I am not aware of literature mentioning such injuries, but few studies dealing with living brachiopods

exist and the fact that those observations were never reported does not necessarily mean that such injuries do not occur.

Even though it is not certain if the high abrasion resistivity of the brachiopod shell primary layer can be interpreted morphofunctionally, the structuring of brachiopod shell hardness can (Section 3.2). The outside primary layer is the hardest and the hardness of the shell layer gradually decreases towards the inside of the animal. Increasing the hardness of the outer surface and the toughness of the inner material leads to a structure optimized against fracture that is realized also in bicycle helmets and human teeth (Chai et al. 2009). The structuring of the hardness is achieved by a combination of microstructural features (Section 3.3) and chemical structuring. Mg that increases the hardness of calcite can be found in its highest concentrations the hard primary layer (Griesshaber et al. 2007, Eckart 2008).

The formation the microstructure of the primary shell layer can not be explained by mechanisms known from classical mineralogy such as those which apply for the tertiary layer. Note that the shell layer is also not suitable for $\delta^{18}O$ (e. g. Parkinson et al. 2005). The present work proposes a growth model based on an ACC precursor (Section 3.3) as observed in brachiopod shells (Griesshaber et al. 2009, Schmahl et al. 2009). The ACC is stored in capsules and after or during the crystallisation of one capsule a mineral bridge forms connecting two capsules. Mineral bridges are believed to be common in $CaCO_3$-biominerals and were observed e. g. in molluscs (Schäffer et al. 1997, Jacob et al. 2008) and sea urchins (Oaki & Imai 2005). The bridging of the crystallisation front from one capsule to the other allows the crystallisation front to pass on. Misorientations observed within single grains support this theory. As the mineral bridges form at random places of the capsule and as organic molecules can accumulate and prevent the progress of the crystallisation front a strongly interdigitating microstructure forms.

The primary shell microstructure was the first ceramic-like single phase microstructure showing a jigsaw-like interdigitation of crystals (Figure 4.3). A similar structure was recently described for the suture of bone plates in tortoise shells (Krauss et al. 2009), a material that can be deformed at small loads but has a rigid behaviour at high loads (Krauss et al. 2009). The structures seem very similar from the topology and both structures consists of hard, mineralised digits that are surrounded by softer organic matter. However there are two major differences to the brachiopod primary layer. The first difference is the length scale on which these structures can be observed: In the tortoise shells the interdigitation is appearing in the scale of 100's of microns whereas the scale for the brachiopod shell primary layer is two orders of magnitude lower. The second difference is the ratio of organic / inorganic components. This ratio is significantly higher in the tortoise shell. Krauss et al. (2009) did not quantify the content of non-mineralized tissue but the images shown indicate that the organic matrix is a major constituent that is clearly visible on the same length scale as the interdigitation. In the brachiopod primary shell layer in contrast the organic content is limited to thin organic membranes (0.5-1.5 nm, cf. Section 3.3) that are only visible in TEM. The content is around 2 wt.-% in brachiopod shells (Schmahl et al. 2008)
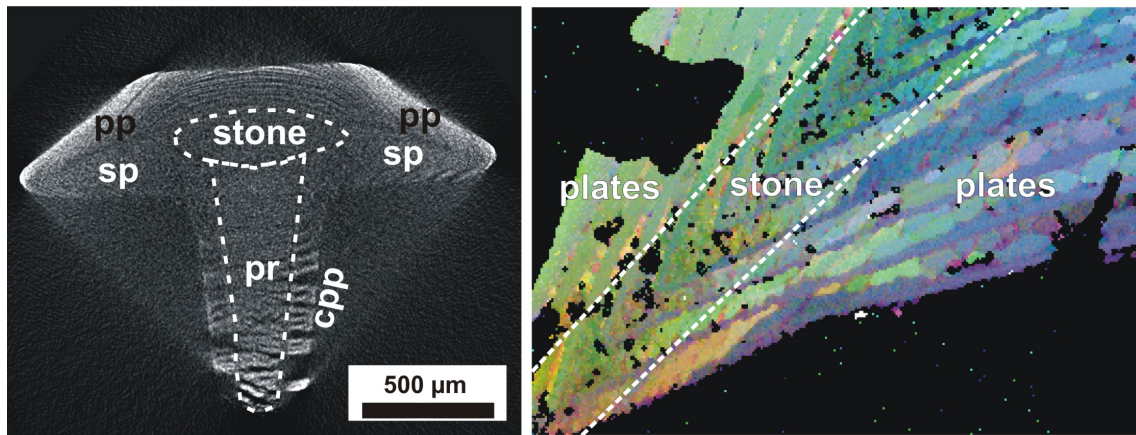
Figure 4.4: LEFT: Virtual transversal section though a sea urchin tooth obtained by nano computed tomography. The stone is in the centre of the structure. pp=primary plates, sp=secondary plates, pr=prisms, cpp=carinar process plates. RIGHT: EBSD map of the tip of a sea urchin tooth obtained at a transversal section. Black points could not be indexed.

From an material scientific point of view the study of teeth has one great advantage to the study of other biomaterials: the purpose of teeth is obvious and therefore purpose optimizations are easier to understand. The purpose of teeth is to reduce the size of food by cutting or grinding to be either able to ingest the food or to facilitate its digestion. In this section we will compare the sea urchin teeth investigated in this work (Section 3.6) to human teeth (e. g. reviewed by He & Swain 2008 and Lawn et al. 2010). Both varieties of teeth consist of Ca-minerals: the mineralized parts of human teeth consist of hydroxyapatite and the mineralized part of sea urchin teeth of calcite (Table 1.1).

Comparing human and sea urchin teeth is so interesting as they have two contrary ways of dealing with abrasion. The abrasion arises in both cases as in the masticatory apparatus of human and sea urchins the ingestion of food involves a mutual grinding of the teeth. This grinding is exploited by sea urchins in a self-sharpening mechanism of their teeth (Section 3.6). The key for understanding the self-sharpening mechanism (described e. g. in Section 3.6) is a part of the tooth called stone. This stone is the hardest part of the quasi single crystalline sea urchin tooth. The hardness is achieved by increasing the Mg-content of the calcite. However, in the stone also the highest amount of organic matter was detected (Section 3.6). In a transversal section through a sea urchin tooth the stone can be found in the centre (Figure 4.4). The stone also forms the tip of the tooth that is used to graze on the substrate. During feeding the hard tip scratches over the outside of other teeth and removes by this movement softer plates that surround the tip of other teeth. The sea urchin tooth constantly regrows by a process in which ACC crystallizes to calcite.

Human teeth in contrast can not grow after they achieved their final size. This leads to a completely different structure of the tooth: Whereas the hardest part in sea urchin teeth is in the centre of the tooth, the hardest part of the human tooth,

the *enamel*[3], is the outer layer. The structure of a hard outside (enamel) and a soft inside (*dentine*) that is present in the human tooth (Cuy et al. 2002) is also found in brachiopod shells (Section 3.2). The higher resistivity of enamel compared to that of dentine is attributed to an increase of the mineral content: 70% in the inner dentine to 96% in enamel (Lawn et al. 2010), the Mg-content in the human tooth is anti-correlated to the hardness (Cuy et al. 2002). In sea urchin teeth in contrast the hardness of the stone is increased due to an increase of the Mg-content whereas the mineral content in the stone is lower compared to the rest of the tooth (Section 3.6). Dentine is a classical example of an highly complex hierachically composite material with excellent material properties (e. g. He & Swain 2007, Chai et al. 2009, Lawn et al. 2010, Raue & Klein 2010). It consits of heavily mineralized curved rods that extend from the dentine to the outer surface. These rods have diameters around $10\,\mu m$ and posses a hierachical structure (Lawn et al. 2010). The rods are sourrounded by an organic rich interrod sheath structure (He & Swain 2008). Whereas pure enamel is very brittle in combination with dentine its toughness is strongly increased (Chai et al. 2009). Beside all these optimizations that make enamel the hardest material in the human body, the weak point in human teeth is their abrasion[4] whereas sea urchins use the grinding to keep sharp teeth.

In the present work no isotope values were measured and thus the point if brachiopod shells incorporate O isotopes in equilibrium with the environment cannot be discussed. However, when the isotope values from skeleton minerals are studied, it should be kept in mind that the diagenetic alteration starts soon after the death of the proxy (Brand et al. 2011). Brand et al. (2011) clearly underline that the degree of alteration cannot be determined by hypothetical and theoretical considerations but that the "the best proxy is the one that has passed the most screening tests" (Brand et al. 2011). This work provides an insight how unaltered brachiopod shells look like and furthermore it shows which details should be addressed with care in geochemical studies: Geochemical literature commonly assumes that the primary brachiopod shell layer did not precipitate in isotopic equilibrium with the ocean water whereas the *secondary layer* (sometimes followed by a *tertiary layer*) precipitates in isotopic equilibrium (e. g. Veizer et al. 1999, Brand et al. 2003, Yamamoto et al. 2010). In Section 3.2 it was demonstrated that brachiopod shell layers can interdigitate and thus special care must be taken in geochemical studies to not probe an intercalation primary shell layer material in other shell layers. It should be noted that the interdigitation of brachiopod shell layers also vetos the nomenclature of brachiopod shells by numbering the layers from the outside to the inside as most geochemical literature does. Geochemical studies should furthermore be very cautious where to take samples of the shall as not only an interdigitation of shell layers can occur but also sediment particles such as clay minerals and Foraminifera are incorporated in the shell (Section 3.2).

---

[3]Enamel is the hardest structure of the human body (Lawn et al. 2010)

[4]Wear of human teeth should not be underestimated: in an exemplary population examined by Cunha-Cruz et al. (2010) moderate to severe tooth damage due to wear were found in one of two adult patients. Pathological grinding of teeth (bruxism), as 85 - 90% of the population will carry out at some point in their life (Bader & Lavigne 2000), can lead to such increased tooth wear.

The Mg/Ca ratio of skeletal parts of Echinoderma has been correlated in the literature to the conditions the organism experienced during its live. Some authors correlate the Mg/Ca ratio of the calcitic skeletons to the Mg/Ca ratio of the ocean water in which the organism lived (Dickson 2002, Dickson 2004, Ries 2004) or to the water temperature the animal experienced (Borremans et al. 2009, Hermans et al. 2010). The Mg/Ca ratio was determined in none of these studies in a spatial resolved manner: Dickson et al. (2002) used EPMA single spot analyses, Dickson (2004) determined the Mg content by XRD powder samples and EDX spot analyses. Borremans et al. (2009) and Hermans et al. (2010) investigated ICP-AES powder samples. The lack of a spatially resolved information did not allow the the authors of these studies to realize that the Mg-concentration is strongly patterned in the stereom and that the Mg incorporation can thus not appear in thermodynamic equilibrium (Section 3.5). The use of this signal as a proxy is thus not possible.

5 Biologic Influence on Mineralisation Processes

It was discussed above that the precipitation of schwertmannite in presence of *Leptospirillum ferrooxidans* must be interpreted as *bioinduced mineralisation*. The precipitation of calcite by the organisms investigated in this work in contrast is clearly a process of *biocontrolled mineralisation*. The characteristics of the minerals and their formation are summarized below and shown in Table 5.1.

Leptospirillum ferrooxidans has no influence on the phase that is precipitated and schwertmannite only forms when it is stable. Calcite as it is produced by sea urchins and brachiopods is the stable phase in the modern oceans. However, the biomineral is precipitated in a confined compartment, which is separated from the ocean water. The thermodynamic conditions within the animal are controlled by metabolism and determine which phase is precipitated. Thus the organism controls the phase that is precipitated.

Schwertmannite precipitates directly from solution. The role of the organism is to oxidise Fe-(II) to Fe-(III) and the lower solubility of Fe-(III) compared to Fe-(II) leads to the precipitation of schwertmannite. All the investigated calcitic biominerals in contrast precipitate from an amorphous calcium carbonate precursor that is produced by the organism.

The only influence of *Leptospirillum ferrooxidans* on the precipitation of schwertmannite is the oxidation of iron and it thus does not influence the composition of the precipitate. The chemical structuring in brachiopod shells enhances the resistivity of the entire shell. It was concluded that brachiopods control the chemical structuring. Also sea urchins actively influence the structural patterning of the Mg in their teeth. No active influence on the chemical composition of sea urchin spines is reported but distribution patterns of Mg were observed.

Schwertmannite is a waste-product of the respiration of the organism with no use for the organism. All the calcitic biominerals investigated in the present work are organs with distinct functions. The brachiopod shell and the sea urchin spines are interpreted to serve mainly a protective role whereas sea urchin teeth are needed for the food intake by the organism.

The microstructure of schwertmannite precipitated by *Leptospirillum ferrooxidans* is identical to the microstructure formed by abiotic pathways. In brachiopod shells there are microstructures (i.e. primary and fibrous layer) that are distinct from abiotic calcite. The columnar layer however has a microstructure that also appears in geologic calcites. Sea urchin spines and teeth show both microstructures that are distinct from abiotic calcites.

Table 5.1: Comparison of the control of the organism over the products of biomineralisation.

	Bioinduced Mineralisation	Biocontrolled Mineralisation		
	SCHWERTMANNITE *Leptospirillum ferrooxidans*	brachiopod shell	CALCITE sea urchin spine	sea urchin tooth
Phase	depends on environmental conditions	controlled by organism	controlled by organism	controlled by organism
Formation from	precipitates directly from solution surrounding organism	amorphous precursor phase produced by organism	amorphous precursor phase produced by organism	amorphous precursor phase produced by organism
Chemical composition	depends on environmental conditions	Mg content probably controlled by the organism	unknown	Mg content controlled by the organism
Purpose	waste product with little or no use for the organism	organ with distinct purpose	organ with distinct purpose	organ with distinct purpose
Microstructure	identical to abiotic product	depending on the shell layer – microstructure can be controlled by organism but also microstructures of abiotic products appear	Microstructure controlled by organism, distinct from abiotic products	Microstructure controlled by organism, distinct from abiotic products

Acknowledgements

Bibliography

This listing contains the references cited within the Chapters 1, 2 & 4. The references cited within Chapter 3 are listed at the end of each particular section.

Acharya, C., Sukla, L. B., Misra, V. N. (2003): Review Biodepyritisation of coal. Journal of Chemical Technology and Biotechnology, 79, 1-12.

Addadi, L., Raz, S., Weiner, S. (2003): Taking Advantage of Disorder: Amorphous Calcium Carbonat and Its Role in Biomineralization. Advanced Materials. 2003, 15, 959-970.

Aizenberg, J., Hanson, J., Ilan, M., Leiserowitz, L., Koetzle, T. F., Addadi, L., weiner, S. (1995): Morphogenesis of calcitic sponge spicules: a role for specialized proteins interacting with growing crystals. Journal of the Federation of American Societies for Experimental Biology, 9, 262-268.

Aizenberg, J., Ilan, M., Weiner, S., Addadi, L. (1996): Intracrystalline Macromolecules are Involved in the Morphogenesis of Calcitic Sponge Spicules. Connective Tissue Research, 34, 255-261.

Alexander, R. B. (2001): Functional Morphology and Biomechanics of Articulate Brachiopod Shells. The Paleontological Society Special Papers, 7, 145-170.

Arafune, K., Ohishi, E., Sai, H., Ohshita, Y., Yamaguchi, M. (2007): Directional solidification of polycrystalline silicon ingots by succesive relaxation of supercooling method. Journal of Crystal Growth, 308, 5-9.

Aratò, B., Zoltàn, S., Flies, C., Schüler, D., Frankel, R. B., Buseck, P. R., Pòsfai, M. (2005): Crystal-size and shape distribution of magnetite from uncultured magnetotactic bacteria as a potential biomarker. American Mineralogist, 90, 1233-1241.

Aristotle (350 B.C.): $\Pi\epsilon\rho\iota$ $T\alpha$ $Z\omega\alpha$ $I\sigma\tau o\rho\iota\alpha\iota$, Book IV. Translated by D'Arcy Wentworth Thompson: The History of Animals, Book IV.
$http://classics.mit.edu/Aristotle/history\_anim.4.iv.html$
Obtained on March, 23rd 2011.

Bader, G., Lavigne, G. (2000): Sleep bruxism; an overview of an oromandibular sleep movement disorder: Review Article. Sleep Medicine Reviews, 4, 27-43.

Banfield, J. F., Welch, S. A., Zhang, H. Ebert, T. T., Penn, R. L. (2000): Aggregation-Based Crystal Growth and Microstructure Develpment in Natural Iron Oxyhydroxide Biomineralisation Products. Science, 289, 751-754.

Barthelat, F., Tang, H., Zavattieri, P.D., Li, C. M., Espinosa, H. D. (2007): On the mechanics of mother-of-pearl: A key feature in the material hierarchical structure. Journal of the mechanics and Physics of Solids. 55, 306-337.

Barthelat, F., Espinosa, H. D. (2007): An Experimantal Investigation of Deformation and Fracture of Nacre-Mother of Pearl. Experimental Mechanics, 47, 311-324.

Bazylinski, D. A., Willians, T. J. (2007): Ecophysiology of Magnetotactic Bacteria. In: Magnetoreception and Magnetosomes in Bacteria. Edited by: Schüler, D.; Springer, Germany, ISBN: 3-540-37467. Pages 37-76.

Beniash, E., Aizenberg, J., Addadi, L., Weiner, S. (1997): Amorphous calcium carbonate transforms into calcite during sea urchin larval spicule growth. Proceedings of the Royal Society London B, 264. 461-465.

Bentov, S., Brownlee, C., Erez, J. (2009): The role of seawater endocytosis in the biomineralization process in calcareous foraminifera. Proceedings of the National Academy of Sciences, 206, 21500-21504.

Berman, A., Hanson, J., Leiserowitz, L., Koetzle, T. F., Weiner, S., Addadi, L. (1993): Biological Control of Crystal Texture: a Widespread Strategy for Adapting Crystal Properties to function. Science, 259, 776-779.

Bigham, J. M., Schwertmann, U., Carlson, L., Murad, E. (1990): A poorly crystallized oxygydroxysulfate of iron formed by bacterial oxidation of Fe(II) in acid mine water. Geochimica et Cosmochimica Acta, 54, 2743-2758.

Bigham, J. M., Carlson, L., Murad, E. (1994): Schwertmannite, a new iron oxyhydroxysulphate from Pyhäsalmi, Finnland, and other localities. Mineralogical Magazine, 58, 641-648.

Bigham, J. M., Schwertmann, U., Traina, S. J., Winland, R. M., Wolf, M. (1996): Schwertmannite and the chemical modeling of iron in acid sulfate waters. Geochimica et Cosmochimca Acta, 60, 2111-2121.

Blakemore, R. P. (1982): Magnetotactic Bacteria. Annual Reviews of Microbiology, 36, 217-238.

Bond, P.L., Smriga, S. P., Banfield, J. F. (2000): Phylogeny of Microorganisms Populating a Thick, Subaerial Predominantly Lithotrophic Biofilm at an Exterme Acid Mine Drainage Site. Applied and Environmental Microbiology, 66, 3842-3849.

Borremans, C., Hermans, J., Baillon, S., André, L., Dubois, P. (2009): Salinity effects on the Mg/Ca and Sr/Ca in starfish skeletons and the achinoderm relevance for paleoenvironmental reconstructions. Geology, 37, 351-354.

Boury-Esnault, N., Rützler, K. (1997): Thesaurus of sponge morphology. Smithonian Contributions to Zoology. 596, 1-55.

Brand, U., Logan, A., Hill, N., Richardson, J. (2003): Geochemistry of modern brachiopods: applications and implications for oceanography and paleoceanography. Chemical Geology, 198, 305-334.

Brand, U., Logan, A., Bitner, M. A., Griesshaber, E., Azmy, K., Buhl, D. (2011): That is the ideal proxy of Paleozoic seawater chemistry? Memoirs of the Association of Astralasian Palaeontologists, 41, 9-24.

Buggisch, W., Keller, M., Lehner, O. (2003): Carbon isotope record of Late Cambrian to Early Ordovician carbonates of the Argentine Precordillera. Palaeogeography, Palaeoclimatology, Palaeoecology, 195, 357-373.

Bunge, H. J., Esling, C. (1986): Quantitative Texture Analysis. DGM Informationsgesellschaft m. b. H., Germany. ISBN: 3-88355-103-1.

Burton, E. D., Johnston, S. G., Watling, K., Bush, R. T., Keene, A. F., Sullivan, L. A. (2010): Arsenic Effects and Behaviour in Association with The Fe(II)-Catalyzed Transformation of Schwertmannite. Environmental Science & Technology. 44, 2016-2021.

Burleson, D. J., Penn, R. L. (2006): Two-Step Grwoth of Goethite from Gerrihydrite. Langmuir, 22, 402-409.

Carlson, L., Bigham, J.M., Schwertmann, U., Kyek, A., Wagner, F. (2002): Scavenging of As from Acid Mine Drainage by Schwertmannite and Ferrihydrite: A Comparison with Synthetic Analogues. Environmental Science and Technology, 36, 1712-1719.

Carpenter, S.J., Lohmann, K.C. (1995): ^{18}O and ^{13}C values of modern brachiopod shells. Geochimica Cosmochimica Acta, 59, 3749– 3764.

Chai, H., Lee, J. J. W., Constantino, P. J., Lucas, P W., Lawn, B. R. (2009): Remarkable resilience of Teeth. Proceedings of the National Academy of Sciences, 106, 7289-7293.

Cody, G. D. (2004): Transiontion Metal Sulfides and the Origins of Metabolism. Annual Reviews of Earth and Planetary Sciences, 32, 569-599.

Coelfen, H., Antonietti, M. (2005): Mesocrystals: Inorganic Superstructures Mady by Highly Parallel Crystallization and Controlled Alignment. Angewandte Chemie International Edition, 44, 5576-5591.

Coelfen, H., Antonietti, M. (2008): Mesocrystals and Nonclassical Crystallization. First Edition, John Willey & Sons, England. ISBN: 978-0-470-02981-7.

Cohen, A. L., Gaetani, G. A. (2010): Ion partioning and the geochemistry of coral skelettons: solving the mystery of the vital effect. In: EMU Notes in Mineralogy, 10: Ion partitioning in ambient-temperature aqueous systems. Edited by: Prieto, M., Stoll, H.; European Mineralogical Union and the Mineralogical society of Britain and Ireland. London, UK, ISBN: 978-0-903056-26-7. Pages 377-339.

Cornell, R. M., Schwertmann, U. (2003): The Iron Oxides. WILLEY-VCH, Weinheim, Germany. Second edition. ISBN-3-527-30274-3.

Currey, J.D., Nichols, D. (1967): Absence of Organic Phase in Echinoderm Calcite. Nature, 214, 81-83.

Currey, J. D. (1977): Mechanical properties of mother of pearl in tension. Proceedings of the Royal Society of London B, 196, 443-463.

Cuy, J. L., Mann, A. b., Livi, K. J., Teaford, M. F., Weihs, T. P. (2002): Nano-indentation mapping of the mechanical properties of human molar tooth enamel. Archives of Oral Biology, 47, 281-291.

Cunha-Cruz, J., Pashova, H., Packard, J. D., Zhou, L., Hilton, T. J. (2010): Tooth wear: prevalence and associated factors in general practice patients. Community Dentistry and Oral Epidemiology, 38, 228-234.

Dalbeck, P., Cusack, M. (2006): Crystallography (Electron Backscatter Diffraction) and Chemistry (Electron Probe Microanalysis) of the Avian Eggshell. Crystal Growth & Design, 6, 2558-2562.

Denison, R.E., Koepnick, R.B., Burke, W.H., Hetherington, E.A., Fletcher, A. (1997): Construction of the Silurian and Devonian seawater $^{87}Sr/^{86}Sr$ curve. Chemical Geology, 140, 109-121.

Devourad, B., Pósfai, M., Hua, X., Bazylinsky, D. A., Frankel, R. B., Buseck, P. R. (1998): Magnetite from magnetotactic bacteria: Size distributions and twinnings. American Mineralogist, 83, 1387-1398.

Dickson, J. A. D. (2002): Fossil Echnioderms As Monitor of the Mg/Ca Ratio of Phanerozoic Oceans. Science, 298, 1222-1224.

Dickson, J. A. D. (2004): Echinoderm Skeletal Preservation: Calcite-Aragonite Seas and the MgCa Ratio of Phanerozoic Oceans. Journal of Sedimentary Research, 74, 355-365.

Domic, E. M. (2007): A Review of the Development and Current Status of Copper Bioleaching Operations in Chile: 25 Years of successful Commercial Implementation. In: Biomining. Edited by: Rawlings, D. E., Johnson, D. B.; Springer, Germany, ISBN: 3-540-34909-X. Pages 81-96.

Donnay, G., Pawson, D.L. (1969): X-Ray Diffraction Studies of Echinoderm Plates. Science, 166, 1147-1150.

Dunlop, J. W. C., Fratzl, P. (2010): Biological Composites. Annual Reviews of Material Science, 40, 1-24.

D'Souza, Ardakani, M. G., McLean, M., Shollock, B. A. (2000): Directional and Single-Crystal Solidification of Ni-Base Superalloys: Part I. The Role of Curved Isotherms on Grain Selection. Metallurgical and Materials Transactions A, 31A, 2877-2886.

Eckart, M. (2008): Elementverteilung in recenten Brachiopodenschalen. Bachelor thesis of the Faculty for Biology, Julius-Maximilians Universität Würzburg, Germany.

Eiken, J. (2009): Dendritic growth texture evolution in Mg-based alloys investigated by phase-field simulation. International Journal of Cast Metals Research, 22, 86-89.

Eisel, U. (2006): Sehen. In: Neuro- und Sinnesphysiologie, 5th Edition. Edited by Schmid, G., Scheidele, H. G.; Springer Medizin Verlag, Germany. ISBN: 3-540-25700-4. Pages 243-287.

Ehrlich, H., Deutzmann, R., Brunner, E., Cappellini, E., Koon, H., Solazzo, C., Yang, Y., Ashford, D., Thomas-Oates, J., Lubeck, M., Baessmann, C., Langrock, T., Hoffmann, R.,Wörheide, G., Reitner, J., Simon, P., Tsurkan, M., Ereskovsky, A. V., Kurek, D., Bazhenov, V.V., Hunoldt, S., Mertig, M., Vyalikh, D. V., Molodtsov, S. L., Kummer, K., Worch, H., Smetacek, V., Collins, M. J. (2010): Mineralization of the metre-long biosilica structures of glass sponges is templated on hydroxylated collagen. Nature Chemistry, 2, 1084-1088.

Evens, A. G., Suo, Z., Wang, R. Z., Aksay, I. A., He, M. Y., Hutchinson, J. W. (2001): Model for the robust mechanical behavior of nacre. Journal of Materials Research, 16, 2475-2484.

Faivre D., Schüler, D. (2008): Magnetotactic Bacteria and Magnetosomes. Chemical Reviews, 108, 4875-4898.

Fernandez-Martinez, A., Timon, V., Roman-Ross, G., Cuello, G.J., Daniels, J.E., Ayora, C. (2010): The structure of schwertmannite, a nanocrystalline iron oxyhydroxysulfate. American Mineralogist, 95, 1312-1322.

Ferris F. G., Hallbeck, L., Kennedy, C.B., Pedersen, K. (2004): Geochemistry of acidic Rio Tinto headwaters and role of bacteria in solid phase metal partitioning. Chemical Geology, 212, 291-300.

Field, D. P. (1997): Recent advances in the application of orientation imaging. Ultramicroscopy, 67, 1-9.

Fratzl, P., Weinkammer, R. (2007): Nature's hierachical materials. Progress in Materials Science, 52, 1263-1334.

Frisia, S., Borsato, A., Fairchild, I. J., McDermott, F. (2000): Calcite Fabrics, Growth, and Environments of Formation in Speleothems from the Italian Alps and Southwest Ireland. Journal of Sedimentary Research, 70, 1183-1196.

Giesbrecht W. (1880): Der feinere Bau der Seeigelzähne. Morphologisches Jahrbuch, 6, 79-105.

Gower, L. B., Odom, D. J. (2000): Deposition of calcium carbonate films by a polymer-induced liquid-precursor (PILP) process. Journal of Crystal Growth, 210, 719-734.

Gregory, J.W. (1900): Echinoidea. In: A Treatise on Zoology Part III The Echinoderma. Edited by Lakester, E. R. Adam & Charles Black, London. Pages 282-332.

Griesshaber, E., Schmahl, W.W., Neuser, R., Pettke, T., Blum M., Mutterlose, J. Brand, U. (2007): Crystallographic texture and microstructure of terebratulide brachiopod shell calcite: An optimized materials design with hierarchical architecture. American Mineralogist,92, 722-734.

Griesshaber, E., Kelm, K., Sehrbrock, A., Mader, W., Mutterlose, J., Brand, U., Schmahl, W. W. (2009): Amorphous calcium carbonate in the shell material of the brachiopod *Megerlia truncata*. European Journal of Mineralogy, 21, 715-723.

Hahn, S., Rodolfo-Metalpa, R., Griesshaber, E., Schmahl, W.W., Buhl, D., Hall-Spencer, J., Baggini, C., Immenhauser, A., (in prep.): Exploring marine bivalve geochemistry and shell ultrastructure from modern low pH environments as possible archives of past ocean acidification. Earth and Planetary Science Letters

Hallberg, K. B., Coupland, K., Kimura, S., Johnson, D. B. (2006): Marcoscopic Streamer Growth in Acidic, Metal-Rich Mine Waters in North Wales Consist of Novel and Remarkably Simple Bacterial Communities. Applied and Environmental Microbiology, 72, 2022-2030.

Hazen, R. M., Sverjensky, D. A. (2010): Mineral Surfaces, Geochemical Complexities, and the Origin of Life. Cold Spring Harbor Perspectives in Biology, 2:a002162. doi: 10,1101/cshperspect.a002162.

He, L. H., Swain, M. V. (2007): Contact induced deformation of enamel. Applied Physics Letters, 90, 171916.

He, L. H., Swain, M. V. (2008): Understanding the mechanical behaviour of human enamel from its structural and compositional characteristics. Journal of the Mechanical Behaviour of Biomedical Materials, 1, 18-29.

Hedrich, S., Heinzel, E., Seifert, J., Schlömann, M. (2009) Isolation of novel iron-oxidizing bacteria from an acid mine water treatment plant. Advanced Materials Research, 71-73, 125-128.

Heinzel, E., Hedrich, S., Janneck, E., Glombitza, F., Seifert, J., Schlömann, M. (2009): Bacterial diversity in a Mine Water Treatment Plant. Applied and Environmental Microbiology, 75, 858-861.

Hermans, J., Borremans, C., Willenz, P., André, L., Dubois, P. (2010): Temperature, salinity and growth rate dependences of Mg/Ca and Sr/Ca ratios of the

skeleton of the sea urchin *Paracentrotus lividus* (Lamarck): an experminetal approach. Marine Biology, 157, 1293-1300.

Hernández-Hernández, A., Vidal, M. L., Gómez-Morales, J., Rodríguez-Navarro, A. B., Labas, V., Gautron, J., Nys, Y., García Ruiz, J. M. (2008): Influence of eggshell matrix proteins on the precipitation of calcium carbonate ($CaCO_3$). Journal of Crystal Growth, 310, 1754-1759.

Holland, N. D. (1965): An autoradiographic investigation of tooth renewal in the purple sea urchin (*Strongylocentrotus purpuratus*). Journal of Experimental Zoology, 158, 275-281.

Holmes, D. S., Bonnefoy, V. (2007): Iron and Sulfur Oxidation Mechanisms of Bioleaching Organisms. In: Biomining. Edited by: Rawlings, D. E., Johnson, D. B.; Springer, Germany, ISBN: 3-540-34909-X. Pages 281-307.

Jakob, D., Soldati, A. L., Wirth, R., Huth, J., Wehrmeister, U., Hofmeister W. (2008): Nanostructure, composition and mechanisms of bivalve shell growth. Geochimica et Cosmochimca Acta, 72, 5401-5415.

Jee, S. S., Thula, T. T., Gower, L. B. (2010): Development of bone-like composites via polymer-induced liwuid precursor (PILP) process. Part 1: Influence of polymer molecular weight. Acta Biomaterialia, 6, 3676-3686.

Koehler, I., Kronhauser, K., Kappler, A. (2010): The role of Microorganisms in Banded Iron Formation. In: Geomicrobiology: Molecular and Environmental Perspective. Edited by Barton, L. L.; Springer Netherlands; ISBN: 978-90-481-9204-5. Pages 309-324.

Krauss, S., Monsonego-Ornan, E., Zelzer, E., Fratzl, P., Shahar, R. (2008): Mechanical Function of a Complex Three-Dimensional Sutur Joining of Bony Elements in the Shell of the Red Eared Slider Turtle. Advanced Material, 21, 407-412.

Larese-Casanova, P., Haderlein, S. B., Kappler, A. (2010): Biomineralization of lepidocrocite and goethite by nitrate-reducing Fe(II)-oxidizing bacteria: Effect of pH, bicarbonate, phosphate, and humic acids. Geochimica et Cosmochimica Acta, 74, 3721-3734.

Lawn, B. R., Lee, J. J. W., Chai, H. (2010): Teeth: Among Nature's Most Durable Biocomposites. Annual Reviews in Material Research, 40, 55-75.

Layne, J. E., Nelson, M. E. (1999): The effects of progressive resistance training on bone density: a review. Medicine & Science in Sports & Exercise, 31, 25-30.

Li, X, Chang, W. C., Chao, Y. J., Chang, M. (2004): Nanoscale Structural and Mechanical Characterization of a Natural Nanocomposite Material: The Shell of Red Abalone. Nano Letters, 4, 613-617.

Logan, T. C., Seal, T., Brierlay, J. A. (2007): Whole-Ore Heap Biooxidation of Sulfidic Gold-Bearing Ores. In: Biomining. Edited by: Rawlings, D. E., Johnson, D. B.; Springer, Germany, ISBN: 3-540-34909-X. Pages 113-138.

Lowenstam, H. A., Weiner, S. (1989): On biomineralization. Oxford University Press, New York. ISBN:0-19-504977-2.

Magdans, U., Gies, H. (2004): Single crystal structure analysis of sea urchin spine calcites: Systematic investigations of the Ca/Mg distribution as a function of habitat of the sea urchin and the sample location in the spine. European Journal of Mineralogy, 16, 261-268.

Mahamid, J., Sharir, A., Addadi, L., Weiner, S. (2008): Amorphous calcium phosphate is a mahor component of the forming fin bones of zebrafish: Indications for an amorphous precursor phase. Proceedings of the National Academy of Sciences, 105, 12748-12753.

Mann, S. (1983): Mineralization in biological systems. Structure and Bonding, 54, 125-174.

Märkel K. (1969): Morphology of Sea-Urchin Teeth. 2. Keeled Teeth of Echinacea (Echinodermata, Echinoidea). Zeitschrift für Morpholologie der Tiere, 66, 1-50.

Markel K, Gorny P. (1973): Functional Anatomy of Sea-Urchin Teeth (Echinodermata, Echinoidea). Zeitschrift für Morphologie der Tiere, 75, 223-242.

Märkel, K., Röser, U. (1983): The Spine Tissues in the Echinoid *Eucidaris tribuloides*. Zeitschrift für Morphologie der Tiere, 103, 25-41.

Meldrum, F. C., Mann, S., Heywood, B. R., Frankel, R. B., Bazylinski, D. A. (1993): Electron Microscopy Study of Magnetosomes in a Cultured Coccoid Magnetotactic Bacterium. Proceedings of the Royal Society B, 22, 231-236.

Menig, R., Meyers, M. H., Meyers M. A., Vecchio, K. S. (2000): Quasi-Static and Dynamic Mechanical Response of *Haliotis Rufescens* (Abalone) Shells. Acta Materialia, 48, 2383-2398.

Merten, H. L., Bachman, G. L. (1980): Stabilized Amorphous Calcium Carbonate. US patent Nr. 4237147.

Meyers, M A., Chen, P. Y., Lin, A. Y. M., Seki, Y. (2008): Biological materials: Structure and mechanical properties. Progress in Materials Science, 53, 1-206.

Mitterer, R. M. (1978): Amino Acid Composition and Metal Binding Capability of the Skeletal Protein of Corals. Bulletin of Marine Science, 28, 173-180.

Moore, J. (2006): An Introduction to the Invertebrates. Second edition. Cambridge University Press, New York, USA. ISBN: 0-511-24942-X.

Morin, D. H. R., d'Huges, P. (2007): Bioleaching of a Cobalt-Containing Pyrite inn Stirred Reactors: a Case Study from Laboratory Scale to Industrial Application. In: Biomining. Edited by: Rawlings, D. E., Johnson, D. B.; Springer, Germany, ISBN: 3-540-34909-X. Pages 35-53.

Nassif, N., Gobeaux, F., Seto, J., Belamie, E., Davidson, P., Panine, P., Mosser, G., Fratzl, P., Giraud Guille, M. M. (2010): Self-Assembled Collagen-Apatite Matrix with Bone-like Hierarchy. Chemistry of Materials, 22, 3307-3309.

Neuser, R. D., Richter, D. K. (2007): Non-marine radiaxial fibrous calcites - examples of speleothems proved by electron backsatter diffraction. Sedimentary Geology, 194, 149- 154.

Nesterova, M., Moreau, J., Banfield, J. F. (2003): Model biomimetic studies of templated growth and assembly of nanocrystalline FeOOH. Geochimica et Cosmochimica Acta, 67, 1177-1187.

Norris, P. R., Murrel, C., Hinson, D. (1995): The potential for diazotrophy in iron- and sulfur-oxidizing axidophilic bacteria. Archives of microbiology, 164, 294-300.

Norris, P. R. (2007): Acidophile Diversity in Mineral Sulfide Oxidation. In: Biomining. Edited by: Rawlings, D. E., Johnson, D. B.; Springer, Germany, ISBN: 3-540-34909-X. Pages 199-216.

Oaki, Y, Imai, H. (2005): Nanoengineering in Echinoderms: The Emergence of Morphology from Nanobricks. Small, 2, 66-70.

Paquette, J., Reeder, R.J. (1990): Single-Crystal X-Ray Structure Refinements of 2 Biogenic Magnesian Calcite Crystals. American Mineralogist, 75, 1151-1158.

Parkinson, D., Curry, G. B., Cusack, M., Fallick, A. E. (2005): Shell structure, patterns and trends of oxygen and carbon stable isotopes in modern brachiopod shells. Chemical Geology, 219, 193-235.

Parro, V., Moreno-Paz, M. (2003): Gene function analysis in environmental isolates: The nif regulon of the strict iron oxidizing bacterium Leptospirillum ferrooxidans. Proceedings of the National Academy of Sciences, 100, 7883–7888.

Peck, L. S. (2001): Pyhsiology. The Paleontological Society Special Papers, 7, 89-104.

Peiffer, S., Paikaray, S., Damian, Ch., Janneck, E., Ehinger, S., Martin, M., Schlömann, M., Wiacek, C., Kipry, J., Schmahl, W., Pentcheva, R., Otte, K., **Götz, A.**, Wang, Z., Hsieh, K., Meyer, J., Schöne, G., Koch, T., Ziegler, A., Burghardt, D. (2010): SURFTRAP - Development and Optimisation of a Process to Biosynthesize Reactive Iron Mineral Surfaces for Water Treatment Purposes. GEOTECHNOLOGIEN Science Report, 16, 154-169.

Pérez-Huerta, A., Dauphin, Y., Cuif, J. P., Cusack, M. (2011): High resolution electron backscatter diffraction (EBSD) data from calcite briominerals in recent gastropod shells. Micron, 2011, 246-251.

Politi, Y., Arad, T., Klein, E., Weiner, S., Addadi, L. (2004): Sea Urchin Spine Calcite Forms via a Transient Amorphous Calcium Carbonate Phase. Science, 12, 1161-1164.

Politi, Y., Metzler, R. A., Abrecht, M., Gilbert, B., Wilte, F. H., Sagi, I., Addadi, L., Weiner, S., Gilbert, P. U. P. A. (2008): Transformation mechanism of amorphous calcium carbonate into calcite in the sea urchin larval spicule. Proceedings of the National Academy of Sciences, 105, 17362-17366.

Presser, V., Kohler, C., Zivcová, Z., Berthold, C., Nickel, K. G., Schultheiß, S., Gregorova, E., Pabst, W. (2009): Sea Urchin Spines as Model System for Permeable, Light-Weight Ceramics with Graceful Failure Behaviour. Part II. Mechanical Behavior of Sea Urchin Spine Inspired Poroous Aluminim Oxide Ceramics under Compression. Journal of Bionic Engeneering, 6, 357-364.

Rahman, M. A., Oomori, T. (2008): Aspartic Acid-rich Proteins in Insoluble Organic Matrix Play a Key Role in the Growth of Calcitic Sclerites in Alcyonarian Coral. Chinese Journal of Biotechnology, 24, 2127-2128.

Raue, L., Klein, H. (2010): Location depending textures of the human dental enamel. Solid State Phenomena, 160, 281-286.

Rawlings, D. E. (2007): Relevance of Cell Physiology and Genetic Adaptability of Biomining Microorganisms to Industrial Processes. In: Biomining. Edited by: Rawlings, D. E., Johnson, D. B.; Springer, Germany, ISBN: 3-540-34909-X. Pages 177-198.

Regenspurg, S., Peifer, S. (2005): Arsenate and chromate incorporation in schwertmannite. Applied Geochemistry, 20, 1226-1339.

Ren S. X., Kenik, E. A., Alexander, K. B., Goyal, A. (1998): Exploring Spatial Resolution in Electron Back-Scattered Diffraction Experiments via Monte Carlo Simulation. Microscopy and Microanalyses, 4, 15-22.

Ries, J. B. (2004): Effect of ambient Mg/Ca ratio on Mg fractionation in calcerous marine invertebrates: A record of the oceanic Mg/Ca ratio over the Phanerozoic. Geology, 32, 981-984.

Robach, J. S., Stock, S. R., Veis, A. (2006): Mapping of magnesium and of different protein fragments in sea urchin teeth via secondary ion mass spectroscopy. Journal of Structural Biology, 155, 87-95.

Robach, J. S., Stock, S. R., Veis, A. (2009): Structure of first- and second-stage mineralized elements in teeth of the sea urchin *Lytechinus variegatus*. Journal of Structural Biology, 168, 452-466.

Rodrigues-Navarro, A. (2001): Model of texture development in polycrystalline films growing on amorphous substrates with different topographies. Thin Solid Films, 389, 288-295.

Rodrigues-Navarro, A., Kalin, O., Nys, Y., Garcia-Ruiz, J. M. (2002): Influence of the microstructure on the shell strength of eggs laid by hens of different ages. British Poultry Sciences. DOI: 10.2080/00071660120103675.

Rohwerder, T., Gehrke, T., Kinzler, K., Sand, W. (2003): Bioleaching review part A: Progress in bioleaching: fundamentals and mechanisms of bacterial metal sulfide oxidation. Applied Microbiology and Biotechnology, 63, 239-248.

Rojas-Chapana, J. A., Tributsch, H. (2004): Interfacial activity and leaching patterns of *Leptospirillum ferrooxidans* on pyrite. FEMS Microbiology Ecology, 47, 19-29.

Rossi, A. L., Farina, M., Borojevic, R., Klautau, M. (2006): Occurence of five rayed spicules in a calcareous sponge: *Sycon pentactinalis* sp. nov. (Porifera: Calcarea). Cahiers de Biologie Marine, 47, 261-270.

Rudwick, M.J.S. (1970): Living and fossil brachiopods. Hutchinson, London, UK. ISBN: 0091030803.

Salter, J. A. (1861): On the Structure and Growth of the Tooth of Echinus. Philosophical Transactions of the Royal Society of London, 151, 387-407.

Sandbdberg, P.A. (1983): An oscillating trend in Phanerozoic non-skeletal carbonate mineralogy. Nature, 305, 19-22.

Schäffer, T. E., Ionescu-Zanetti, C., Proksch, R., Fritz, M., Walters, D. A., Almqvist, N., Zaremba, C. M. (2008): Does Abalone Nacre Form by Heteroepitaxial Nucleation or by Growth through Mineral Bridges? Chemistry of Materials, 9, 1731-1740.

Schmahl, W.W., Griesshaber, E., Merkel, C., Kelm, K., Deuschle, J., Neuser, R.D., **Goetz, A. J.**, Sehrbrock, A., Mader, W. (2008): Hierarchical fibre composite structure and micromechanical properties of phosphatic and calcitic brachiopod shell biomaterials - an overview. Mineralogical Magazine, 72, 539 - 560.

Schmahl, W.W., Griesshaber, E., Neuser, R.D., **Goetz, A.**, Lüter, C. (2009): Electron Backscatter Diffraction Study of Brachiopod Shell Calcite - Microscale Phase and Texture Analysis of a Polycrystalline Biomaterial. Particle and Particle Systems Characterization, 25, 474-478.

Schmahl, W. W., Kelm, K., Griesshaber, E., **Goetz, A.**, Jordan, G., Xu, D., Merkel, C., Brand, U., Logan, A. (2010): The hierachical organization in biomaterials: from nanoparticles vio mescrystals to functionality. Seminarios de la Sociedad Espanola de Mineralogía, 7, 5-21.

Schmidt, W.J. (1930): Die Skelettstücke der Stachelhäuter als Biokristalle. Zoologisches Jahrbuch Allgemeine Zoologie, 47, 357-510.

Schrenk, M. O., Edwartds, K. J., Goodman, R. M., Hamers, R. J., Banfield, J. F. (1998): distribution of *Thiobacillus ferrooxidans* and *Leptospirillum ferrooxidans*: Implications for Generation of Acid Mine Drainage. Science, 2779, 1519-1522.

Schulz - Mierbach, T., Griesshaber, E., **Goetz, A. J.**, Schmahl, W. W. et al. (in prep.): The texture and nano-scale internal microstructure of the Atlantic molly *Poecilia mexicana*: a high-resolution EBSD study. to be submitted to Micron.

Sethmann, I., Putnis, A., Grassmann, O., Löbmann, P. (2005): Observation of nano-clustered calcite growth via an transient phase mediated by organic polyanions: A close match for biomineralization. American Mineralogist, 90, 1213-1217.

Sethmann, I., Hinrichs, R., Wörheide, G., Putnis, A. (2006): Nano-cluster composite structure of calcitic sponge spicules - A case study of basic characteristics of biominerals. Journal of Inorganic Biochemistry, 100, 88-96.

Sethmann, I., Wörheide, G. (2008): Structure and composition of calcareous sponge spicules: A review and comparision to structurally related biominerals. Micron, 39, 209-228.

Smith, A. B. (1980): Stereom Microstructure of the Echinoid Test. Special Papers of Palaeontology, 25, 1-81.

Smith, B. L., Schäffer, T. E., Viani, M., thompson, J. B., Frederick, N. A., Kindt, J., Belcher, A., Stuck, G. D., Morse, D. E., Hansma, P. K. (1999): Molecular mechanistic origin of the toughness of natural adhesives, fibres and composites. Nature, 761-763.

Soldati, A. L. Jacob, D. E., Wehrmeister, U., Wehrmeister, W. (2008): Structural characterization and chemical composition of aragonite and vaterite in freshwater cultured pearls. Mineralogical Magazine, 72, 577–590.

Song, F., Soh, A. K., Bay, Y. L. (2003): Structure and mechanical properties of the organic matrix layers of nacre. Biomaterials, 24, 3623-3631.

Song, F., Bay, Y. L. (2003): Effects of nanostructures on the fracture strength of the interfaces in nacre. Journal of Materials research, 18, 1741-1744.

Stahl, K., Nielsen, K., Jiang, J. Z., Lebech, B., Hanson, J. C., Norby, P., van Lanschot, J. (2003): On the akaganeite crystal structure, phase transformations and possible role in post-excavational corrosion of iron artifacts. Corrosion Science, 45, 2563-2575.

Stock, S. R., Ignatiev, K. I., Dahl, T., Veis, A., De Carlo, F. (2003): Three-dimensional micro architecture of the plates (primary, secondary, and carinar process) in the developing tooth of Lytechinus variegatus revealed by synchrotron X-ray absorption microtomography (microCT). Journal of Structural Biology, 144, 282-300.

Strathmann, R.R. (1981) The Role of Spines in Preventing Structural Damage to Echinoid Tests. Paleobiology, 7, 400-406.

Steinmetz, D. R., Zaefferer S.(2010): Towards ultrahigh resolution EBSD by low accelerating voltage. Material Science and Technology, 26, 640-645.

Su, X., Kamat, S., Heuer, A.H. (2000): The structure of sea urchin spines, large biogenic single crystals of calcite. Journal of Materials Science, 35, 5545-5551.

Tang, Z., Kotov, N. A., Magonov, S., Ozturk, B. (2003): Nanostructured artificial nacre. Nature Materials, 2, 413-418.

Tributsch, H., Rojas-Chapana, J. A. (2007): Bacterial Strategies for Obtaining Chemical Energy by Degrading Sulfide Minerals. In: Biomining. Edited by: Rawlings, D. E., Johnson, D. B.; Springer, Germany, ISBN: 3-540-34909-X. Pages 263-280.

Thomas-Keprta, K. L., Bazylinsky, D. A., Kirschvink, J. L., Clemett, S. J., McKay, D. S., Wentworth, S. J., Vali, H., Gibson, E. K., Romanek, C. S. (2000): Elongated prismatic magnnetite crystals in ALH84991 caronate globules: Potential Martian magnetofossils. Geochimica et Cosmochimica Acta, 64, 4049-4081.

Tysen, G. W., Chapman, J., Hugenholtz, P., Allen, E. E., Ram, R. J., Richardson, P. M., Solovyev, V. V., Rubin, E. M., Rokhsar, D. S., Banfield, J. F. (2004): Community structure and metabolism through reconstruction of microbial genomes from the environment. Nature, 428, 37-43.

Versnyder, F. L., Shank, M. E. (1970): The Development of Columnar Grain and Single Crystal High Temperature Materials Thorugh Directional Solidification. Materials Science and Engineering, 6, 213-247.

Veizer, J., Ala, D., Azmy, K., Bruckschen, P., Buhl, D., Bruhn, F., Carden, G. A. F., Diener, A., Ebneth, S., Godderis, Y., Jasper, T., Korte, C., Pawellek, F., Podlaha, O. G., Strauss, H. (1999): ^{87}Sr / ^{86}Sr, δ ^{13}C and δ ^{18}O evolution of Phaerozoic seawater. Chemical Geology, 161, 59-88.

Wächtershäuser, G. (1988): Before Enzymes and Templates - Theory of Surface Metabolism. Microbiological reviwes, 52, 452-484.

Wächtershäuser, G. (1990): Evolution of the first metabolic cycles. Proceedings of the National Academy of Sciences, 87, 200-204.

Wächtershäuser, G. (2000): Life as we don't know it. Science, 25, 1307-1308.

Wang, R. Z., Wen, H. B., Cui, F. Z., Zhang, H. B., Li, H. D. (1995): Observations of damage morphologies in nacre during deformation and fracture. Journal of Materials Science, 30, 2299-2304.

Wang, R. Z., Addadi, L., Weiner, S. (1997): Design strategies of sea urchin teeth: Structure, composition and micromechanical relations to function. Philosophical Transactions of the Royal Society of London Series B-Biological Sciences, 352, 469-480.

Wang, R. Z., Suo, Z., Evans, A. G., Yao, N., Aksay, I. A. (2001): Deformation mechanisms in nacre. Journal of Material Research. 16, 2485-2493.

Wang, H., Bigham, J. M. , Tuovinen, O. H. (2006): Formation of schwertmannite and its transformation to jarosite in the presence of acidophilic iron-oxidizing microorganisms. Materials Science & Engeneering C, 26, 588-529.

Waychunas, G.A., Xu, N., Fuller, C. C., Davis, J. A., Davis, J. A., Bigham, J. M. (1995): XAS study of AsO_4^{3-} and SeO_4^{2-} substituted schwertmannites. Physica B, 208 & 209, 481-483.

Webern K. A., Achenbach, L. A., Coates, J. D. (2006): Microorganisms pumping iron: anaerobic microbial iron oxidation and reduction. Nature Reviews Microbiology, 2, 752-764.

Webster, J. G., Swedlund, P. J., Webster, K. S. (1998): Trace Metal Adsorption onto an Acid Mine Drainage Iron(III) Oxy Hydroxy Sulfate. Environmental Science and Technology. 32, 1361-1368.

Wegst,U G. K., Ashby, M. F. (2004): The mechanical efficiecy of natural materials. Philosphical Magazine, 21, 2671-2181.

Weiner, S. (1979): Aspartic Acid-Rich Proteins: Major Components of the Soluble Organic Matrix of Mollusc Shells. Calcified Tissue International, 29, 163-167.

Weiner, S., Sagi, I., Addadi, L. (2005): Choosing the Crystallization Path Less Traveled. Science, 309, 1027-1028.

Weis, I. M., Renner, C., Strigl, M. G., Fritz, M. (2002): A Simple Reliable Method for the Determination and Localization of Chitin in Abalone Nacre. Chemistry of Materials, 12, 3252-3259.

Williams, A., Bruntun, C. H. C. and Carlson, S. J. (1997): Treatise on Invertebrate Paleontology Part H Brachiopoda. The Geological Society of America. ISBN: 0-8137-3108-9.

Winklhofer, M., Petersen, N. (2006): Paleomagnetism and Magnetic Bacteria. In: Magnetoreception and Magnetosomes in Bacteria. Edited by: Schüler, D.; Springer, Germany, ISBN: 3-540-37467. Pages 255-274.

Winklhofer, M. (2008):Nanobiotechnology: Putting cobalt on the menu. Nature Nanotechnology, 3, 135 - 136.

Wright, S. I., Nowell, M. M. (2006): EBSD image quality mapping. Microscopy and Microanalysis, 12, 72–84.

Xu, A. W., Antonietti, M., Cölfen, H., Fang, Y. P. (2006): Uniform Hexagonal Plates of Vaterite $CaCO_3$ Mesocrystals Formed by Biomimetic Mineralization. Advanced Functional Materials. 16, 903-908.

Yamamota, K., Asami, R., Iryu, Y. (2010): Within-shell variations in carbon oxygen isotope compositions of two modern brachiopods from a subropical shelf environment off Amami-o-shima, southwestern Japan. Geochemistry, Geophysics Geosystems, 11, Q10009. doi:10.1029/2010GC003190.

Zhou, G. T., Yao, Q. Z., Jin, G. (2009): Formation of aragonite mesocrystals and implication for biomineralisation. American Mineralogist, 94, 293-302.

Articles Prepared as Part of the Present Thesis

This chapter gives an overview over the published and submitted works prepared as a part of this thesis. Articles published aside the thesis are not mentioned. A complete list of my publications can be found in the subsequent section.

Published Peer-Reviewed Articles

Section 3.3: Goetz, A.J., Steinmetz, Griesshaber, E., Zaefferer, S., Raabe, D., Kelm, K., Irsen, S., Sehrbrock, A., Schmahl, W.W. (2011): Interdigitation Biocalcite Dendrites form a 3-D Jigsaw-Structure in Brachiopod Shells. Acta Biomaterialia, 7, 2237-2243.

Section 3.4: Goetz, A., Griesshaber, E., Schmahl, W.W. (2010): An Easy Approach to Increase the Precession of EBSD Analysis - Examples from a Sea Urchin Calcite Study. Solid State Phenomena, 160, 229-234.

Section 3.2: Goetz, A. J., Griesshaber, E., Neuser, R. D., Lüter, C., Hühner, M., Harper, E., Schmahl, W. W. (2009): Calcite morphology, texture and hardness in the distinct layers of rhynchonelliform brachiopod shells. European Journal of Mineralogy, 21, 303-315.

Submitted Manuscripts

Section 3.1: Goetz, A. J., Ziegler, A., Kipry, J., Wagner, F. E., Wang, Z.-L., Hsieh, K.-Y., Parks, S.-H., Pentcheva, R., Wiacek, C., Schlömann, M., Janneck, E., Schmahl, W. W.: On the Structure and Formation of Biotic and Abiotic Schwertmannite. Submitted to *European Journal of Mineralogy.*

Section 3.6: Goetz, A. J., Griesshaber, E., Deuschle, J., Abel, R., Howard, L. Fehr, K. T., Ruthensteiner, B., Schmahl, W. W.: Biomechanical functionalisation by composite crystal hierarchical architectures: crystallography of the tooth of the sea urchin *Paracentrotus lividus.* Submitted to *Journal of Structural Biology.*

List of Publications

Articles

Goetz, A. J., Steinmetz, D. R., Griesshaber, E., Zaefferer, S., Raabe, D., Kelm, K., Irsen, S., Sehrbrock, A., Schmahl, W.W. (2011): Interdigitating Biocalcite Dendrited form a 3D Jigsaw-Structure in Brachiopod Shells. Acta Biomateri-alia, 7, 2237-2243.

Kelm, K., Griesshaber, E., **Goetz, A.**, Schmahl, W. W.: How perfect are sea urchin spine single crystals ? Examples from the spine of the sea urchin *Holopneustes porosissimus*. Proceedings of the Microscopy Conference 2011, in print.

Schmahl, W. W., Kelm, K., Griesshaber, E., **Goetz, A.**, Jordan, G., Xu, D., Merkel, C., Brand, U., Logan, A. (2010): The hierachical organization in biomaterials: from nanoparticles vio mescrystals to functionality. Seminarios de la Sociedad Espanola de Mineralogía, 7, 5-21.

Peiffer, S., Paikaray, S., Damian, Ch., Janneck, E., Ehinger, S., Martin, M., Schlö-mann, M., Wiacek, C., Kipry, J., Schmahl, W., Pentcheva, R., Otte, K., **Goetz, A.**, Wang, Z., Hsieh, K., Meyer, J., Schöne, G., Koch, T., Ziegler, A., Burghardt, D. (2010): SURFTRAP - Development and Optimisation of a Process to Biosynthesize Reactive Iron Mineral Surfaces for Water Treatment Purposes. GEOTECHNOLOGIEN Science Report, 16, 154-169.

Goetz, A., Griesshaber, E., Schmahl, W.W. (2010): An Easy Approach to In-crease the Precession of EBSD Analysis - Examples from a Sea Urchin Calcite Study. Solid State Phenomena, 160, 229-234.

Goetz, A. J., Griesshaber, E., Neuser, R. D., Lüter, C., Hühner, M., Harper, E., Schmahl, W. W. (2009): Calcite morphology, texture and hardness in the distinct layers of rhynchonelliform brachiopod shells. European Journal of Mineralogy, 21, 303-315.

Schmahl, W.W., Griesshaber, E., Neuser, R.D., **Goetz, A.**, Lüter, C. (2009): Elec-tron Backscatter Diffraction Study of Brachiopod Shell Calcite - Microscale Phase and Texture Analysis of a Polycrystalline Biomaterial. Particle and Particle Systems Characterization, 25, 474-478.

Schmahl, W.W., Griesshaber, E., Merkel, C., Kelm, K., Deuschle, J., Neuser, R.D., **Goetz, A. J.**, Sehrbrock, A., Mader, W. (2008): Hierarchical fibre composite structure and micromechanical properties of phosphatic and calcitic

brachiopod shell biomaterials - an overview. Mineralogical Magazine, 72, 539 - 560.

Submitted Manuscripts

Goetz, A. J., Ziegler, A., Kipry, J., Wagner, F. E., Wang, Z.-L., Hsieh, K.-Y., Parks, S.-H., Pentcheva, R., Wiacek, C., Schlömann, M., Janneck, E., Schmahl, W. W.: On the Structure and Formation of Biotic and Abiotic Schwertmannite. Submitted to *European Journal of Mineralogy.*

Goetz, A. J., Griesshaber, E., Deuschle, J., Abel, R., Howard, L. Fehr, K. T., Ruthensteiner, B., Schmahl, W. W.: Biomechanical functionalisation by composite crystal hierarchical architectures: crystallography of the tooth of the sea urchin *Paracentrotus lividus.* Submitted to *Journal of Structural Biology.*

Dienstmaier, J. F., Gigler, A. M., **Goetz, A. J.**, Knochel, P., Bein, T., Heckl, W. M., Lackinger, M.: Synthesis of well-ordered COF monolayers via surface growth of nanocrystalline precursors. Submitted to *Advanced Materials.*

Talks at Conferences

High spacial resolution EBSD reveals a novel microstructure of brachiopod shell primary layer.
A.J. Goetz, D. R. Steinmetz, E. Griesshaber, S. Zaefferer, D. Raabe, K. Kelm, S. Irsen, A. Sehrbrock, W.W. Schmahl.
EBSD 2011, Düsseldorf, Germany, 28. - 30. March 2011.

Sea Urchin Teeth - A Mechanical, Chemical and Crystallographic Characterization of a Highly Optimized Biogenic Composite Material.
A.J. Goetz, E. Griesshaber, W.W. Schmahl.
XXX Reunión de la Sociedad Española de Mineralogía, Madrid, Spanien, 13. - 16. September 2010.

An easy approach to increase the precission of EBSD analysis - A sea urchin calcite study.
A.J. Goetz, E. Griesshaber, W.W. Schmahl.
3rd International Conference on Texture and Anisotropy of Polycrystals (ITAP-3), Göttingen, 23-25 September 2009.

Sea Urchin Teeth - A Mechanical, Chemical and Crystallographic Characterization of a Highly Optimised Biogenic Composite Material.
A.J. Goetz, E. Griesshaber, J. Deuschle, Th. Fehr, S. Bernstein, W.W. Schmahl
Micro-Analysis, Processes, Time, Annual Meeting of the Mineralogical Society of Great Britain and Ireland, Edinburgh, UK, 31. August - 2. September 2009.

Small Tools for the Evaluation and Representation of Small Angular Differences in
   EBSD Datasets.
   A. J. Goetz, E. Griesshaber, W. W. Schmahl.
   DGM/DGK AK-Treffen: Mikrostrukturcharakterisierung im REM. TU Chem-
   nitz, 18. + 19. Mai 2009.

An Easy Approach to Increase the Precession of EBSD Analysis - A Sea Urchin
   Calcite Study.
   A.J. Goetz, E. Griesshaber, W. W. Schmahl.
   DGM/DGK AK-Treffen: Mikrostrukturcharakterisierung im REM. TU Chem-
   nitz, 18. + 19. Mai 2009.

Posters presented at conferences

Structural Variations in Biogenic and Synthetic Schwertmannite.
   A.J. Goetz, A. Ziegler, J. Kipry, C. Wiacek, M. Schlömann, W. W. Schmahl.
   XXX Reunión de la Sociedad Española de Mineralogía, Madrid, Spanien, 13.
   - 16. September 2010.

Bacteria-controlled precipitation of iron-oxides in contaminated environments.
   A.J. Goetz, A. Ziegler, J. Kipry, C. Wiacek, M. Schlömann, W. W. Schmahl.
   EMU-School 2010: Ion-Partitioning in ambient temperature aqueous systems.
   Oviedo, Spanien, 27. - 40. Juni 2010.

Sea Urchin teeth are hierarchically structured mesocrystals.
   A.J. Goetz, A. Ziegler, J. Kipry, C. Wiacek, M. Schlömann, W. W. Schmahl.
   EMU-School 2010: Ion-Partitioning in ambient temperature aqueous systems.
   Oviedo, Spanien, 27. - 40. Juni 2010

Small tools for the evaluation and representation of small angular differences in
   EBSD datasets.
   A.J. Goetz, E. Griesshaber, W.W. Schmahl.
   3rd International Conference on Texture and Anisotropy of Polycrystals (ITAP-
   3), Göttingen, 23. - 25. September 2009.

Textur und Härteverteilung in rezenten Brachiopoden - ein Vergleich zwischen ein-
   schichtigen und mehrschichtigen Schalen. The texture and hardness distribu-
   tion pattern in recent brachiopods - a comparative study between single and
   multilayered shells.
   A. J. Goetz, E. Griesshaber, W.W. Schmahl.
   DGK Tagung Erlangen, 3. - 6. März 2008.

Electron Diffraction and Vickers Microhardness Reveal "Advanced" Materials De-
   sign of Brachiopod Shells.
   A. J. Goetz, E. Griesshaber, K. Kelm, A. Sehrbrock, C. Merkel, C. Lüter,
   R. Neuser, W. Mader, W. W. Schmahl.
   DGK Tagung Bemen, 5. - 9. März 2007.

The texture and hardness distribution pattern in modern brachiopods - an 'advanced' materials design.
A. J. Goetz, E. Griesshaber, W. W. Schmahl,C. Lüter, M. Hühner, D. Neuser.
Frontiers of Mineralogy, Cambridge, UK, 26. - 28. Juni 2007.

Crystal Orientation Selection during Growth of Brachiopod Shell Calcite.
A. J. Goetz, E. Griesshaber, W. W. Schmahl, C. Lüter.
Goldschmidt Conference, Cologne, 19. - 24. August 2007.

Awards and Memberships

Awards

- *Young Scientist Prize* for the best oral communication on the annual of meeting of the *Sociedad Española de Mineralogía* 2011, Madrid.

Memberships

- Deutsche Mineralogische Gesellschaft (DMG)

- Deutsche Kristallographische Gesellschaft (DGK)

- Sociedad Española de Mineralogía (SEM)

Curriculum Vitae

Personal Data

NAME: Andreas Johannes Götz

BORN: May, 9th 1983 in Hirschau, Germany.

NATIONALITY: German

FAMILY STATUS: married

ADRESS: Livingstonestr. 1
95615 Marktredwitz

TELEPHONE: 0170 765 97 36

E-Mail: andreas.goetz@lrz.uni-muenchen.de

School

1988-1990 Grundschule Hirschau.

1990-1992 Grundschule Wunsiedel.

1992-2002 Luisenburg Gymnasium Wunsiedel, graduated with *Abitur*.

Community Service

2002 - 2003 Kreiskrankenhaus München Perlach - Nursing Service.

Academic Career

2003-2006 Bachelor of Science in Earth Sciences.
LMU and TUM, Munich, Germany.

2006-2008 Master of Science in Geochemistry and Geomaterials.
LMU and TUM, Munich, Germany.

since 2009 PhD-student at the Chair for Inorganic and Organic Geomaterials,
Department for Earth and Environmental Sciences, LMU Munich.

Memberships

since 2007 Deutsche Mineralogische Gesellschaft

since 2007 Deutsche Kristallographische Gesellschaft

since 2010 Sociedad Española de Mineralogía